

INAUGURAL - DISSERTATION
zur
Erlangung der Doktorwürde
der Naturwissenschaftlich - Mathematischen
Gesamtfakultät
der
Ruprecht - Karls - Universität
Heidelberg

vorgelegt von
Dipl.-Phys. Vago Kilian Hesshaimer
aus Konstanz

Tag der mündl. Prüfung 11.7.1997

TRACING THE GLOBAL CARBON CYCLE
WITH BOMB RADIOCARBON

Gutachter:

Prof. Dr. Karl Otto Münnich
Prof. Dr. Till Kirsten

BOMBEN ^{14}C ALS TRACER DES REZENTEN KOHLENSTOFFKREISLAUFS

Zusammenfassung: Radiokohlenstoff (^{14}C) aus Kernwaffentests hat innerhalb des rezenten Kohlenstoffkreislaufs noch kein Gleichgewicht erreicht. In der vorliegenden Arbeit wurde der Verbleib von Bomben ^{14}C seit 1950 mit Hilfe grobauflösender Modelle untersucht. Ziel der Arbeit war es, das Potential von ^{14}C als Tracer zur Validierung von Austauschraten zwischen den einzelnen Kohlenstoff-Reservoirs zu bestimmen. Als Basis dienten die am Institut vorhandenen langen Messreihen von $^{14}\text{CO}_2$ in der Atmosphäre. Es wurden drei wichtige Ergebnisse erzielt: 1. Das nur anthropogen in die Atmosphäre freigesetzte inerte Spurengas SF_6 wurde erstmals erfolgreich zur Validierung globaler atmosphärischer Transportmodelle eingesetzt. 2. Die Bilanz des Bomben ^{14}C in einem einfachen Boxmodell des Kohlenstoffkreislaufs konnte nicht geschlossen werden, was höchstwahrscheinlich eine zu starke Aufnahme von Bomben ^{14}C durch die Ozeane bedeutet. Dann wäre die Aufnahme von anthropogenem CO_2 durch die Ozeane um 25% niedriger als bisher angenommen. 3. Die Anbindung von ^{14}C Messungen in der Stratosphäre an die troposphärischen Messungen während und kurz nach den Kernwaffentests diente zur Quantifizierung des Stratosphären/Troposphären-Austauschs. Diese drei Werkzeuge konnten für eine vorläufige Interpretation der saisonalen Variation des rezenten atmosphärischen $^{14}\text{CO}_2$ eingesetzt werden.

TRACING THE GLOBAL CARBON CYCLE WITH BOMB RADIOCARBON

Abstract: Bomb radiocarbon (^{14}C) emitted to the atmosphere by nuclear explosion tests has not yet reached equilibrium within the Earth carbon system. In the present thesis this fate of radiocarbon is investigated using coarse-grid models to trace high-precision $^{14}\text{CO}_2$ observations available in the atmosphere since the 1950s. The goal of the study is to progress our quantitative understanding of bomb radiocarbon following the pathways of the global carbon cycle. Inversely, I wanted also to determine new constraints on the atmospheric carbon budget buried in the long-term observations of atmospheric $^{14}\text{CO}_2$. Three relevant findings came out at the different stages of my research. First, the man-made passive tracer SF_6 was shown to be a powerful tool for investigating air mass transport in atmospheric transport models. Second, a serious mismatch in the global bomb radiocarbon budget has been detected, suggesting that the oceans take up 25% less anthropogenic CO_2 than hitherto believed. Third, tracking both the tropospheric and the stratospheric ^{14}C observations during the period of major bomb ^{14}C activity excursions was found to uncover the cycle of air mass through the stratosphere. The above tools were finally used in a first assessment of the seasonal cycles of recent atmospheric $^{14}\text{CO}_2$.

CONTENTS

INTRODUCTION	1
CHAPTER 1 Confining model air mass transport by SF ₆ observations	5
1.1 Introduction	5
1.2 Emission data base and atmospheric observations	6
1.2.1 Krypton 85 (⁸⁵ Kr)	6
1.2.2 Sulfur Hexafluoride (SF ₆)	7
1.3 Model	10
1.3.1 Algorithm scheme	10
1.3.2 Meteorological data fields	11
1.3.3 Free parameter setting	11
1.4 Modeling the meridional distribution of SF ₆	13
1.5 Modeling time series of ⁸⁵ Kr and SF ₆ at selected monitoring stations.....	15
1.5.1 Long-term trends and interannual variations.....	15
1.5.1.1 Krypton 85.....	15
1.5.1.2 SF ₆	17
1.5.2 Seasonal cycles.....	17
1.5.2.1 Krypton 85.....	18
1.5.2.2 SF ₆	19
1.6 Interhemispheric exchange.....	20
1.6.1 Interhemispheric exchange time deduced from observations using a two-box model of the atmosphere	21
1.6.2 Interhemispheric exchange time deduced from the 2D-HD model of the atmosphere.....	22
1.6.3 Seasonal variation of the interhemispheric exchange time	23
1.7 Summary and conclusions.....	23
CHAPTER 2 Global bomb radiocarbon inventory	25
2.1 Introduction	25
2.2 The model tools.....	25
2.2.1 Model of the ocean, the biosphere and the stratosphere.....	26
2.2.2 Initial and boundary conditions	26
2.3 Bomb ¹⁴ C yield and ¹⁴ C budget imbalance.....	28
2.3.1 Bomb ¹⁴ C emissions	28
2.3.2 Missing source or overestimated sink	28
2.4 Possible solutions to the ¹⁴ C imbalance	29
2.4.1 Stratosphere.....	29
2.4.2 Biosphere.....	29
2.4.3 Ocean.....	29
2.5 Summary and conclusions.....	31
CHAPTER 3 Tracing the cycle of air mass through the stratosphere with bomb ¹⁴ C	33
3.1 Introduction	33
3.2 Model	33
3.2.1 Atmosphere	33
3.2.2 Ocean and biosphere	34
3.3 Data	36
3.4 Results: air mass exchange intensity and phase	36
3.5 Applications with beryllium and SF ₆ in the southern hemisphere	37

3.6 Comparison of our findings with present knowledge	38
3.7 Summary and conclusions.....	39
CONCLUSIONS	41
APPENDIX	45
A.1 Carbon and ^{14}C exchange ocean - troposphere.....	45
A.1.1 Air-sea gas exchange and the TM2 carbon fluxes.....	46
A.1.2 Ocean surface $\Delta^{14}\text{CO}_2$ determined from observation.....	47
A.1.3 The radiocarbon exchange between atmosphere and ocean	49
A.1.4 Mean gas exchange rate balancing the bomb ^{14}C inventory.....	50
A.1.5 Remark concerning the definition of the oceanic bomb ^{14}C inventory	51
A.1.6 Preindustrial oceanic ^{14}C uptake and cosmic ray ^{14}C production.....	52
A.1.7 Discussion on k_{ex} and the oceanic ^{14}C inventory.....	52
A.2 Carbon and ^{14}C exchange biosphere - troposphere	53
A.2.1 The mixed biosphere box model	53
A.2.1.1 Cycling of carbon	53
A.2.1.2 Cycling of radiocarbon	55
A.2.1.3 Numerical realization of the mixed biosphere model	56
A.2.2 The statistical biosphere box model	57
A.2.2.1 Basic idea of the statistical model	57
A.2.2.2 Cycling of carbon (no seasonality).....	58
A.2.2.3 Cycling of radiocarbon (no seasonality).....	61
A.2.2.4 Seasonally variable cycling of carbon	65
A.2.2.5 Seasonally variable cycling of radiocarbon	66
A.2.2.6 NPP, decomposition, fertilization, destruction and the TM2 data fields	67
A.2.2.7 Numerical realization of the statistical biosphere model	68
A.2.2.8 Statistical biosphere settings	68
A.3 Complements on the 14-box atmosphere model	70
A.4 Definitions and equations concerning radiocarbon	71
A.4.1 Definition of $\delta^{13}\text{C}$	71
A.4.2 Definition of $\Delta^{14}\text{C}$	71
A.4.3 Isotopic fractionation terminology	71
A.4.4 Interannual variation of ocean surface $\Delta^{14}\text{C}$	72
REFERENCES	75
FIGURES	82
TABLES.....	82
DANKSAGUNG.....	83
LEBENS LAUF.....	84

INTRODUCTION

Life needs carbon. Carbon is assimilated in all living and dead organic tissues and, for example, makes up half the weight of dry wood. On our Earth, however, most of the carbon inventory is stored in sediments. The remaining part is less than one permil of which 93% reside in the ocean, 5% in the land biosphere and only 2% in the atmosphere. Nevertheless, man-made changes in the apparently infinitesimal fraction of atmospheric carbon may have considerable implications and therefore are investigated by an entire community of researchers.

Atmospheric carbon is found mainly in greenhouse gases reflecting thermal radiation back to the Earth surface. More than 99% of the atmospheric carbon inventory is made up by carbon dioxide (CO₂) gas. The rest is essentially methane (CH₄) and carbon monoxide (CO). Atmospheric CO₂ concentrations during the present millennium have been reconstructed from polar ice-core records [*Neftel et al.*, 1985; *Friedli et al.*, 1986; *Siegenthaler et al.*, 1988] and show an accelerating increase since industrialization started, about two centuries ago. This increase mainly is due to fossil fuel burning but also reflects net emissions from land-use change [*Siegenthaler and Oeschger*, 1987]. Direct CO₂ measurements are available in the atmosphere since 1957 [*Keeling and Whorf*, 1994] and show a mean concentration for 1995 of about 360 ppm [*Tans et al.*, 1996] (1 ppm CO₂ corresponds to 10⁻⁶ mole CO₂ per mole of dry air) which is 25% above preindustrial levels. This offset corresponds to a supplementary radiative forcing from CO₂ estimated to be 1.5 W m⁻² or 60% of the total direct climate forcing due to changes in greenhouse gases since preindustrial times [*IPCC1995*, 1996].

What about future concentrations? The yearly CO₂ increase observed in the atmosphere during the 1980s corresponds to a net storage of carbon of about 3 GtC yr⁻¹ (1 gigaton of carbon (GtC) is 10¹² kg of carbon) in the atmosphere. Over the same period, the mean anthropogenic emissions from fossil fuel burning, cement production, gas flaring and land-use change sum up to some 7 GtC yr⁻¹ [*IPCC1995*, 1996]. Thus only 45% of the today's emissions remain in the atmosphere and 55% must be taken up by the land biosphere and the ocean. Anthropogenic excess carbon captured in the ocean and further mixed into the deeper ocean layers is being removed from the atmosphere for centuries or longer whereas the corresponding sequestration potential in the biosphere is still poorly understood. This is why unraveling the distribution of carbon removed from the atmosphere is essential for improving prediction of future CO₂ levels in response to projected fossil fuel consumption scenarios.

Figure 1 illustrates the present day understanding of the global carbon cycle where most of the exchange fluxes are uncertain to at least ±20%. This picture is an immense simplification of the worldwide and seasonally varying real processes. Furthermore Figure 1 shows that natural gross carbon fluxes between the atmosphere and both the ocean and the land biosphere are much larger than the corresponding net uptake fluxes. Hence, confidently determining the fate of fossil fuel CO₂ leaving the atmosphere turns out to be a challenge of considerable complexity. To quantify the global carbon sources and sinks to the atmosphere indirect methods are applied, mainly relying on tropospheric observations of isotopes in CO₂ (¹³CO₂, ¹⁴CO₂, ¹²C¹⁶O¹⁸O). The methods are indirect since they do not validate the exchange by global coverage measurements of fluxes.

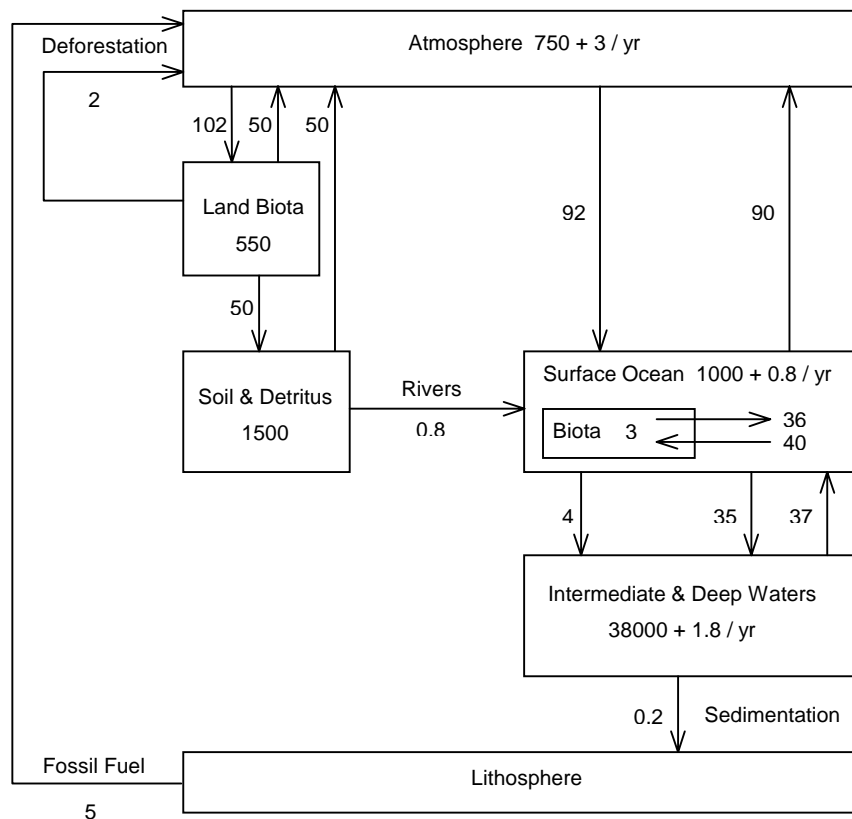


Figure 1 Global carbon reservoirs and fluxes [Levin, 1994]. The numbers apply to the present-day situation (1980-1989). Fluxes, e.g. between atmosphere and surface ocean are gross annual exchanges. Units in GtC for reservoir sizes and in GtC yr⁻¹ for fluxes.

Instead, they use atmospheric transport models to link hypotheses about sources and sinks to the atmospheric CO₂ observations. As the atmosphere is well-mixed if compared to the ocean and the biosphere, it acts as a global scale carbon flux integrator which can be monitored at a reasonable expense.

In the present thesis I report on my model investigations of the Earth's recent carbon system. They rely on the assimilation of worldwide radiocarbon (¹⁴C) observations in simple and gradually refined numerical carbon cycle models. The goal of the study is to progress quantifying, in a globally consistent manner, the mechanisms controlling variations of the isotopic ¹⁴C/C ratio of CO₂ observed in the free troposphere after the 1980s. Inversely, this study also inquires the potential of high precision atmospheric ¹⁴CO₂ observations to constrain the general carbon budget. Before comparing predicted values with observations a prerequisite of any atmospheric transport model is its capability of simulating air mass transport processes correctly. Chapter 1 demonstrates how I investigated this property in our two-dimensional atmospheric transport model using new sulfur hexafluoride (SF₆) tracer data. In the same breath SF₆ was shown to be a powerful transport tracer for other atmospheric applications.

The two-dimensional model with air mass transport validated by SF₆ observations then was started from observed initial conditions in 1970. Using simple but at that time reliable carbon isotope exchange fluxes to the ocean and the biosphere the two-dimensional model could not reproduce tropospheric ¹⁴CO₂ observations. These observations reflect a disequilibrium of ¹⁴C

activity between the troposphere and the actively connected carbon reservoirs. The disequilibrium mainly results from nuclear bomb tests in the early 1960s. Obviously, the remnant amount of bomb ^{14}C in the ocean, the biosphere and the stratosphere had to be better determined to successfully implement ^{14}C as a tracer in global carbon cycle modeling. This approach initially was hampered by the large uncertainty range found in the literature concerning the yield of bomb ^{14}C from nuclear blasts. Chapter 2 shows how I was able to solve this problem and to budget the global bomb radiocarbon inventory. Excitingly, at the term of this second part of my thesis we were faced with a major imbalance within the global carbon cycle. The long term atmospheric $^{14}\text{CO}_2$ observations can not be consistently linked with oceanic and biospheric exchange fluxes within their individual range of uncertainty. A reduction by 25% of the gross carbon exchange fluxes to the ocean was identified as most appropriate candidate to solve the mismatch. However, this contradicts the total bomb ^{14}C budget in the ocean obtained from the global GEOSECS survey during the 1970s and still assumed to be uncertain within only $\pm 10\%$ [Broecker *et al.*, 1995].

To untangle this complication I focussed my investigations from the interannual to the seasonal time scale. Here I was confronted with the need to parameterize the vertical cross-tropopause exchange accurately because (1) the source of natural and bomb ^{14}C is, to a large extent, located in the stratosphere, and, (2) the stratospheric-tropospheric air mass exchange (STE) is modulated strongly during the course of a year with corresponding seasonal impact on tropospheric $^{14}\text{CO}_2$. The complex nature of STE, consisting of many scales from small-scale eddy transport to large-scale Hadley Cell circulation, is not well understood yet. It is, therefore, not a matter of vertical resolution that general atmospheric circulation models show a poor quantitative prediction of STE. Hence our two-dimensional model was not helpful here because its vertical transport is mainly adopted from fields of a three-dimensional model which has proved inadequacies in its STE processes [Rehfeld and Heimann, 1995]. Therefore I developed a simple 14-box diffusion model of the atmosphere and determined its stratospheric air mass cycling by matching the tropospheric and stratospheric $^{14}\text{CO}_2$ observations during the period of main nuclear bomb ^{14}C excursions. This part of my thesis is presented in the final Chapter 3. In the conclusions I also briefly discuss seasonal $^{14}\text{CO}_2$ results between 1985 and 1995 obtained using this robust atmospheric model together with carbon isotope fluxes from the ocean and the biosphere detailed in the appendix.

CHAPTER 1 Confining model air mass transport by SF₆ observations

1.1 Introduction

Atmospheric transport models are considered a powerful tool to investigate biogeochemical cycles of trace constituents such as carbon dioxide or methane. As they link hypotheses about sources and sinks to atmospheric observations, a crucial prerequisite of these models is their capability to correctly simulate atmospheric transport processes. The transport behavior of atmospheric models is, therefore, often tested through so-called atmospheric transport tracers and their global distributions. The radioactive isotopes krypton 85 (⁸⁵Kr) and radon 222 (²²²Rn) as well as inert (long-lived) halocarbons are the classical tracers for this purpose [Jacob *et al.*, 1987; Prather *et al.*, 1987; Heimann and Keeling, 1989; Zimmermann *et al.*, 1989; Feichter and Crutzen, 1990; Tans *et al.*, 1990] as they have relatively well-defined source-sink characteristics, and their global atmospheric distributions have been thoroughly measured [Weiss *et al.*, 1992; Cunnold *et al.*, 1994].

Recently, a new tracer gas has been added to this potpourri, namely the solely man-made and steadily increasing trace gas sulfur hexafluoride (SF₆) [Maiss and Levin, 1994]. Quasi-continuous atmospheric observations of SF₆ are now available for several years from globally distributed sites in the northern (Alert 82°N, Fraserdale 50°N, Izaña 28°N) as well as in the southern hemisphere (Cape Grim 41°S, Neumayer 71°S) [Maiss *et al.*, 1996]. This observational SF₆ data base was now used in combination with global observations of ⁸⁵Kr [Weiss *et al.*, 1992] in a simple exercise performed with our two-dimensional model of atmospheric transport (2D-HD model (HD = Heidelberg)), [Hesshaimer *et al.*, 1989; Hesshaimer, 1990]. Meridional and vertical profiles as well as long term trends and seasonal cycles have been compared with observations.

Our purpose was threefold: (1) We wanted to investigate the behavior of the new tracer SF₆ in direct comparison to the classical global tracer ⁸⁵Kr. SF₆ has a totally different source distribution, namely, it is emitted in industrialized areas from a large number of almost continuously distributed sources, in contrast to ⁸⁵Kr which has only a small number of point sources, mainly situated in the northern hemisphere. (2) Through the comparison with ⁸⁵Kr, namely, fine-tuning the transport parameters of our model with ⁸⁵Kr observations, we wanted to test the hypothesis that the global SF₆ source distribution is closely related to electrical power production. By this we could provide a realistic source characterization of SF₆, necessary for future use of this tracer in more sophisticated three-dimensional transport models. (3) We wanted to assess potential shortcomings in the investigation of global trace gas budgets using two-dimensional model results which, for problems related to atmospheric variations observed on hemispheric scales, are often distinct enough if compared to three-dimensional models. Among others, this assessment is relevant when using our 2D-HD model to simulate the global distribution and temporal change of atmospheric ¹⁴CO₂ which has only a limited observational data base [Levin *et al.*, 1992] but can provide important constraints on the global carbon budget [Hesshaimer *et al.*, 1994].

1.2 Emission data base and atmospheric observations

1.2.1 Krypton 85 (⁸⁵Kr)

The radioactive noble gas ⁸⁵Kr today is mainly released to the atmosphere through nuclear fuel reprocessing plants (NFRPs). Its only relevant sink is radioactive decay with a mean radioactive life time of 15.6 years. All known NFRPs are located in the northern hemisphere between 33°N and 56°N; their locations are given in Table 1. Nevertheless, observational evidence at the two midlatitude southern hemispheric stations Cape Point (34°S) and Cape Grim (41°S) [Weiss *et al.*, 1992] clearly demonstrates that there must be one or several yet unidentified ⁸⁵Kr sources located in the southern hemisphere. Yearly mean ⁸⁵Kr emission rates from the eight major NFRPs in the western world until 1986 as summarized in have been compiled by Rath [1988]. More updated

Plant	1975	1976	1977	1978	1979	1980	1981	1982	1983	1984	1985	1986	1987	1988
1. Hanford, USA (46.6°N, 114.7°W)	294	250	108	291	283	276	212	95	214	268	251	251 ^e	251 ^e	251 ^e
2. Idaho, USA (43.4°N, 112.1°W)	24	33	111	101	0	92	59	9	3	0	0 ^e	0 ^e	0 ^e	0 ^e
3. Savannah, USA (33.3°N, 81.7°W)	520	711	448	530	480	580	840	515	698	698	700	700 ^e	700 ^e	700 ^e
4. Sellafield, UK (54.6°N, 3.6°E)	1200	1200	800	700	940	840	1400	1190	1129	1003	643	1441	919	1076
5. Marcoule, France (44.4°N, 4.5°E)	100	92	117	308	280	535	310	310	620	600	600 ^e	600 ^e	600 ^e	600 ^e
6. La Hague, France (49.0°N, 0.9°W)	657	343	669	786	642	825	969	1220	1356	730	1900	784	946	730
7. Karlsruhe, Germany (49.0°N, 8.4°E)	43	86	115	34	51	32	70	16	76	32	92	83	83 ^e	83 ^e
8. Tokai-Mura, Japan (36.5°N, 140.6°E)	0	0	0	60	0	280	110	190	90	180	270	351	324	73
9. Kyshtym, Russia (55.7°N, 60.6°E)														
Zimmermann <i>et al.</i> ^a	1440	2100	3070	3140	3660	3080	2620	3200	3020	4720 [*]	4930 [*]
This work ^d	1439	2109	3062	3136	3651	3069	2626	3212	3056	4905	4787	4834	5416	4764
<i>Total Source</i>														
Zimmermann <i>et al.</i> ^a	4278	4815	5438	5950	6336	6540	6590	6745	7388	8051	9116
Jacob <i>et al.</i> ^b	6000	6130	6270	6400	6530	6660
Heimann and Keeling ^c	4397	4782	5261	5765	6211	6524	6661	6648	6628
This work ^d	4277	4824	5430	5946	6327	6529	6596	6757	7424	8416	9243	8837	8657	8929

Table 1 Yearly mean ⁸⁵Kr emissions 1975 - 1988 for individual NFRPs and model-estimated global emissions all in 10³ Ci yr⁻¹. NFRP, nuclear fuel reprocessing plant. Releases for 1975-1986 from plants 1-8 were taken from Rath [1988], except for Tokai-Mura, where 1985 and 1986 emissions were taken from UNSCEAR [1993]. The 1985 and 1986 emissions for Sellafield and La Hague reported by Rath [1988] which were taken from von Hippel *et al.* [1986] compare within ±1% with those given in UNSCEAR [1993]. 1987 and 1988 emissions from Sellafield, La Hague and Tokai-Mura were also taken from UNSCEAR [1993].

^aModel-calculated values taken from Zimmermann *et al.* [1989, Figure 1a]; asterisk, value calculated with zero release from Tokai-Mura.

^bJacob *et al.* [1987].

^cHeimann & Keeling [1989].

^dThis work: emission values were compiled for a 5.06 * 10¹⁸ kg of air atmosphere [Prather *et al.*, 1987]; the model run was started at January 1st, 1975, with a uniform ⁸⁵Kr concentration of 0.525 Bq m⁻³.

^eValue set equal to the previous value.

numbers for La Hague, Sellafield and Tokai-Mura are reported in *UNSCEAR* [1993]. For overlapping periods, they compare within $\pm 1\%$ with the numbers compiled by *Rath* [1988]. Direct emission rates from Kyshtym (Russia) are not available yet. The values of *Zimmermann et al.* [1989] and our estimates listed in Table 1 (9a, d) have been calculated as the difference between the respectively determined total emissions and the known releases from the western plants 1-8. *Zimmermann et al.* [1989] calculated the total emissions from their model, and we derived them likewise (as listed in Table 1) from the observed temporal change of the global atmospheric ^{85}Kr inventory. For comparison, Table 1 also shows the total ^{85}Kr releases calculated by *Jacob et al.* [1987] and by *Heimann and Keeling* [1989]. The spatial distribution of the ^{85}Kr sources for our model estimates was set according to the latitudes and strengths of plants 1-9 (Table 1).

Continuous observations of ^{85}Kr at several worldwide distributed stations are performed by the Institut für Atmosphärische Radioaktivität, Freiburg, Germany, and the data till end of 1988 have been published by *Weiss et al.* [1992]. In the northern hemisphere, we used the weekly integrated long-term observations at Miami (25°N, 10m a.s.l.: 1981-1988) and at Schauinsland (48°N, 1200 m a.s.l.: 1980-1988) for comparison with model simulations. In the southern hemisphere, only weekly grab samples from Neumayer station (Antarctica 71°S, 42m a.s.l., 1982-1987) were compared with model simulations, to determine the long-term trend and to investigate the seasonal cycle.

Nine observed meridional ^{85}Kr profiles sampled during ship cruises over the Atlantic ocean at about 30°W between 1980 and 1987 [1992] were used in addition to the quasi-continuous long-term station data. To allow direct intercomparison, observed and model calculated profiles were normalized to October 1st, 1983, by the following procedure: We calculated the long term trend through the Neumayer observations (see Figure 5a) and added the difference in the long term fit values for Neumayer between October 1st, 1983, and the respective observation date to each observational ship cruise value. This method partly compensates the statistical uncertainty of individual profiles reflecting variations in meteorology not resolved in our 2D-HD model. Moreover, it takes into account the overall increase of interhemispheric concentration gradients, caused by a 50% overall increase of the source strength between 1980 and 1987.

Observed vertical ^{85}Kr profiles are only available for the small latitudinal zone between 43°N and 45°N (1°W - 3°E), namely southern France. A mean observed vertical profile, normalized to January 1st, 1986, was calculated from the data in Table A-III of *Weiss et al.* [1992] for comparison with our model results at the respective latitude (compare Figure 3).

1.2.2 Sulfur Hexafluoride (SF_6)

Sulfur hexafluoride (SF_6) is a very long-lived (atmospheric life time $\tau > 800$ years [*Morris et al.*, 1995]) purely anthropogenic atmospheric trace gas. Its mean concentration in the atmosphere has increased by about two orders of magnitude in the last two decades, exceeding 3 ppt at the end of 1994 [*Maiss and Levin*, 1994; *Maiss et al.*, 1996]. About 80% of the global SF_6 release are presumably due to leakages, etc. in electrical insulations and switching, and the remaining 20% mainly come from degassing and purifying molten reactive metals [*Stordal et al.*, 1993]. The estimated mean banking time between production and release today is approximately 10 years [*Maiss and Levin*, 1994]. Due to these source characteristics, the global distribution of SF_6 emissions is closely coupled with the global distribution of electrical power production. SF_6

emissions are, thus, quite continuously distributed over the world's industrialized areas, herein contrasting with the punctual ⁸⁵Kr emissions. The atmospheric lifetime of SF₆ with respect to chemical destruction in the mesosphere, and dissolution losses in the world oceans is larger than 800 years [Ko *et al.*, 1993; Ravishankara *et al.*, 1993; Morris *et al.*, 1995]. This long lifetime is of great advantage for the application of SF₆ as atmospheric transport tracer if compared to halocarbons: The uncertainty upon atmospheric lifetimes of chlorofluorocarbons introduces additional errors when using them to validate atmospheric transport models [Prather *et al.*, 1987].

Quasi-continuous two-weekly integrated high-accuracy atmospheric SF₆ observations at three background stations in the northern hemisphere (Alert 82°N, 187m a.s.l., 1993-1994; Fraserdale 50°N, 200m a.s.l., 1994; Izaña 28°N, 2367m a.s.l., 1991-1994) and spot measurements of SF₆ from two background stations in the southern hemisphere (Cape Grim 41°S, 95m a.s.l., 1978-1994; Neumayer 71°S, 42m a.s.l., 1986-1994) as well as from two meridional profiles of SF₆ over the Atlantic ocean from 40°N to 71°S have recently been reported by Maiss and Levin [1994] and Maiss *et al.* [1996]. These data form the observational basis for our comparison with SF₆ model results.

Year	Q_{SF_6}	Year	Q_{SF_6}
1970	0.730	1982	3.302
1971	0.940	1983	3.518
1972	1.152	1984	3.735
1973	1.364	1985	3.951
1974	1.578	1986	4.168
1975	1.792	1987	4.38
1976	2.007	1988	4.602
1977	2.222	1989	4.818
1978	2.437	1990	5.035
1979	2.653	1991	5.252
1980	2.869	1992	5.469
1981	3.085	1993	5.686

Table 2 Yearly SF₆ emission rates (Q_{SF_6} [10^6 kg SF₆ yr⁻¹]) as used in the 2D-HD model. Emission values were compiled for a $5.06 \cdot 10^{18}$ kg of air atmosphere [Prather *et al.*, 1987], the model run was started at January 1st, 1970, with a uniform SF₆ mixing ratio of 0.036 ppt.

Maiss and Levin [Maiss and Levin, 1994] reported global mean SF₆ emission rates increasing linearly with time from 1970 onwards with an estimated value of $5 \cdot 10^6$ kg SF₆ per year around 1990. This estimate is based on the long term quadratic concentration increase observed at Neumayer station. For the SF₆ model run presented here we calculated the time development of the global mean emission rate for 1970 to 1993 in a similar way as for ⁸⁵Kr: SF₆ emission rates were derived from the change of the global atmospheric SF₆ inventory by using the quadratic concentration increase trends at Neumayer, Cape Grim and Izaña. We accounted for the stratosphere, containing 15% of the atmospheric air mass, with a mean lag time of 2.5 years, but assumed no loss of SF₆ due to chemical destruction or other processes. A linear increase with time of the global mean SF₆ emission starting in 1967 according to Q_{SF_6} [10^6 kg yr⁻¹] = $4.913 + 0.2133 \cdot t$, t = years after 1990.0 fits the observed quadratic increase in the atmosphere

reasonably well. To account for small interannual concentration variations, source strengths slightly different from this linear curve have been used in our model estimates. These yearly release rates are listed in Table 2. A total atmospheric mass of $5.06 * 10^{18}$ kg air was used for this source strength estimate. The meridional distribution of the nearly linearly rising SF₆ source was assumed to be equivalent to the meridional distribution of electrical power production used by *Prather et al.* [1987] to determine the emission pattern of halocarbons (Table 3). No temporal change of this distribution was assumed during the modeled period, although one may expect slight changes of the relative contributions (NH: 95%, SH: 5%) from the respective hemispheres from the 1970s throughout the 1990s.

Box No.	Latitude Belt	Percent Emission
1	-90 to -86.1 (south)	0
2	-86.1 to -78.3	0
3	-78.3 to -70.4	0
4	-70.4 to -62.6	0
5	-62.6 to -54.8	0
6	-54.8 to -47.0	0
7	-47.0 to -39.1	0
8	-39.1 to .31.3	2.22
9	-31.3 to -23.5	2.22
10	-23.5 to -15.7	0.74
11	-15.7 to -7.8	0
12	-7.8 to 0	0
13	0 to 7.8	0
14	7.8 to 15.7	1.48
15	15.7 to 23.5	2.96
16	23.5 to 31.3	4.44
17	31.3 to 39.1	21.48
18	39.1 to 47.0	25.19
19	47.0 to 54.8	28.89
20	54.8 to 62.6	10.37
21	62.6 to 70.4	0
22	70.4 to 78.3	0
23	78.3 to 86.1	0
24	86.1 to 90 (north)	0

Table 3 Meridional distribution of SF₆ emissions in percent of the global mean.

1.3 Model

The two-dimensional Heidelberg model of atmospheric transport (2D-HD model) has been developed to allow first order comparisons between its results and observations [Hesshaimer, 1990]. It also provides pre-constraining estimates for the results to be obtained by more sophisticated three-dimensional models. The model has been developed in cooperation with the Max-Planck Institut (MPI) für Meteorologie in Hamburg [Heimann,]. It was designed to work on any IBM PC compatible computer.

1.3.1 Algorithm scheme

All physical parameters of the Earth atmosphere are represented in the model as zonally averaged means, thus reducing the modeling space to two dimensions. Subdividing the atmosphere into boxes, the algorithm computes the air mass transport between these boxes on the basis of observed meteorological data. This scheme is appropriate to describe the mass flow transport of any tracer, as long as the main transport medium is the air. The model bases on a zonally integrated version of the continuity equation:

$$\int_{\Sigma} \cos(\theta) \partial_t (\rho c) d\sigma + \int_{\partial\Sigma} \cos(\theta) \rho V c d\eta - \int_{\partial\Sigma} \cos(\theta) \rho K (\nabla c) d\eta + CONVEC = \int_{\Sigma} \cos(\theta) Q_{vol} d\sigma + \frac{Q_{rest}}{2\pi R} \quad (1)$$

- Σ : box surface;
- $d\sigma$: surface element (scalar);
- $\partial\Sigma$: border of box surface (scalar);
- $d\eta$: border element (vector);
- θ : degree latitude;
- ρ : mean air density;
- c : mean mass of tracer per mass of air;
- V : mean wind velocity ($V = v, w$);
- K_{ij} : diffusion tensor;
- Q_{vol} : volume sources;
- Q_{rest} : additional sources;
- R : Earth radius;
- CONVEC: vertical convection (see text).

The horizontal transport is derived from meridional wind fields (v) and horizontal diffusion (K_{yy}), whereas the vertical transport depends on vertical wind fields (w), vertical diffusion (K_{zz}) and vertical convection (CONVEC). Horizontal and vertical diffusion terms account for the temporal and spatial averaging when the real wind data is mapped into the model grid. The diffusion coefficients were set to be proportional to the standard deviations (σ_v , σ_w) of the input wind fields. The off-diagonal elements of the diffusion tensor are set to zero according to *Zimmermann et al.* [1989]. The term labeled CONVEC represents vertical transport arising from dry and moist convective processes which are not resolved in the model's wind field. The explicit CONVEC scheme consists of a redistribution of mass between the boxes in a vertical air column during the model's time step [see *Prather et al.*, 1987].

1.3.2 Meteorological data fields

The model grid and the data fields bear strong resemblance to a three-dimensional atmospheric CO₂ transport model (TM2) in use at the MPI in Hamburg [Heimann and Keeling, 1989]. The model grid subdivides the atmosphere horizontally into 24 segments leading from South Pole to North Pole and vertically into 9 layers covering the range between 984 hPa and 10 hPa. The limits of the boxes are the same as the corresponding limits in the TM2. The wind field (v , w) and standard deviation data (σ_v , σ_w) used in our model are the zonally and monthly averaged TM2 fields (originally data from the Global Weather Experiment, see Heimann and Keeling [1989]), and are based on observations between December 1978 and November 1979. Besides the problem of data availability, it does not make too much difference to use real time meteorological data for this study. The real time wind fields when averaged longitudinally to two dimensions would be considerably smoothed out anyhow, and the 1978-1979 data set is quite representative for mean conditions.

Our CONVEC data (monthly averages) are the zonal means of the TM2 models (originally described by Prather *et al.* [Prather *et al.*, 1987]), corrected for the time step used in our model. The air density data (monthly averages) have been computed on the basis of temperature and pressure fields [Houghton, 1977]. The meridional wind data field (v) has been slightly modified to insure air mass conservation in each air column of the model. The vertical wind field (w) was then deduced from the horizontal wind data field to insure air mass conservation in each box of the model.

1.3.3 Free parameter setting

Tuning of the 2D-HD model was performed by determining optimal values for the only free parameters which we decided to take: the diffusion fields (K_{yy} , K_{zz}). These were determined by multiplying, respectively, the horizontal and vertical wind variances at each grid point i,j (σ_v , σ_w) _{ij} (not CONVEC) with two constants a_v and a_w . In a first step, we fixed a_v and a_w to obtain a plausible diffusion field (compare e.g. Hyson *et al.* [1980]). In a second step, we made profit of the similitude between the TM2 and our 2D-HD model: A parallel ⁸⁵Kr run of the two models was used to get improved values for the parameters a_v and a_w . The final fine tuning of a_v and a_w was achieved by fitting optimally to observed meridional ⁸⁵Kr profiles.

Figure 2 shows the comparison of our ⁸⁵Kr model results with the cruise data (both data sets normalized to October 1st, 1983; see data description above). The maritime ⁸⁵Kr observations over the Atlantic ocean are not zonal means. However, due to the rather strong longitudinal mixing from west to east at the latitude of the major sources, these data are still a very good approximation of the real zonal mean, at least south of the major ⁸⁵Kr source regions. On the other hand, adjusting the air mixing in our 2D-HD model to maritime observations makes it more reliable to correctly model other trace gases (e.g. CO₂ or CH₄) where observations are also biased towards maritime stations [e.g. Conway *et al.*, 1994]. The model results in Figure 2 were obtained by optimum adjustment (least squares fitting to observations) of only the horizontal diffusion parameter a_v . However, with this tuning we also obtained good agreement between the observed vertical distribution and our model results as shown in Figure 3. The corresponding parameters a_v and a_w from this "fine-tuned" model run were, therefore, adopted for all further ⁸⁵Kr and SF₆ runs which allow for a direct comparison of both transport tracers.

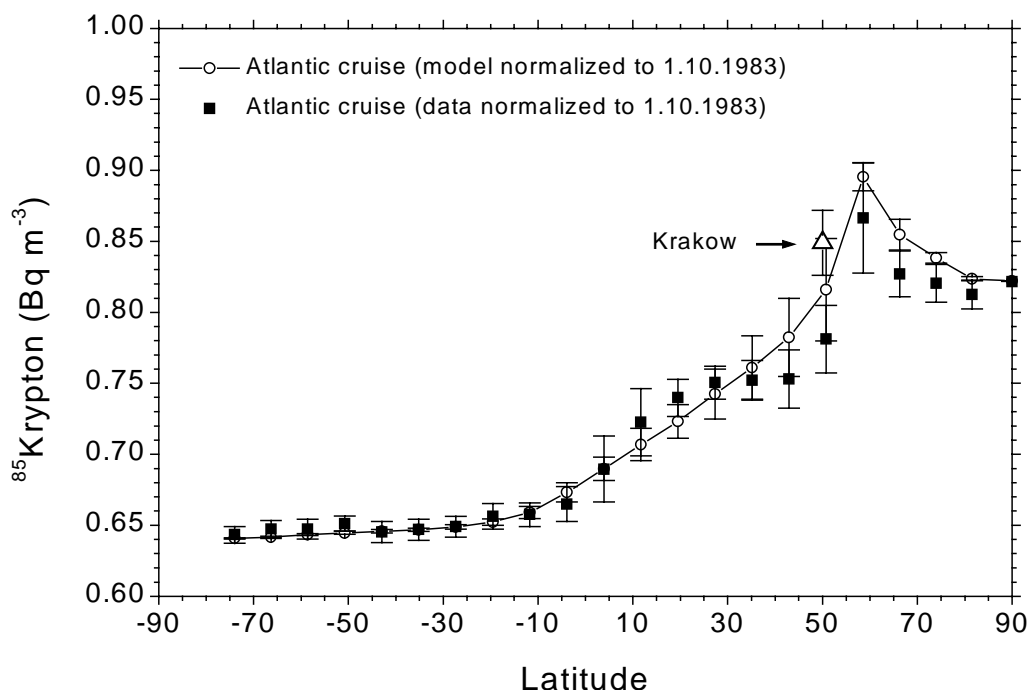


Figure 2 Comparison of meridional ^{85}Kr profiles at ground level. Full squares: mean observed cruise data over the Atlantic ocean for each of the meridional model box latitudes normalized to October 1st, 1983 (see text). The open up triangle represents the mean value and standard deviation observed at Kraków station, Poland (220m a.s.l.), between mid September and mid October 1983. Open circles, mean concentrations as calculated by the 2D-HD model for the individual dates where cruise data exist, also normalized to October 1st, 1983. Error bars correspond to the standard deviation of the individual observations/model results.

Refined inspection of the model results in comparison with the observations provides several important features to be discussed: North of about 40°N the 2D-HD model ^{85}Kr results - although qualitatively reproducing the latitudinal pattern with a maximum at about 55°N - still shows systematically higher values than observed over the Atlantic ocean. The reason for this discrepancy is that the model results represent real zonal mean concentrations which are, particularly north of 40°N strongly influenced by the continental ^{85}Kr pile up close to the large point sources. To illustrate this fact, we included the observed mean ^{85}Kr level in Central Europe represented by measurements at the most eastern station Kraków (Poland, 50°N , 20°E , 220m a.s.l.) for mid September to mid October 1983 and its standard deviation in Figure 2. There is, indeed, a general substantial ^{85}Kr pile up of $0.05\text{-}0.1\text{ Bq m}^{-3}$ observed at this continental site if compared to Atlantic Ocean levels. We, therefore, come to the (trivial) conclusion that our 2D-HD model will neither simulate maritime nor continental ^{85}Kr concentration levels in mid northern latitudes correctly, at least for the lowest tropospheric levels between 40° and 70°N (see, however, SF₆ results below). At 50°N , the model results do, however, seem to represent the observed zonal mean accurately, if estimated as lying between the mean of Atlantic Ocean and Kraków observations.

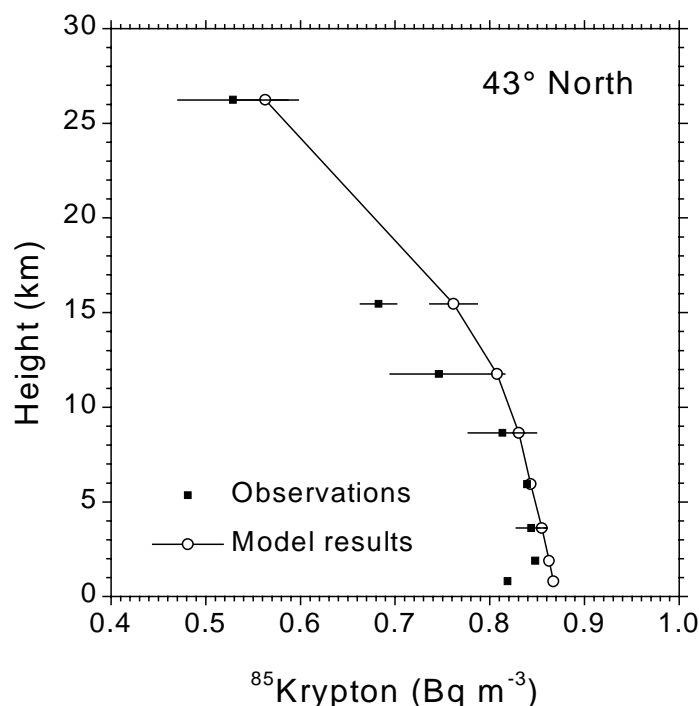


Figure 3 Comparison of vertical ⁸⁵Kr profiles for 43°N. Full squares: concentrations observed over France, averaged for each box level, and normalized to January 1st, 1986. Circles, mean of model calculated values for each individual observation normalized to January 1st, 1986. Error bars correspond to the standard deviation of the individual observations/model results.

1.4 Modeling the meridional distribution of SF₆

Once the 2D-HD model was optimized through observed ⁸⁵Kr profiles, we could simulate the meridional distribution of SF₆ using the emission scenario described above and listed in Tables 2 and 3. Figure 4a compares the observed meridional profile collected at the end of 1993 over the Atlantic ocean [Maiss *et al.*, 1996] with the results calculated by the model for the lowest tropospheric box layer. Mean SF₆ concentrations for the end of 1993 (October - December) observed at Alert (82°N), Izaña (28°N), Cape Grim (41°S) and Neumayer (71°S) [Maiss *et al.*, 1996] are also included in Figure 4a. The height of all stations except Izaña lies within the lowest model layer. To inspect the model predicted vertical decrease of concentration with height due to the ground location of the SF₆ sources, we also included the model estimate for 2367m a.s.l. at the latitude of Izaña in Figure 4a. The predicted difference matches the difference between observations at Izaña station and corresponding ship based measurements, but this needs to be confirmed when more data will be available.

Figure 4b shows the meridional distribution of the yearly mean SF₆ concentrations in 1993 in comparison with model estimates. Here we also included a value for Fraserdale (50°N) which was extrapolated back from the observations during 1994. We used the mean difference of Fraserdale and Izaña in 1994 (0.14 ppt) and the trend from the Izaña curve to estimate that value. The general good agreement between SF₆ observations and our model results confirms that tuning horizontal diffusion with the observed SF₆ profile would provide a very similar value for

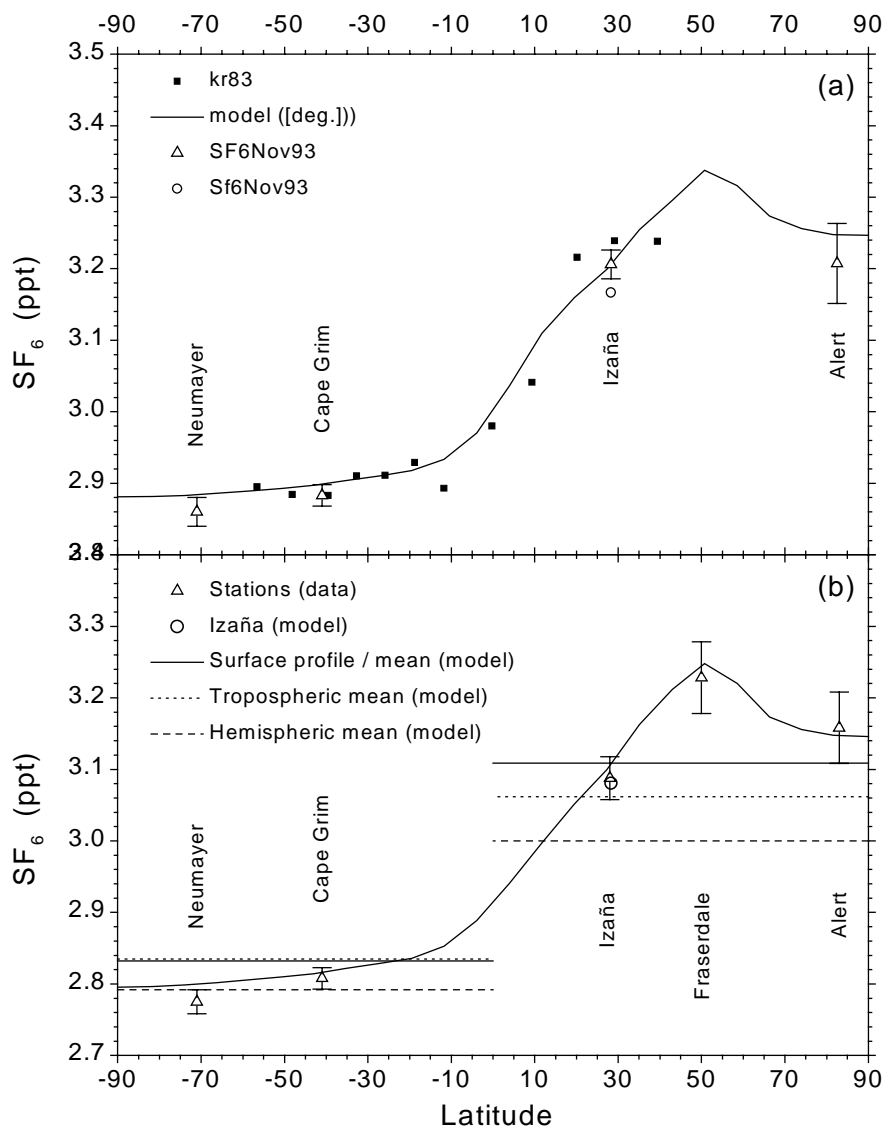


Figure 4 (a) Comparison of meridional SF₆ profiles for November 1993. Full squares: observations over the Atlantic ocean. Open up triangles, mean station data for October to December 1993. Solid line, estimates for the model's surface layer. Circles, model estimate for Izaña station (2367m a.s.l.). (b) Comparison of 1993 yearly mean meridional profiles of SF₆. Open up triangles, yearly means of station observations. The value for Fraserdale was extrapolated back from the observations during 1994, using the mean difference to Izaña in 1994 (0.14 ppt) as offset from the mean value for Izaña in 1993. Circle, model estimate for Izaña station. Solid line: model calculations for the meridional profile respectively hemispheric means (horizontal lines) at the model's surface layer. Short-dashed horizontal lines, hemispheric means as calculated by the 2D-HD model for the respective troposphere; long-dashed horizontal lines, total hemispheric means. Error bars of the station data correspond to the mean standard deviations around individual trend curves (see Figure 6).

the model's free parameter a_v . The data from Fraserdale, if they are representative for the mean SF₆ concentration at about 50°N, also nicely confirm the model predictions at the latitude where the strongest sources are located.

Also the observations at Alert (82°N), at very high northern latitudes are correctly reproduced

by our 2D-HD model. This was not so obvious for ^{85}Kr north of about 60°N (see Figure 2), and may, in fact, be due to the more uniform release of SF_6 on the northern hemispheric continents and to missing significant sources north of about 65°N . This finding is very promising with respect to the validity of our 2D-HD model for CO_2 and $^{14}\text{CO}_2$ simulations for Alert and comparison with the respective observations (see *Levin et al.* [*Levin et al.*, 1992]) (but perhaps does not hold for CH_4 due to the high northern wetland sources still significant at latitudes north of 65°N). It is interesting to note from Figure 4b that the model estimated mean ground level difference between the two hemispheres (solid horizontal line) nearly exactly represents the yearly mean SF_6 concentration difference observed between Izaña in the northern hemisphere and Cape Grim in the southern hemisphere.

1.5 Modeling time series of ^{85}Kr and SF_6 at selected monitoring stations

Beside meridional and vertical profiles, we also compared concentration records of ^{85}Kr and SF_6 at individual stations with the 2D-HD model results. In order to compare the potentially different behavior of the two tracers ^{85}Kr and SF_6 with considerably different source distributions, it would be ideal to choose stations where long term continuous measurements of both tracers have been published. Unfortunately, this is only the case for Neumayer station in Antarctica. Among all published northern hemispheric long term ^{85}Kr records, Miami (25°N , 10m a.s.l.) shows the smallest influence from air masses with very high concentrations. These "spiked" air masses are not representative for their latitude as they were poorly dispersed longitudinally on the way from the respective NFRP point source. ^{85}Kr observations at Miami can be compared with SF_6 model results at Izaña at approximately the same latitude, but located in the free troposphere (28°N , 2367m a.s.l.). At Miami, ^{85}Kr observations from 1981 to 1988 have been published [*Weiss et al.*, 1992], a time span which, however, does not overlap with the time span of published SF_6 data from Izaña (1991-1994) [*Maiss et al.*, 1996]. Even if the time spans for ^{85}Kr and SF_6 do only slightly or even not at all overlap, intercomparison of the general temporal behavior of both tracers is still feasible. This makes sense, as we, anyhow, do not use the actual meteorological data in individual years for the model estimates of trace gas concentrations.

Because of their vicinity to the sources, northern hemispheric stations need, however, a minimum of 4-5 years of continuous observations until we are able to pick up a mean seasonal behavior of SF_6 or ^{85}Kr with confidence. The Izaña, Fraserdale and Alert SF_6 records are, thus, still too short, and their mean seasonal cycles show too much variance to be compared with the model estimates. To compare the seasonal cycles of model results with long-term observations at Miami and Neumayer for ^{85}Kr , and at Neumayer for SF_6 , we calculated monthly mean values, deduced the long term trends and determined mean seasonal cycles by least squares curve fitting to a polynomial and harmonic function according to *Thoning et al.* [1989].

1.5.1 Long-term trends and interannual variations

1.5.1.1 Krypton 85

Figures 5a and 5b compare the interannual variations of ^{85}Kr observed at Neumayer, Miami and Schauinsland with the corresponding 2D-HD model results. For comparison with the model results, the data from Miami have been selected to flag obvious outliers respectively samples that were influenced by direct emission plumes of nuclear fuel reprocessing plants. We rejected spikes more than 20 mBq higher than the original data filtered 60 times with a recursively applied binomial filter ($y_i' = 1/4 \cdot (y_{i-1} + 2y_i + y_{i+1})$). For Neumayer and Miami (Figure 5a) the observed

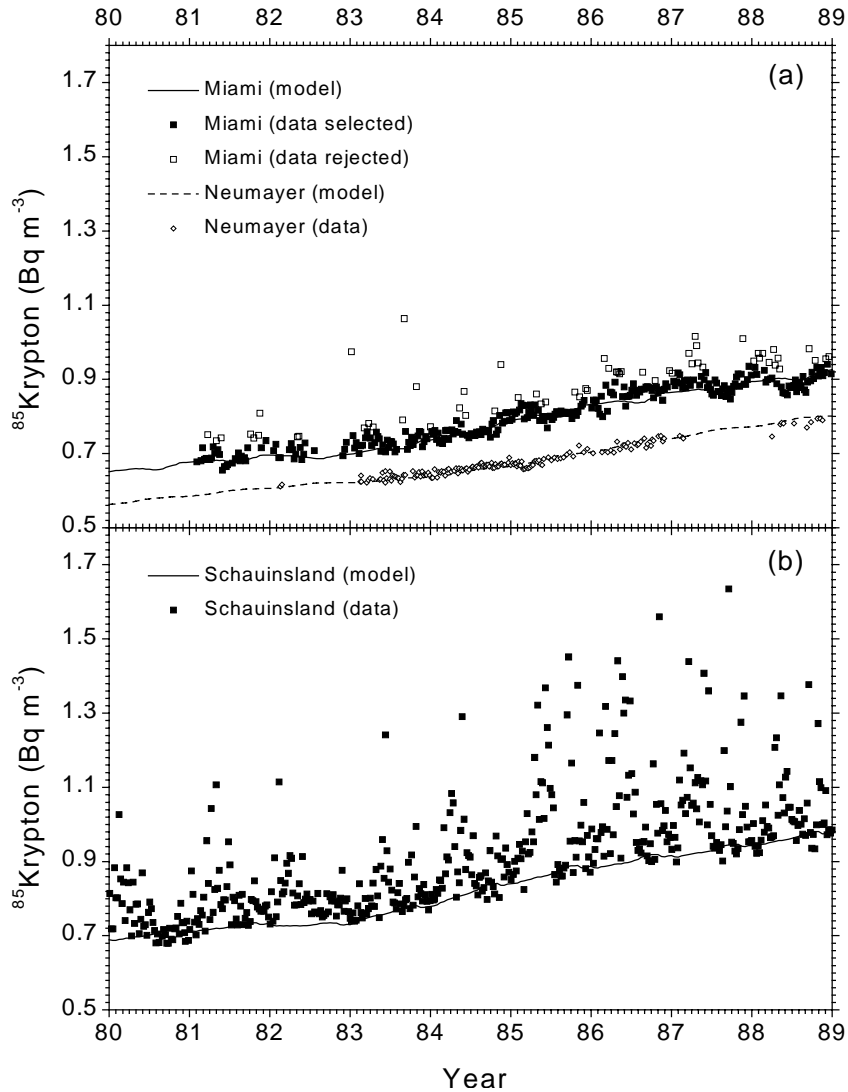


Figure 5 (a) Comparison of observed weekly integrated (individual data points) and model estimated (curves) long-term trends of ^{85}Kr at Neumayer station and Miami. For a more reliable comparison with model results, the Miami data have been selected for obvious outliers (plumes from nuclear fuel reprocessing plants; see text). (b) Same as (a) except for the continental site Schauinsland.

absolute concentration level and the long term increase are correctly reproduced by the model. For the most remote station Neumayer at the Antarctic coast this is, however, not surprising as the global ^{85}Kr emissions had been derived from the time development at Neumayer station, and the meridional diffusion parameter had been adjusted in the model to reproduce shipboard measurements over the Atlantic ocean including observations at Neumayer. The good agreement between model and observations found for Miami, however, underpins both, the representativeness of this station for the mean concentration at this latitude with respect to ^{85}Kr and the ability of the model to correctly predict the offset from Neumayer. As expected, however, our 2D-HD model is not able to reproduce the observed spikes resulting from direct transport of ^{85}Kr plumes from individual point sources to the observation site.

The effect of continental and regional ^{85}Kr sources is most obvious in the observations at the

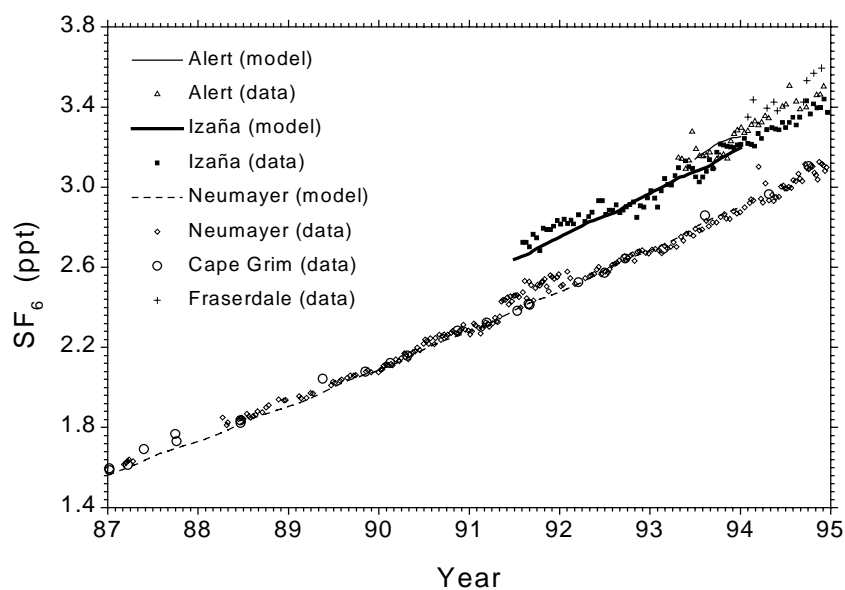


Figure 6 Comparison of observed (individual data points) and model estimated (curves) long term trends of SF_6 concentration for northern and southern hemispheric sites.

Schauinsland station. Here the ^{85}Kr model estimates can only reproduce the lower envelope of observations (Figure 5b). The large seasonality seen in the data with pronounced maxima in summer and autumn which are caused by enhanced vertical mixing over the continent and therewith transport of ground level pollutants to the mountain site cannot be reproduced by the model. This feature of our 2D-HD model had already been identified when simulating the seasonal amplitude of CO_2 at the Schauinsland station which was underestimated by more than 30% [Hesshaimer *et al.*, 1989].

1.5.1.2 SF_6

Figure 6 shows the comparison of the long-term increase of SF_6 observations at Neumayer, Cape Grim, Izaña and Alert with model estimates. As already indicated in Figures 4a and 4b, the agreement between observed and modeled SF_6 concentrations is very good. Again for the pure trend curve this is not surprising as we used the quadratic trend of Neumayer, Cape Grim and Izaña data to estimate the time trend of the global SF_6 source strength. However, the perfect representation of the interhemispheric gradient confirms both, that the meridional transport in the model is adequately parameterized and that the latitudinal partitioning of our SF_6 production scenario is reasonable. Also confirmed now on an interannual time scale is the representativeness of Izaña for the mean concentration at that latitude, as we already pointed out above when discussing the SF_6 meridional profile for 1993.

1.5.2 Seasonal cycles

In both estimates of global trace gas emissions (^{85}Kr and SF_6) no seasonal variation had been taken into account. For SF_6 this assumption is justified as release of SF_6 in high voltage electrical equipment is unlikely to show any seasonality. For ^{85}Kr emissions, seasonal variations have been reported for the La Hague reprocessing plant showing nearly zero releases in the summer months July and August [Rath, 1988; Zimmermann *et al.*, 1989]. As this source alone contributes about 15-20% to the global source (see Table 1) part of the observed seasonal variation at regional stations in western Europe may also be attributed to the seasonality of this source (see below).

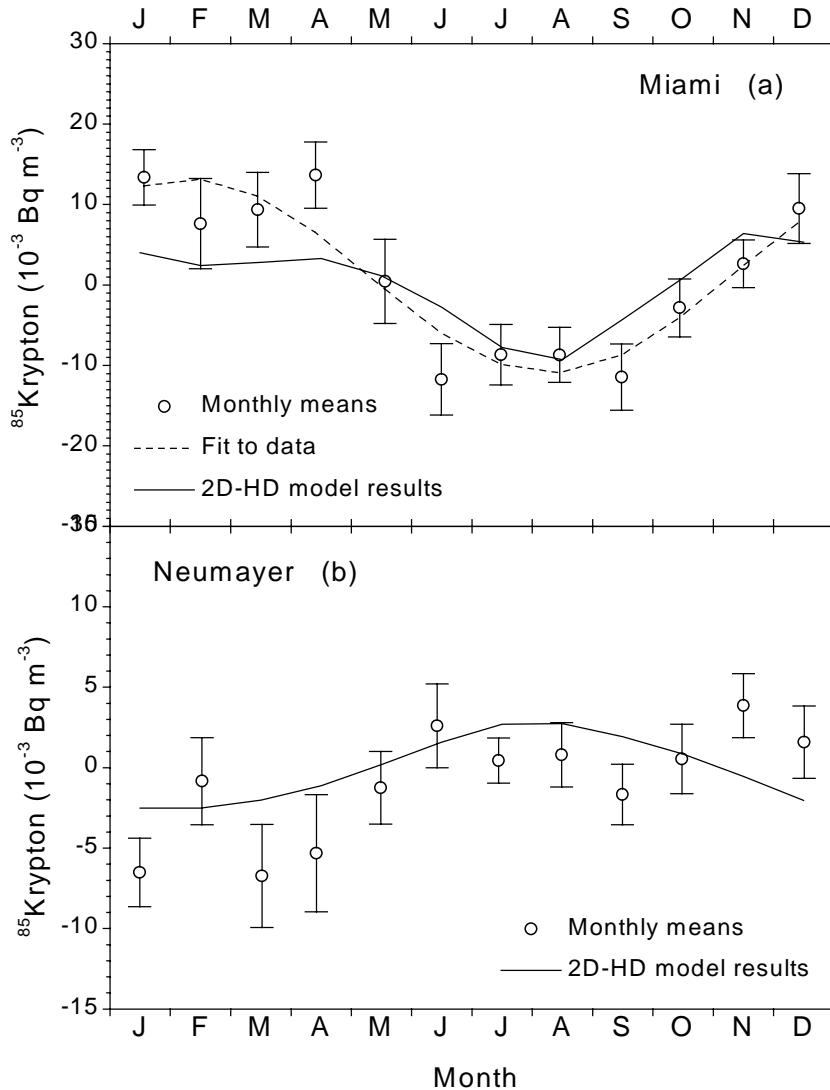


Figure 7 (a) 1981 - 1988 mean seasonal amplitude of selected monthly mean ^{85}Kr observations at Miami in comparison to the model estimate. (b) Same as (a) but for unselected observations at Neumayer from 1983 to 1988. Error bars show the standard deviations of the mean, calculated from eight (Miami) respectively five (Neumayer) individual years.

1.5.2.1 Krypton 85

Although no seasonal variation in emissions has been assumed, a pronounced seasonal variation of ^{85}Kr at Miami is estimated by the model with lowest values during summer and highest concentrations in winter and spring. Figure 7a shows the deviations of observed respectively modeled monthly mean ^{85}Kr values from the respective long term trends (modeled results and selected data of Figure 5a). As our model is restricted to two dimensions, only the seasonal changes in vertical and meridional transport are potentially reproduced. The striking agreement between model results and observations at Miami strongly suggests that the observed seasonal cycle of ^{85}Kr is caused by seasonal changes of the transport pattern: Both, the position of the Inner Tropical Convergence Zone (ITCZ) characterized by the steep concentration gradient between 30°N and 10°S (e.g. Figure 2), and/or the height of the boundary layer change with season. During winter, when the ITCZ is at its most southern location, Miami is largely influenced by the northern hemispheric regime (high ^{85}Kr concentrations), whereas during the

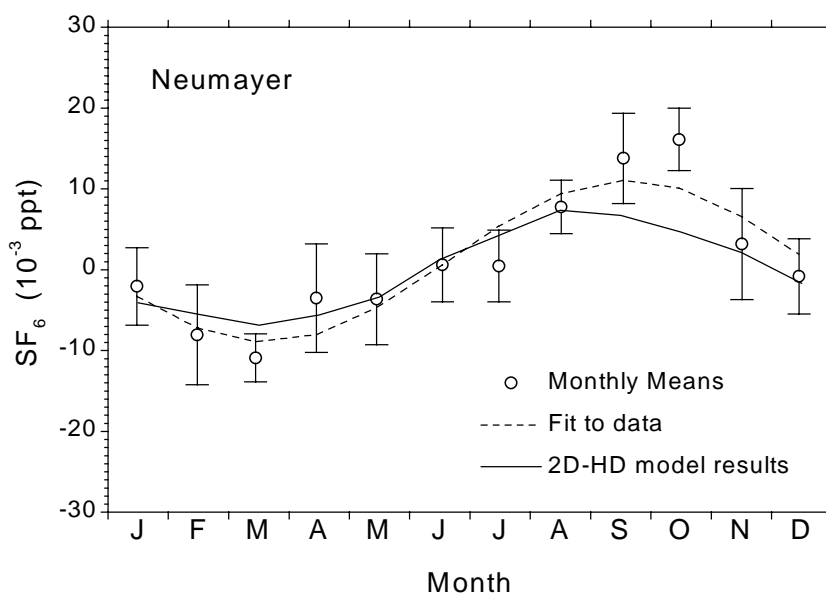


Figure 8 Mean seasonal amplitude of monthly mean SF_6 concentrations at Neumayer station from 1988 to 1993 in comparison to model estimates. The period from February 1991 to February 1992 has been excluded in the analysis due to possible contamination of the samples [Maiss *et al.*, 1996]. Error bars show the standard deviations of the mean calculated from five individual years.

summer, tropical air masses with lower ^{85}Kr activities are dominating at Miami. The seasonal amplitude we model for Miami underestimates the observations by about 30% which may be an indication that part of the variability is also caused by variations of the ^{85}Kr source. Within the year to year variability of the data, agreement between model and observations is, however, very satisfactory.

Also at Neumayer station in Antarctica a small seasonal ^{85}Kr cycle is calculated by the model (Figure 7b). This predicted seasonality is also slightly indicated in the data, however the November and December observations do not agree with the model estimates. The small seasonal amplitude postulated by the model for southern hemispheric stations may be attributed to variations in the interhemispheric transport being largest during the southern summer (December to February, compare Figure 9) when the ITCZ is moved northward therewith injecting high-concentration northern hemispheric air into the southern hemisphere. Also Prather *et al.* [1987] found a slight seasonality for CFC-11 concentration at Cape Grim which is in qualitative agreement with our model calculations.

1.5.2.2 SF_6

A significant seasonal variation is observed in SF_6 at Neumayer station which is in phase but about 30% larger than predicted by the model (Figure 8). Besides the effect of a changing flux of northern hemispheric air to the southern hemisphere (see below and Figure 9), input of SF_6 -depleted stratospheric air into the Antarctic troposphere is largest during late austral summer. This can be deduced from the seasonality of radioisotope ratios ($^{10}\text{Be} / ^7\text{Be}$) showing a maximum at Neumayer station at that time of the year (February) [Wagenbach, 1996]. The underestimated amplitude may be explained by a wrong parameterization of the seasonality of vertical exchange through both, the Global Weather Experiment wind fields, and the CONVEC transport scheme used in the Hamburg TM2 model and adopted for our 2D-HD model, particularly in high

southern latitudes. The nicely resolved seasonal cycle of SF₆ observed at Neumayer station now provides a powerful instrument to improve the transport parameters used in atmospheric models, particularly for these latitudes. This was not possible with the available ⁸⁵Kr data set [Weiss *et al.*, 1992] due to a significantly larger scatter in the observations at, e.g., Neumayer station. The relative scatter of the ⁸⁵Kr data is about a factor of two larger if compared to the respective SF₆ scatter at that site. Part of the reason for the larger ⁸⁵Kr variability also at Neumayer, Antarctica, seems to be a yet unidentified ⁸⁵Kr source in the southern hemisphere leading to significant positive ⁸⁵Kr excursions at the Cape Point station in South Africa [Weiss *et al.*, 1992]. Correct modeling of the transport is particularly crucial, e.g., to investigate the composite sources of CO₂ in middle to high latitudes of the southern hemisphere. Particularly concerning this aspect, SF₆ seems to be the most appropriate tracer to fulfill the task validating atmospheric transport models.

1.6 Interhemispheric exchange

The interhemispheric exchange time τ_{ex} is an important parameter to characterize global atmospheric transport models. It was introduced to express the strength of the ITCZ acting as the major resistance of air mass exchange between the two hemispheres [see e.g. Bolin and Rodhe, 1973]. Basically, it describes the inverse of the air mass fraction of one hemisphere transferred into the other hemisphere within the course of one year. Unfortunately, the value of τ_{ex} cannot be obtained from direct observations of air mass transport but has to be deduced indirectly from tracer observations. For tracers like ⁸⁵Kr or SF₆, mainly released to the atmosphere in the northern hemisphere and with atmospheric life times τ_a much longer than τ_{ex} , the transport to the southern hemisphere is mainly controlled by the concentration offset between the two hemispheres. Therefore, the hemispheric exchange time can be deduced from this offset provided the tracer release rate in both hemispheres is known.

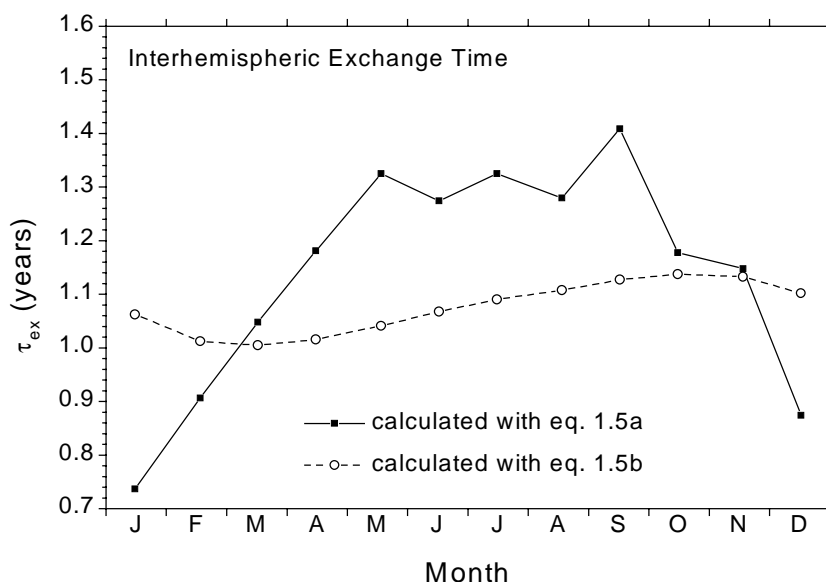


Figure 9 Seasonal cycle of the interhemispheric exchange time calculated for 1987 using ⁸⁵Kr as tracer. Results obtained with SF₆ as tracer are very similar. The solid line shows τ_{ex} calculated with equation (7), the dashed line shows τ_{ex} calculated according to Jacob *et al.* [1987] when assuming $d/dt(c_{NH} - c_{SH}) = 0$ (equation (8)).

1.6.1 Interhemispheric exchange time deduced from observations using a two-box model of the atmosphere

Subdivision of the atmosphere into two well-mixed boxes, each representing one hemisphere, and with a gross air mass flow between the two boxes inversely proportional to τ_{ex} allows a first approach to estimate this parameter. This procedure, with little modeling effort, has been used in the past leading to values of τ_{ex} between 1 and 2 years from ^{85}Kr and SF_6 observations [e.g. *Weiss et al.*, 1983; *Jacob et al.*, 1987; *Maiss et al.*, 1996]. Comparing the results of their three-dimensional atmospheric transport model with ^{85}Kr observations over the Atlantic ocean, *Jacob et al.* [1987] pointed out that the direct use of ground level ^{85}Kr observations to determine the interhemispheric concentration difference leads to τ_{ex} values systematically overestimated by about 50%. This is due to inappropriately neglecting the ^{85}Kr concentration decrease towards higher altitudes and in the stratosphere, particularly in the northern hemisphere.

For our two-box model approach, we use the simple tracer mass balance equations describing the variation of concentration in the two hemispheric boxes:

$$\frac{d}{dt}c_{NH} = 2\frac{Q_{NH}}{\alpha} - \frac{c_{NH} - c_{SH}}{\tau_{ex}} - \frac{c_{NH}}{\tau_a} \quad (2)$$

$$\frac{d}{dt}c_{SH} = 2\frac{Q_{SH}}{\alpha} + \frac{c_{NH} - c_{SH}}{\tau_{ex}} - \frac{c_{SH}}{\tau_a} \quad (3)$$

τ_a is the tracer's atmospheric life time; for ^{85}Kr , $\tau_a = 15.6$ years is the radioactive life time, for SF_6 we set $1/\tau_a = 0$ (no destruction). α is the conversion factor from tracer concentration c to the corresponding global atmospheric tracer mass inventory. If ^{85}Kr is expressed in Bq m^{-3} STP (1 $\text{Bq} = 27$ pCi) and Q in kCi (as in Table 1), $\alpha = 1.058 * 10^5$. For SF_6 expressed in ppt (10^{-9} moles of SF_6 per moles of air) and Q in kg, $\alpha = 2.55 * 10^4$. From (2) and (3) we have two choices to estimate τ_{ex} from mean hemispheric concentration time series:

$$\tau_{ex1} = \frac{c_{NH} - c_{SH}}{2\frac{Q_{NH}}{\alpha} - \frac{d}{dt}c_{NH} - \frac{c_{NH}}{\tau_a}} \quad (4)$$

$$\tau_{ex2} = \frac{c_{NH} - c_{SH}}{\frac{d}{dt}c_{SH} + \frac{c_{SH}}{\tau_a} - 2\frac{Q_{SH}}{\alpha}} \quad (5)$$

To estimate the mean hemispheric concentration time series, observations at individual sites are used. Differences in the interannual concentration changes (dc/dt) at different (back-ground) sites within one hemisphere are small for both tracers, ^{85}Kr and SF_6 , due to relatively fast mixing within hemispheres. The main uncertainty in the determination of τ_{ex} , therefore, is associated to the accuracy of the concentration difference between hemispheres ($c_{NH} - c_{SH}$).

We calculated mean hemispheric ^{85}Kr (surface) concentrations, from observed meridional profiles measured at ground level over the Atlantic Ocean (see Figure 2) using an appropriate areal weighting. All measured cruise data from *Weiss et al.* [1992] were normalized to October 1st, 1983. From the observed meridional profiles we obtain a mean $\tau_{ex} = 1.6$ years with the two-box model approach. When applying the same areal weighting procedure to the 2D-HD model

results corresponding to the cruise observations (also normalized to October 1st, 1983, see Figure 2) we obtain a $\tau_{ex} = 1.7$ years with the two-box model approach. This value is slightly, but not significantly higher than the τ_{ex} obtained directly from ⁸⁵Kr observations.

For the areal weighted meridional SF₆ profile observed at ground level over the Atlantic Ocean in November 1993 and extended northwards by station data from Fraserdale (back-extrapolated) and Alert (see Figure 4a and *Maiss et al.* [1996]), we obtain a value of $\tau_{ex} = 1.5$ years with the two-box model approach. The respective 2D-HD model results for the surface box layer, areal weighted and applied to the two-box model lead to the same $\tau_{ex} = 1.5$ years. These results have still to be confirmed by more observations. However, the very good agreement between the interhemispheric exchange time derived from direct SF₆ surface measurements over the Atlantic Ocean respectively from 2D-HD model results for the surface box layer confirms that Atlantic SF₆ profiles are probably a good approximation for the real zonal means. This is less obvious for the tracer ⁸⁵Kr where the Atlantic observations seem to underestimate the real zonal mean at least north of 40°N (see Figure 2).

All results for the interhemispheric exchange time derived with the two-box model approach from mean hemispheric surface values of ⁸⁵Kr and SF₆ (observations and 2D-HD model results for the surface box layer) lie in the range of 1.5 to 1.7 years. Also for the 2D-HD model estimated yearly mean surface ⁸⁵Kr profile in 1983-1984 we obtain a $\tau_{ex} = 1.5$ years. We, therefore, can confirm earlier estimates of the interhemispheric exchange time from *Weiss et al.* [1983], *Jacob et al.* [1987] and *Maiss et al.* [1996] when using surface data and a two-box model of the atmosphere.

1.6.2 Interhemispheric exchange time deduced from the 2D-HD model of the atmosphere

In the 2D-HD model the net cross-equatorial tracer flux F_{eq} can be computed on a monthly basis. The interhemispheric exchange time can then be calculated from the northern hemispheric concentration offset relative to the southern hemisphere:

$$\tau_{ex} = \frac{\alpha}{2} \frac{c_{NH} - c_{SH}}{F_{eq}} \quad (6)$$

Using equation (6) and ⁸⁵Kr respectively SF₆ as tracers, in both cases we obtain the same annual mean $\tau_{ex} = 1.1$ years. This interhemispheric exchange time is significantly smaller than the values we obtained from the two-box model approach and mean surface data ($\tau_{ex} = 1.5$ to 1.7 years) but agrees with the mean value reported by *Jacob et al.* [1987] ($\tau_{ex} = 1.1$ years) obtained with their three-dimensional atmospheric transport model. As pointed out earlier by *Jacob et al.* [1987], the discrepancy between the two model approaches is mainly due to an overestimation of the real hemispheric means by surface observations. More rapid interhemispheric exchange in higher tropospheric and stratospheric levels of the atmosphere is only of minor importance. In fact, for anthropogenic trace gases with predominant sources in the northern hemisphere, it is the ground level concentration pile-up in the northern hemisphere which is mainly responsible for overestimating $(c_{NH} - c_{SH})$. When using tropospheric means of SF₆ to calculate $(c_{NH} - c_{SH})$ and τ_{ex} , the interhemispheric exchange time is overestimated by only 10% if compared to values obtained with two-dimensional or three-dimensional models (compare Figure 4b where mean surface, tropospheric and hemispheric values for SF₆ in 1993 are shown as horizontal lines).

1.6.3 Seasonal variation of the interhemispheric exchange time

The seasonal variation of net tracer transport over the ITCZ is one major reason for seasonal ^{85}Kr and SF_6 concentration variations observed at ground level at least in the southern hemisphere. F_{eq} determined by the transport field used in the 2D-HD model varies with season, the same is true for the northern hemispheric concentration offset with respect to the southern hemisphere ($c_{\text{NH}} - c_{\text{SH}}$). Both parameters lead to a seasonal variation of τ_{ex} in our 2D-HD model with an amplitude of $\pm 30\%$. Weaker exchange is observed during the months April to September whereas interhemispheric exchange is enhanced in the northern winter months (Figure 9). The seasonal amplitude of τ_{ex} seems to be stronger by a factor of four and phase shifted by three months if compared to the figures reported by *Jacob et al.* [1987] for their 3D transport model. This obvious discrepancy seems to be caused by an artefact: *Jacob et al.* [1987] calculated the seasonal variation of τ_{ex} from the seasonal change of the global mean interhemispheric concentration difference using a linear relationship between τ_{ex} and ($c_{\text{NH}} - c_{\text{SH}}$) (dashed curve in Figure 9). This linear relationship is obtained from combining equations (2) and (3)

$$\tau_{\text{ex}} = \left(\frac{Q_{\text{NH}} - Q_{\text{SH}}}{\alpha(c_{\text{NH}} - c_{\text{SH}})} - \frac{\frac{d}{dt}(c_{\text{NH}} - c_{\text{SH}})}{2(c_{\text{NH}} - c_{\text{SH}})} - \frac{1}{2\tau_a} \right)^{-1} \quad (7)$$

and assuming $d/dt(c_{\text{NH}} - c_{\text{SH}}) = 0$. When also omitting the decay term ($1/(2\tau_a) = 0$), we obtain the simplified equation (8) which was used by *Jacob et al.* [1987, Figure 9]:

$$\tau_{\text{ex}} = \alpha \frac{c_{\text{NH}} - c_{\text{SH}}}{Q_{\text{NH}} - Q_{\text{SH}}} \quad (8)$$

However, assuming $d/dt(c_{\text{NH}} - c_{\text{SH}}) = 0$ is not justified at all when studying the influence of the seasonal behavior of ($c_{\text{NH}} - c_{\text{SH}}$) on the seasonality of τ_{ex} . The appropriate equation to calculate the seasonal change of τ_{ex} is (7). We, therefore, conclude that τ_{ex} indeed (also in the three-dimensional atmospheric model of *Jacob et al.* [1987]) is changing by a factor of two within the course of the year as illustrated in Figure 9. It is worth noticing that the seasonal cycle of SF_6 at Neumayer (Figure 8) can not be explained simply from the variation of interhemispheric tracer transport. Considering the southern hemispheric troposphere as a well mixed box we would deduce from τ_{ex} in Figure 9 a maximum tracer concentration in the southern hemisphere during February - March, when the interhemispheric tracer transport (inversely proportional to τ_{ex}) passes its yearly mean value. Figure 8 shows that the seasonal cycle of SF_6 observed at Neumayer is just opposite to this prediction. It is well possible that the arrival of northern hemispheric air at the Antarctic coast in 71°S is delayed by several months. On the other hand, input of stratospheric air into the Antarctic troposphere is nearly immediately observed at ground level. As stated above, SF_6 at Neumayer shows concentration minima in late southern hemispheric summer, the time of the year when we observe maxima of stratospheric air at Neumayer station [*Wagenbach, 1996*].

1.7 Summary and conclusions

Our high precision data base of the global distribution of SF_6 in the troposphere [*Maiss et al.*, 1996] was used in a two-dimensional atmospheric transport model (2D-HD model) to study the behavior of this new tracer in comparison to the classical global atmospheric transport tracer

⁸⁵Kr. The 2D-HD model grid has been derived from the 3D Hamburg TM2 model with the same resolution in the vertical and meridional direction, and was designed to run on any standard personal computer. The same vertical convection scheme and wind fields as in the TM2 model, reduced to two dimensions, were used in the calculations. In addition, the horizontal diffusion parameter of the model was adjusted by matching the model estimated mean meridional ⁸⁵Kr distribution with observations over the Atlantic Ocean. For simulating global tropospheric SF₆ concentrations, an almost linearly increasing SF₆ source strength was applied since 1970. The latitudinal distribution of the SF₆ source was assumed to be similar to the global electrical power production. The comparison of the 2D-HD model output with long-term observations of the two transport tracers ⁸⁵Kr and SF₆ has led to the following results:

1. The ⁸⁵Kr-tuned 2D-HD model led to excellent agreement with observations when estimating the meridional distribution of SF₆ at ground-based stations and over the Atlantic Ocean. Among others, this confirms our assumption that the SF₆ sources are distributed similarly to the global electrical power production.
2. The interhemispheric exchange time derived from mean ⁸⁵Kr and SF₆ observations at ground level when using a simple two-box model of the atmosphere ($\tau_{\text{ex}} = 1.5$ to 1.7 years) is considerably larger by about 50% if compared to the exchange time derived from a latitudinally resolved transport model (in our 2D-HD model $\tau_{\text{ex}} = 1.1$ years). This confirms the finding of *Jacob et al.* [1987] that hemispheric exchange times derived from two- and three-dimensional transport models cannot simply be applied to two-box models of the atmosphere if only surface observations are available. Using, however, tropospheric means leads to an overestimation of τ_{ex} of only 10% which is in the uncertainty range of estimates from high resolution transport models.
3. The interhemispheric exchange time τ_{ex} shows strong seasonal variations with about two times higher values in the northern hemispheric summer (May - September) than in the northern hemispheric winter (December - February). Interhemispheric exchange times derived from single meridional profiles can, therefore, be strongly biased.
4. The new high precision SF₆ data base with extremely smooth time trends now opens new possibilities for transport model validation. This is obviously true for models simulating man-made trace emissions with similar distributions as SF₆ which could be seen from the perfect agreement between model estimates and observations particularly in the northern hemisphere. SF₆ therewith proofed to provide the most powerful and easy to measure transport tracer for future atmospheric applications.

CHAPTER 2 Global bomb radiocarbon inventory

2.1 Introduction

As discussed in the introducing section to my thesis the attempts to match $\Delta^{14}\text{C}$ concentrations (see Appendix A.4.2 for the definition of the $\Delta^{14}\text{C}$ notation) observed in atmospheric CO_2 using the 2D-HD model confined by SF_6 failed. Our bomb ^{14}C modeling strategy initially was to start the simulations ongoing from ^{14}C activities observed since 1970 [Levin, 1985 #50; Manning, 1990 #51; unpublished results from the Heidelberg Radiocarbon Laboratory], several years after the major bomb ^{14}C injections into the atmosphere. Doing this we wanted to elude the problem of a poorly known ^{14}C yield per Mt-TNT of nuclear detonations, being at that time the most uncertain parameter of the bomb ^{14}C budget. The radiocarbon exchange fluxes between the 2D-HD model and the ocean were determined from carbon fluxes used in a three-dimensional atmospheric model [Heimann, 1989 #93; more details in Appendix A.1] combined with observations of oceanic bomb ^{14}C inventories [Broecker *et al.*, 1985] and surface water $\Delta^{14}\text{C}$ [Stuiver *et al.*, 1981]. The radiocarbon exchange fluxes to the biosphere were also determined from exchange fluxes used in the three-dimensional model [Heimann, 1989 #93; more details in Appendix A.2]. Unfortunately no observation-based ^{14}C inventory is available for the biosphere. We had to rely on weakly constrained model assumptions to determine the ^{14}C activity of CO_2 from soil carbon decomposition which balances the carbon assimilation by photosynthesis. This, however, made our ^{14}C exchange fluxes between the biosphere and the atmosphere rather hypothetical. The following sections show how we partly found out of this impasse by consistently budgeting the long-term bomb $^{14}\text{CO}_2$ observations in the troposphere and the stratosphere.

2.2 The model tools

Radiocarbon produced naturally in the upper atmosphere or artificially during the atmospheric weapon tests is the main tracer used to validate models of oceanic carbon cycling, in particular the exchange of carbon dioxide with the atmosphere [Stuiver, 1980; Stuiver *et al.*, 1981; Broecker *et al.*, 1985] and the mixing parameters within the ocean itself [Oeschger *et al.*, 1975; Siegenthaler, 1983; Toggweiler *et al.*, 1989; Maier-Reimer, 1993]. The atmospheric $^{14}\text{CO}_2$ activity has undergone large excursions since the beginning of nuclear bomb tests (solid lines Figure 10a and b). After the Test Ban Treaty in 1962 the bomb signal is declining in the atmosphere due to $^{14}\text{CO}_2$ exchange with the ocean and the other carbon reservoirs. The time behavior of these ^{14}C exchange fluxes mainly depends on the total carbon fluxes between the reservoirs, and on the internal circulation dynamics within these reservoirs.

The temporal variation of the tropospheric radiocarbon inventory N_{trop} is determined by the net exchange fluxes with the ocean F_o , the terrestrial biosphere F_b , and the stratosphere F_s , by input from anthropogenic sources Q_{trop} , and the radioactive decay ($\lambda^{-1} = 8275$ yrs) as follows:

$$\frac{d}{dt} N_{trop} = F_o + F_b + F_s + Q_{trop} - \lambda \cdot N_{trop} \quad (9)$$

Only the global response on the interannual time scale to a major atmospheric perturbation is

examined in this study. We, therefore, can use relatively simple models to determine the respective radiocarbon fluxes.

2.2.1 Model of the ocean, the biosphere and the stratosphere

For the ocean, a robust Oeschger and Siegenthaler type box diffusion model [Oeschger *et al.*, 1975; Siegenthaler, 1983] was adopted using a vertical eddy diffusion coefficient $K=7685 \text{ m}^2\text{yr}^{-1}$ coupled to 7.8 yr residence time of atmospheric CO_2 with respect to air/sea gas exchange. The flux F_o , computed according to our tropospheric boundary conditions, matches the integrated oceanic bomb ^{14}C uptake until 1.1.1974 of $300 \cdot 10^{26}$ atoms (Figure 11a) derived from oceanic measurements during GEOSECS [Broecker *et al.*, 1985], and compares well with results of the most recent version of the HILDA ocean model [Siegenthaler and Joos, 1992].

The model biosphere is divided into three boxes where the input carbon is decomposed exponentially with an e-folding constant given by the turnover time τ . Box 1 has a mass of 105 GtC (gigatonnes carbon; $1 \text{ Gt} = 10^{12} \text{ kg}$), $\tau = 3 \text{ yr}$, and accounts for fine roots, twigs and leaves. Box 2 has a mass of 675 GtC, $\tau = 27 \text{ yrs}$, and represents big roots, stems and branches. Box 1 and 2 couple directly to the troposphere, and the sum of their input fluxes, determining the net primary productivity, is set to 60 GtC yr^{-1} . Box 3, the "old carbon reservoir" has a mass of 1420 GtC and $\tau = 375 \text{ yrs}$. Box 3 contains the slowly decomposing material of boxes 1 and 2, gets its carbon input equally distributed from these boxes, and is needed to account for the low $\Delta^{14}\text{C}$ values measured in soil organic carbon [Harrison *et al.*, 1993]. These settings correspond to previously published estimates for the terrestrial biosphere [Siegenthaler and Oeschger, 1987]. We did not account for fertilization and destruction fluxes when computing F_b from the tropospheric boundary conditions.

Our model stratosphere consists of one box with the same CO_2 concentration as the model troposphere, and a turnover time of 2.5 yrs with respect to the troposphere. The total mass of the stratospheric box corresponds to 15% of the total atmospheric air mass. F_s was computed owing to the bomb input scenario and the measured tropospheric boundary conditions.

2.2.2 Initial and boundary conditions

The initial conditions in 1945 for all reservoirs were computed starting at preindustrial equilibrium in 1750 (280 ppm CO_2 , $\Delta^{14}\text{C}=-4.5\%$). Using annual means of observed atmospheric CO_2 concentrations [Keeling and Whorf, 1990] and $^{14}\text{CO}_2$ data [Levin *et al.*, 1985; Levin *et al.*, 1987; Manning *et al.*, 1990; Levin *et al.*, 1992] (Figure 12b) as prescribed input data in all scenarios, we automatically account for the dilution of $^{14}\text{CO}_2$ by input of ^{14}C free carbon from fossil fuel consumption (Suess effect [Suess, 1955]). All natural ^{14}C production ($P_{nat} = 2.3 \cdot 10^{26}$ atoms yr^{-1} , assumed as constant) occurred in the stratosphere.

The anthropogenic input of $^{14}\text{CO}_2$ by the nuclear industry, significantly contributing to the tropospheric inventory only from about 1970 onwards, was calculated for different reactor types using the normalized $^{14}\text{CO}_2$ emission data per generated electrical energy reported by Bonka [1980] and in UNSCEAR [1993]. The latter was estimated for the period of 1970-1990 from the installed plants worldwide, assuming a capacity utilization of 60% for all reactor types. $^{14}\text{CO}_2$ emissions from reprocessing plants were also taken from UNSCEAR [1993]. The $^{14}\text{CO}_2$ release from the nuclear industry in 1990 was estimated to be less than $0.5 \cdot 10^{26}$ ^{14}C atoms yr^{-1} , increasing almost linearly from 1970 onwards (cf Figure 11b).

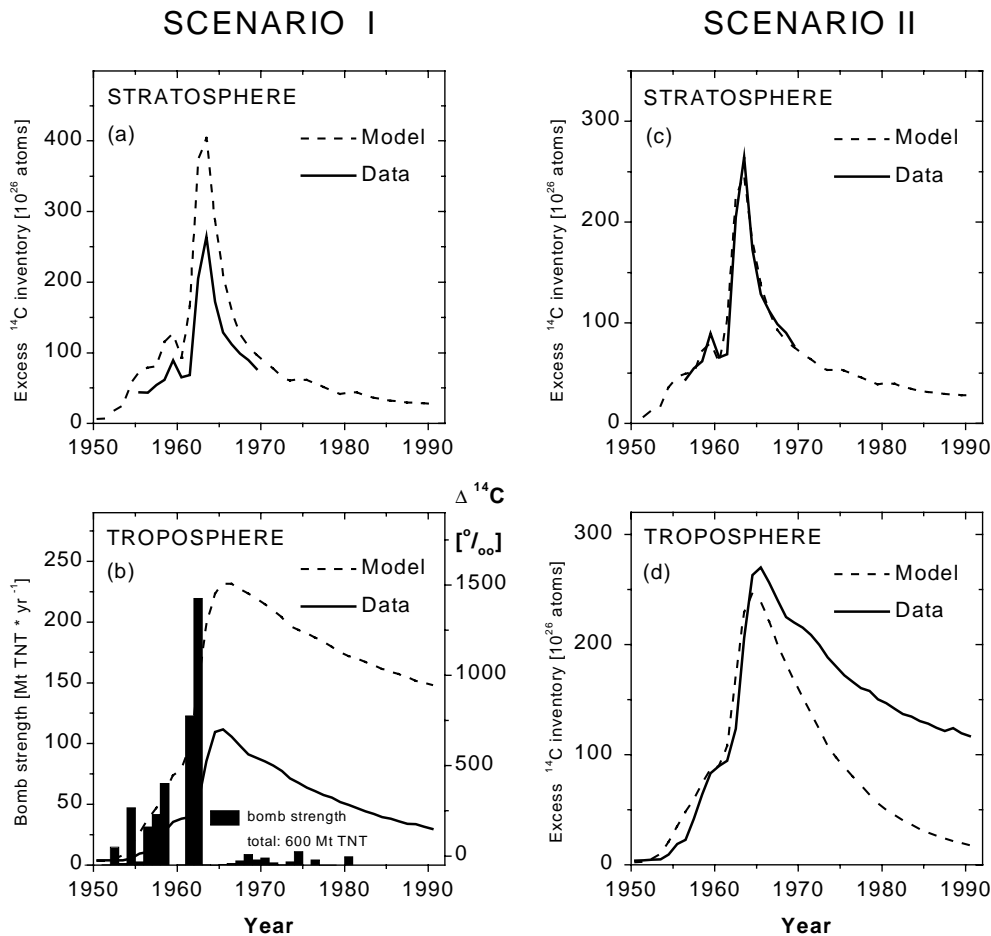


Figure 10 *a-d*, Comparison between results from two ^{14}C model scenarios (dashed lines) and annual means of observations (solid lines) in the stratosphere (*a* and *c*), and in the troposphere (*b* and *d*). The observed stratospheric inventories were taken from *Tans* [1981] and *Telegadas* [1971] (according to *Tans* [1981], the original observations are corrected by -20%; another adjustment of +3.5% was made to correct for the NBS oxalic acid standard activity value used by *Telegadas* [1971]). Mean tropospheric ^{14}C inventories are calculated from long-term tropospheric observations in both hemispheres [*Levin et al.*, 1985; *Levin et al.*, 1987; *Manning et al.*, 1990; *Levin et al.*, 1992]. For the early period of 1950-1959, we use tree ring ^{14}C data [*Stuiver and Quay*, 1981]. In both scenarios, the stratosphere consists of only one box with an air mass of 15% of the atmosphere, corresponding to a tropopause level at 13.5 km. In scenario I (*a* and *b*), the bomb ^{14}C input is estimated using the bomb strength data (*b*), and the standard ^{14}C yield P_{stand} of $1.75 \cdot 10^{26}$ atoms per Mt-TNT [*UNSCEAR*, 1982]. With P_{stand} the tropospheric and the stratospheric $^{14}\text{CO}_2$ levels are overestimated. In scenario II (*c* and *d*) the bomb ^{14}C input is adjusted to 60% of P_{stand} . The model matches the observations in the troposphere until about 1963. After that date the decrease in the troposphere is much faster than actually observed. The missing tropospheric $^{14}\text{CO}_2$ source needed to adjust model and data results is similar in time shape and strength to about 25% of the oceanic or, equivalently, to 80% of the biospheric net bomb ^{14}C uptake flux (see Figure 12*d* and *e*).

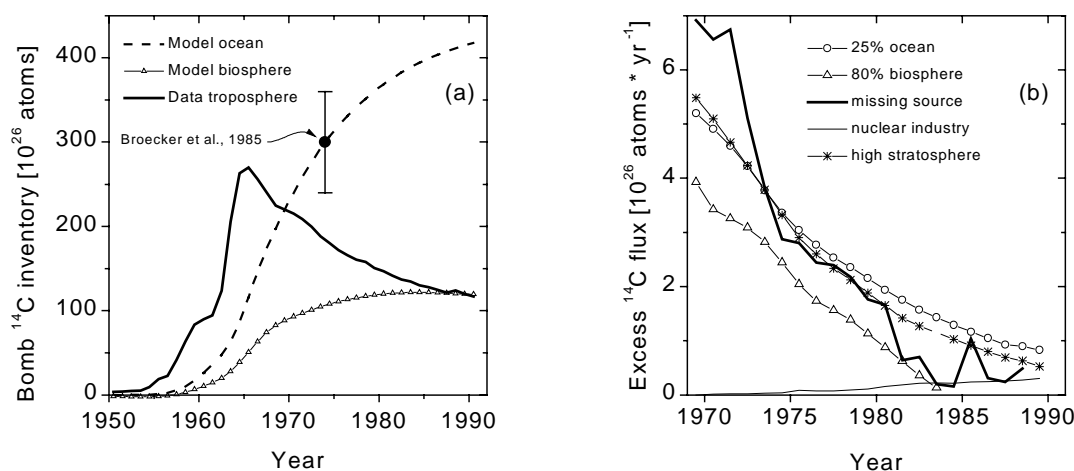


Figure 11 Bomb ^{14}C inventories (a) and missing source flux (b). a, The standard bomb ^{14}C inventories are calculated as the difference to the respective ^{14}C inventory in 1940. The standard inventories for the ocean (dashed line) and the biosphere (Δ) are as computed for scenarios I, II & III with prescribed tropospheric values. The standard ocean bomb ^{14}C inventory on 1.1.1974 matches the value of $300 \cdot 10^{26}$ atoms (\bullet) given by Broecker et al. [1985]. b, The missing ^{14}C flux to the troposphere (6 years running means, thick solid line) is as calculated in scenario II (Figure 10d). This missing flux is compared to the net supplementary contributions from (1) a high stratosphere (*, scenario III), (2) a 80% reduction of the standard biospheric uptake (Δ , scenario IV), and (3) a 25% reduction of the standard oceanic uptake (\circ , scenario V). In all three cases, the supplementary flux has the right time shape and amplitude to account for the missing source (Figure 12b, d and e). The emission from nuclear installations (thin solid line) is also given for comparison.

2.3 Bomb ^{14}C yield and ^{14}C budget imbalance

2.3.1 Bomb ^{14}C emissions

^{14}C input from the atmospheric bomb tests was estimated based on the compilation of bomb strength data [Rath, 1988] (Figure 10b), and, depending on the respective scenario, adjusting the specific ^{14}C production per megatonne (Mt) TNT to the tropospheric and stratospheric observations during the time period of the major ^{14}C rises. The uncertainty of this adjustment is small as the total bomb ^{14}C uptake by the ocean and the biosphere compared to the bomb input is small until 1963. As the observational data in the troposphere show a systematic delay between the date when the stronger bombs were fused, and the date when the respective signal showed up in the troposphere, we introduced all bomb ^{14}C production directly into the stratosphere. The results reported in Figure 10a and b show clearly that the ^{14}C production calculated with the standard ^{14}C yield $P_{stand} = 1.75 \cdot 10^{26}$ atoms per Mt-TNT [UNSCEAR, 1982] was overestimated. In fact, different estimates of P_{stand} are in the range $(1-2) \cdot 10^{26}$ atoms per Mt-TNT [Machta et al., 1963; Bonka, 1980].

2.3.2 Missing source or overestimated sink

Figure 10c and d (scenario II) show the results obtained when reducing the value of P_{stand} by 40%. The model inventory fits well with the data in the stratosphere and in the troposphere until 1963, as long as the bomb production is the dominant flux term. In the post bomb period, the model troposphere is influenced by a much too strong sink term. The fictive tropospheric source

needed to adjust model and data results reveals to be similar in time shape and strength to about 25% of the oceanic or, equivalently, to 80% of the biospheric net bomb ^{14}C uptake flux (Figure 11*b*). The magnitude of the missing source can be in error by at most one third. This is mainly due to the strong constraint on the coupling constants between the reservoirs given by the more than 40 years long record of tropospheric $^{14}\text{CO}_2$ observations. The strength of the missing source should decrease with an e-folding time similar to the ocean uptake, i.e. about 8 yr. Neither the nuclear industry nor the natural cosmic ray production can account for this source. The variation of cosmic ray production is about 20% between solar minimum and solar maximum [Stuiver and Quay, 1980], and, thus, at least one order of magnitude too small. The ^{14}C production by nuclear industry is only a few permil of the needed ^{14}C source in the 1970s, while increasing instead of declining (Figure 11*b*).

2.4 Possible solutions to the ^{14}C imbalance

2.4.1 Stratosphere

Looking for a candidate in the atmosphere itself, we subdivided the stratosphere in two boxes. The high box contains less than 1.5% of the atmospheric mass (lower boundary corresponding to 25 km a.s.l.) and has a turnover time of about 5 yr exchanging with a low box ($\tau = 2.5$ yr with respect to the troposphere). In Figure 12*a* and *b* the results obtained with such a two-box stratosphere (scenario III) are shown. In this scenario, 15% of the adjusted bomb production (in this case 70% of P_{stand}) are injected into the high stratosphere, the rest into the low stratosphere. Scenario III now leads to a nearly perfect agreement between the model and the observations in the lower stratosphere and in the troposphere. However, scenario III demands very high $\Delta^{14}\text{C}$ values in the remote high stratosphere (Figure 12*a*) which is inconsistent with recent $^{14}\text{CO}_2$ observations up to 30 km height [Nakamura *et al.*, 1992]. Also the old data from Telegadas [1971] obtained in the early 1960s suggest a $\Delta^{14}\text{C}$ decrease rather than an increase to higher stratospheric levels. Moreover, the observed decrease from intermediate to high stratospheric levels has also been obtained by recent high resolution stratospheric model calculations [Rasch *et al.*, 1994]. Therefore, the required remote stratosphere (with still very high $^{14}\text{CO}_2$ levels) can most probably not close the bomb ^{14}C budget.

2.4.2 Biosphere

On the other hand, assuming almost no bomb ^{14}C uptake by the terrestrial biosphere (scenario IV, Figure 12*c* and *d*) would also match the bomb radiocarbon constraints. In our model scenario this reduced uptake is simply obtained by multiplying the standard uptake of the biosphere with 0.2. In reality, such a strong reduction is only achieved if, for example, the net primary productivity is reduced by a factor of 5 and the reservoir sizes are modified accordingly. This, however, would so seriously contradict our understanding of mass, cycling and turnover times in the biosphere [Goudriaan, 1992] that scenario IV appears highly improbable.

2.4.3 Ocean

The most tempting solution to the problem would be an about 25% reduction of the ^{14}C uptake by the ocean (scenario V, Figure 12*c* and *e*) leading to an oceanic bomb ^{14}C inventory reduced by the same amount. This only means a correction to known processes (e.g. gas exchange rate) rather than introducing, for example, still unconsidered subreservoirs as in the biospheric or stratospheric scenarios. However, a 25% reduction of the bomb ^{14}C inventory of the ocean lies outside the error bars generally accepted for this number (20%, [Broecker *et al.*, 1985]). The contradiction gets even larger when taking into account the very recent upward revision of the

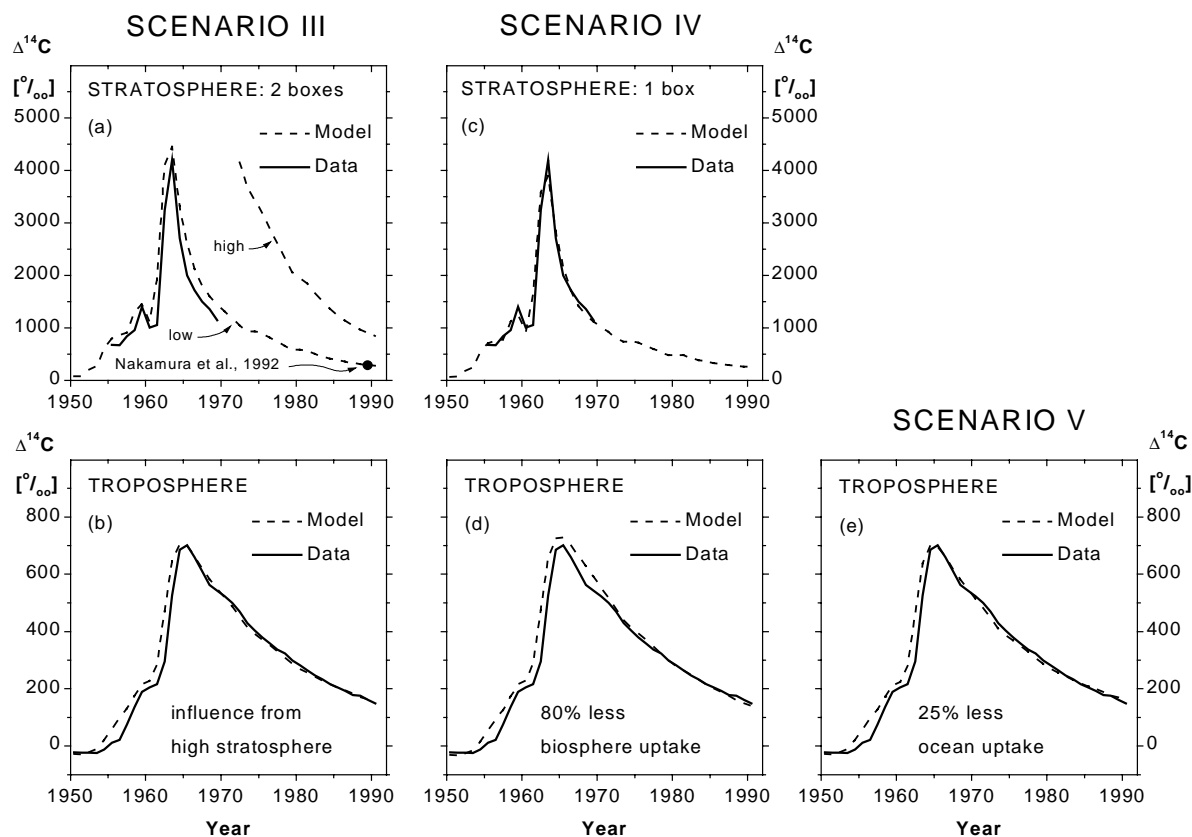


Figure 12 Comparison between observed and calculated $\Delta^{14}\text{C}$ values in the troposphere, (b, d, e) and in the two- and one-box stratosphere (a and c respectively). ^{14}C results of stratospheric sampling in 1989 [Nakamura et al., 1992] are included in a. In scenario III (a and b) bomb ^{14}C input is adjusted to 70% of P_{stand} . The stratosphere is subdivided into two boxes, 85% of the bomb ^{14}C input is introduced into the lower stratosphere, and 15% into the remote high stratosphere. The model results agree well with the atmospheric observations in the troposphere and in the lower stratosphere (90% of stratospheric air mass, 13.5 to 25 km height). The stratospheric observations, however, indicate that, even in the early 1990s, the modeled upper stratospheric $\Delta^{14}\text{C}$ is still about 2 times too high. In scenario IV (c and d) and V (e), as in scenario II (Figure 10c and d), bomb ^{14}C input is adjusted to 60% of P_{stand} and introduced into the one-box stratosphere. In scenario IV, the bomb ^{14}C uptake by the biosphere has been reduced by 80%, in scenario V, bomb ^{14}C uptake by the ocean has been reduced by 25% with respect to the standard case given in scenario II. Scenarios IV and V satisfactorily match the $^{14}\text{CO}_2$ observations, both in the troposphere as well as in the one-box stratosphere (the stratospheric model results of scenario V are indistinguishable from those of scenario IV). However, both scenarios are in serious disagreement to the actual understanding of the carbon cycle.

oceanic bomb ^{14}C inventory evaluated on the basis of more observations and an improved estimation of the pre-bomb natural oceanic radiocarbon distribution [Peng and Broecker, 1993]. This problem needs to be resolved.

2.5 Summary and conclusions

We have tested the overall consistency of $^{14}\text{CO}_2$ exchange fluxes between all relevant compartments in a simple model of the global carbon cycle, using long term tropospheric CO_2 [Keeling and Whorf, 1990] and $^{14}\text{CO}_2$ [Levin *et al.*, 1985; Levin *et al.*, 1987; Manning *et al.*, 1990; Levin *et al.*, 1992] observations, the bomb ^{14}C inventory in the stratosphere [Telegadas, 1971; Tans, 1981] and a compilation of bomb detonation dates and strengths [Rath, 1988]. We found that to balance the budget, we must invoke an extra source to account for e.g. 25% of the generally accepted uptake of bomb ^{14}C by the ocean [Broecker *et al.*, 1985]. The strength of this source decreases from 1970 onwards, with a characteristic time scale similar to that of the ocean uptake. Significant radiocarbon transport from the remote high stratosphere and drastically reduced uptake of bomb ^{14}C by the biosphere can both be ruled out by observational constraints. We therefore conclude that the global oceanic bomb ^{14}C inventory should be revised downwards. A reduced bomb ^{14}C uptake by the ocean models would have significant implications for our understanding of the global carbon cycle: (1) The radiocarbon-derived CO_2 gas exchange coefficient would have to be reduced by the same amount, then being almost in agreement with estimates of Liss and Merlivat [1986] which are based on direct measurements in wind tunnels, over lakes and open ocean [Watson, 1993]. (2) If we believe the ^{14}C observations in surface water performed during the last 30 years, the estimated bomb ^{14}C penetration depth [Broecker *et al.*, 1980] has to be reduced. (3) If it is assumed that the CO_2 uptake by the ocean scales directly with the bomb ^{14}C penetration depth [Siegenthaler and Sarmiento, 1993] a downward revision of the latter would imply a corresponding reduction by approximately 25% of the inferred oceanic sink for anthropogenic CO_2 .

CHAPTER 3 Tracing the cycle of air mass through the stratosphere with bomb ^{14}C

3.1 Introduction

The radiocarbon modeling investigations presented in Chapter 2 [Hesshaimer *et al.*, 1994] detected a serious mismatch within the carbon cycle. The detected global bomb ^{14}C imbalance was soon corroborated by an other study [Broecker and Peng, 1994] which preceded a revision of the ocean bomb ^{14}C inventory [Broecker *et al.*, 1995]. That revision, however, confirmed the previously published bomb ^{14}C inventory of the ocean ($300 \cdot 10^{26} \pm 20\%$ atoms on 1.1.1974) furthermore reducing its uncertainty from $\pm 20\%$ to $\pm 10\%$. In this latter study the authors concluded that " ... for times earlier than 1965, the stratospheric and perhaps tropospheric inventories are uncertain due to inhomogeneities in the distribution of bomb radiocarbon during the first year or two after the test ban was implemented". Also other authors neutralized the radiocarbon mismatch by depreciating the atmospheric, especially the stratospheric $^{14}\text{CO}_2$ observations [Lassey *et al.*, 1996; Jain *et al.*, 1997]. As this contradicts our fundamental modeling assumption relying on both the quality and the relevance of atmospheric $^{14}\text{CO}_2$ monitoring we decided to carefully assess the stratospheric observations. However, stratospheric-tropospheric air mass exchange (STE) happens on many scales ranging from large-scale Hadley Cell circulation to small-scale eddy transport across the tropopause [Holton *et al.*, 1995]. This makes it very difficult to get globally valid intensities of STE from observed or computed wind fields and even three-dimensional global atmospheric transport models fail to reproduce stratospheric tracer distributions in the troposphere [Rehfeld and Heimann, 1995]. As a realistic parameterization of STE is crucial to successfully implement ^{14}C in global carbon cycle models we designed for that purpose a new global carbon isotope model.

3.2 Model

Our model refines and extends our previous bomb ^{14}C study [Hesshaimer *et al.*, 1994] now resolving seasonal variations and including explicitly all carbon isotopomers of CO_2 in the atmosphere, the ocean and the biosphere.

3.2.1 Atmosphere

Figure 13 shows the simple model atmosphere structure adopted from Telegadas [Telegadas, 1971]. Each hemisphere is subdivided into two tropospheric and five stratospheric well-mixed compartments exchanging air mass only through mixing. Meridional air mass transport in the troposphere was determined to obtain good agreement between model results and globally distributed SF_6 observations as described in Chapter 2. The carbon cycle part of the model includes emissions from fossil fuel consumption, cement manufacturing and gas flaring [Keeling, 1994; Marland *et al.*, 1994] and emissions from land use change [Houghton and Hackler, 1995].

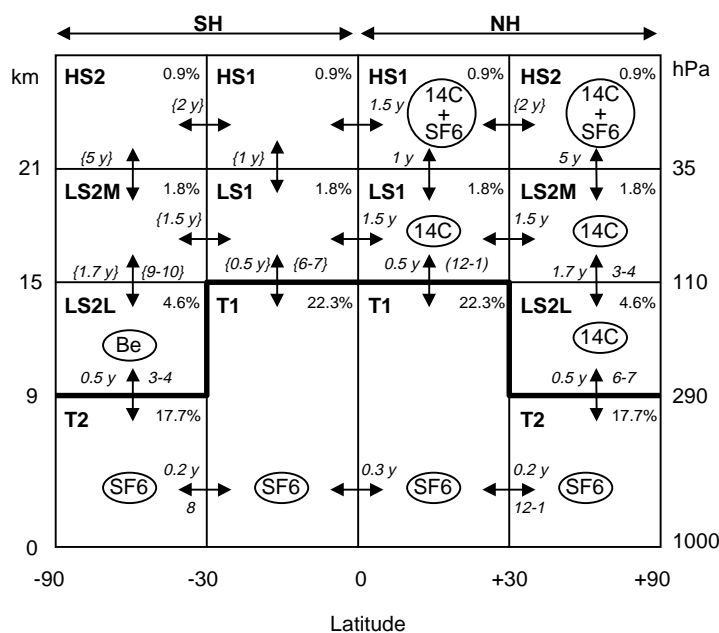


Figure 13 Schematic representation of the model atmosphere versus geographical latitude and elevation above ground. The considered air mass amounts 5.1×10^{18} kg distributed 20% to the stratosphere and 80% to the troposphere. In the northern hemisphere (NH), the poleward troposphere (NHT2), the poleward low stratosphere (NHLS2L), the poleward middle stratosphere (NHLS2M), the poleward high stratosphere (NHHS2), the equatorward troposphere (NHT1), the equatorward low stratosphere (NHLS1) and the equatorward high stratosphere (NHHS1) have their name in the upper left corner and their air mass fraction in the upper right corner of their box. In the southern hemisphere (SH), the definitions are correspondent. The arrows representing air mass exchange are supplemented on one of their ends by the exchange strength and by the months of maximum exchange. Each exchange strength describes the ratio of the air mass in the surrounding box and of the gross yearly air mass flux represented by its arrow. The exchange strength values have an individual uncertainty of about $\pm 30\%$. The uncertainty of peak exchange times is about ± 1.5 months. Values in parentheses are less certain. Southern hemispheric values in curly braces are mirrored from the northern hemisphere. Open ellipses contain the name of the tracer(s) which mainly constrains the surrounding exchange values.

3.2.2 Ocean and biosphere

The exchange of atmospheric CO_2 with the ocean and the biosphere is determined from two-dimensional monthly carbon flux distributions used in the atmospheric transport model TM2 [Heimann and Keeling, 1989]. The radiocarbon exchange with the ocean is calculated by combining these carbon fluxes with $\Delta^{14}\text{C}$ observations in the troposphere [Stuiver and Quay, 1981; Tans, 1981; Manning et al., 1990; Levin et al., 1992] and in the ocean surface [Broecker et al., 1995]. To account for the bomb ^{14}C imbalance [Broecker and Peng, 1994; Heshaimer et al., 1994] we use a low air-sea gas exchange rate with a global mean of $4.55 \times 10^{-2} \text{ mol m}^{-2} \text{ yr}^{-1} \mu\text{atm}^{-1}$. This results in an oceanic bomb ^{14}C inventory during January 1975 which is 25% lower than the Broecker inventory [Broecker et al., 1995]. At preindustrial equilibrium assumed for the year 1750 our model biosphere (see Appendix A.2 for details) has a total inventory of 2200 Gt-C (1 Gt-C = 10^{12} kg of carbon) and cycles radiocarbon along with the net primary productivity of 60 Gt-C yr^{-1} which, on a yearly basis is exactly balanced by litter and soil carbon decomposition to the atmosphere. These and other biospheric settings overall correspond to present day literature [Post III, 1993].

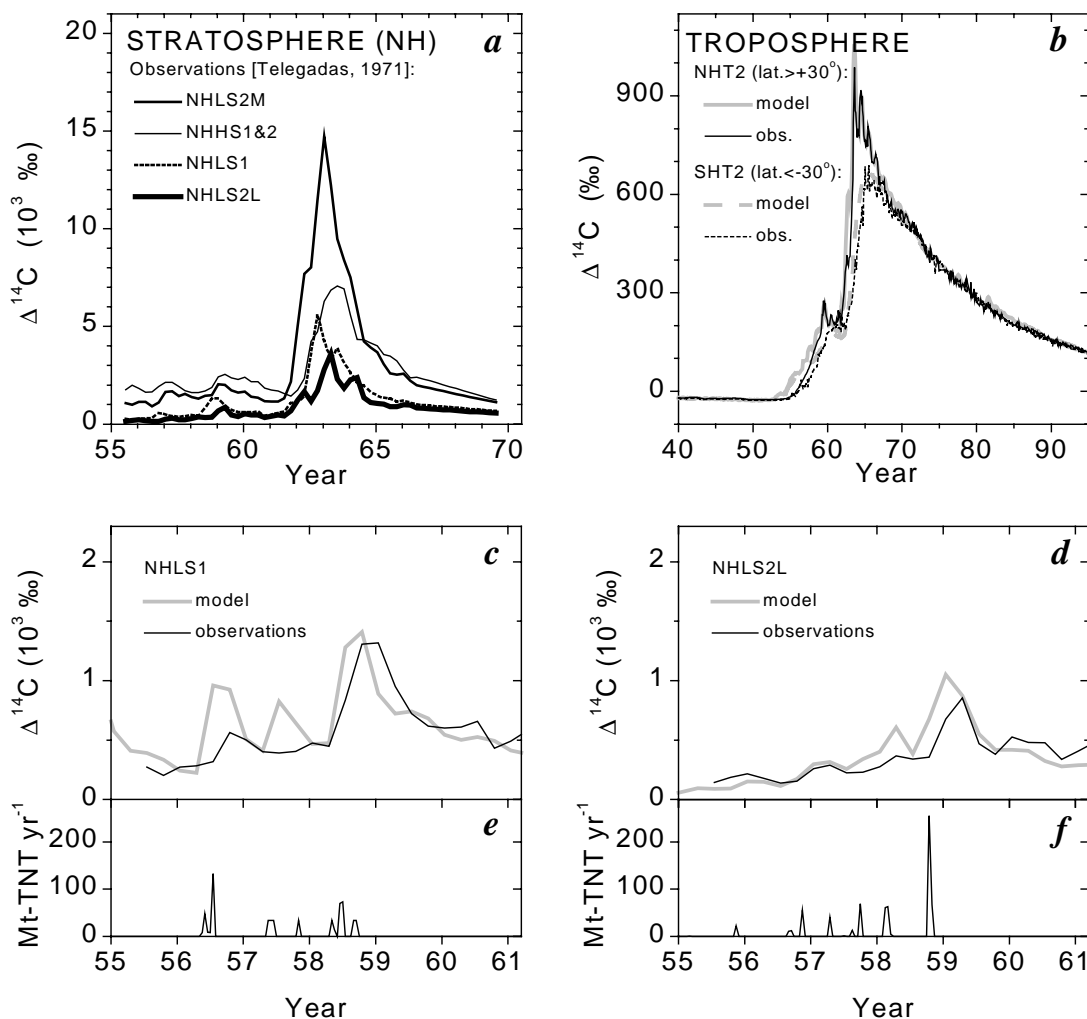


Figure 14 Observations of ^{14}C activity in the northern hemispheric stratosphere (*a*) and in the free troposphere (*b*) compared with model results for the troposphere (*b*) and for the lower northern hemispheric stratosphere (*c* and *d*). In *a*, NHHS1&2 is the stratospheric area including NHHS1 and NHHS2 from Figure 13 because *Telegadas* [1971] did not consider this subdivision of the high stratosphere. The observed stratospheric bomb ^{14}C activities [*Telegadas*, 1971] are corrected by -20% according to *Tans* [1981] and further adjusted by +3.5% to correct for the NBS oxalic acid standard activity value used by *Telegadas* [1971]. These activities were converted from atoms per gram of air to $\Delta^{14}\text{C}$ ($\Delta^{14}\text{C}$ is the per mil deviation from NBS oxalic acid activity corrected for decay [*Stuiver and Polach*, 1977]) using model values for the CO_2 concentration and the $\delta^{13}\text{C}$ isotopy. Direct bomb ^{14}C injections to the lowest stratospheric boxes (*e* and *f*) are compared with $\Delta^{14}\text{C}$ from observations and from the model in these boxes (*c* and *d*). The ^{14}C input corresponding to each blast was distributed over its vertical extension following a decreasing exponential with an e-folding height of 3 km. This accounts in some way for the effect of both pressure and nuclear cloud concentration decreasing with height. To obtain a vertical repartition of the bomb input agreeing with the stratospheric observations during the years of major injections 1961 and 1962 we finally had to multiply the lower boundary of the prescribed extensions by 0.8 in the poleward belts.

We use a natural cosmic ray ^{14}C production of $2.8 \cdot 10^{26}$ atoms ^{14}C yr^{-1} distributed 2/3 to the stratosphere and 1/3 to the troposphere according to *Lingenfelter* [1963]. Only 80% of this natural production are removed from our model atmosphere by oceanic and biospheric uptake and by radioactive decay (^{14}C decays with a mean lifetime of 8275 yr). The remaining 20% are

removed from the model troposphere to overall account for ^{14}C decay in sedimentary reservoirs like coastal wetlands and continental paleosols [Damon and Sternberg, 1989]. In addition to the main anthropogenic ^{14}C source from nuclear bomb tests which is more detailed below we also account for small ^{14}C emissions from nuclear industry as described in Chapter 2 [Hesshaimer *et al.*, 1994].

3.3 Data

The three observational data sets mainly corroborating our stratospheric air mass cycling are a compilation of stratospheric ^{14}C observations [Telegadas, 1971] (Figure 14a), long-term measurements of the tropospheric radiocarbon composition [Manning *et al.*, 1990; Levin *et al.*, 1992] (Figure 14b) and a collection of bomb strength data [Rath, 1988]. The bomb strength data include date, geographical location and vertical extension of atmospheric and underground nuclear detonations between 1945 and 1981. For bombs detonated near ground some of the neutrons are absorbed by the earth surface instead of producing ^{14}C by low-energy resonance capture reaction with atmospheric nitrogen [Enting, 1982]. We accounted for this by dividing all detonations strengths before 1959 by 1.5 so that the total *effective* strength for ^{14}C production amounts to 530 Mt-TNT_{eff} instead of 600 Mt-TNT for the entire data set. Applying the adjustment procedure described in Chapter 2 [Hesshaimer *et al.*, 1994] we now use a yield of $1.15 \cdot 10^{26}$ atoms per Mt-TNT_{eff} to calculate ^{14}C inputs. In total 89% of the bomb ^{14}C input are injected to the northern hemispheric stratosphere and 7% to the respective troposphere. The remaining 4% of bomb ^{14}C are injected to the southern hemisphere.

3.4 Results: air mass exchange intensity and phase

Combining our bomb input scenario with optimum cross-tropopause radiocarbon fluxes we satisfactorily model the $\Delta^{14}\text{CO}_2$ observations in the troposphere (Figure 14b) and in the lowest stratospheric boxes (NHLS2L, NHLS1) of the northern hemisphere (Figure 15a and b). By this we implicitly determine the residence time of air in NHLS2L and NHLS1 with respect to STE. We reiterated the same procedure with the overlaying stratospheric boxes NHLS2M, NHHS1 and NHHS2 (Figure 15c and d) to obtain the other air mass exchange strengths reported in Figure 13. Mixing times within the high stratospheric boxes NHHS1 and NHHS2 were further constrained to match observed vertical SF₆ profiles [Harnisch *et al.*, 1996]. The interhemispheric exchange strengths in the stratosphere were determined to match the bomb ^{14}C observations in the southern hemisphere.

The stratospheric ^{14}C excursions reported by Telegadas [1971] reflect the conjugate influence of direct bomb injections and dilution by air mass exchange. Figure 14c and d illustrates how the model tracks these alternating features before the major nuclear tests began. The strongest nuclear test series performed between September 1961 and November 1962 injected half of the total bomb ^{14}C production into the poleward stratosphere. Later blasts were much weaker so that subsequent stratospheric ^{14}C activity variations were mainly controlled by stratospheric air mass cycling and STE. The stratospheric $^{14}\text{CO}_2$ observations after 1963.0 track not only the strength but also the seasonality of air mass cycling. Although constrained by tropospheric observations only, the model STE seasonality with a peak of exchange in June-July well reproduces the stratospheric observations in the lowermost poleward stratosphere NHLS2L (Figure 15e). In the lower equatorward stratosphere (Figure 15f), the observed seasonality until 1964 is matched when STE exchange peaks during December-January. A subtle information becomes apparent

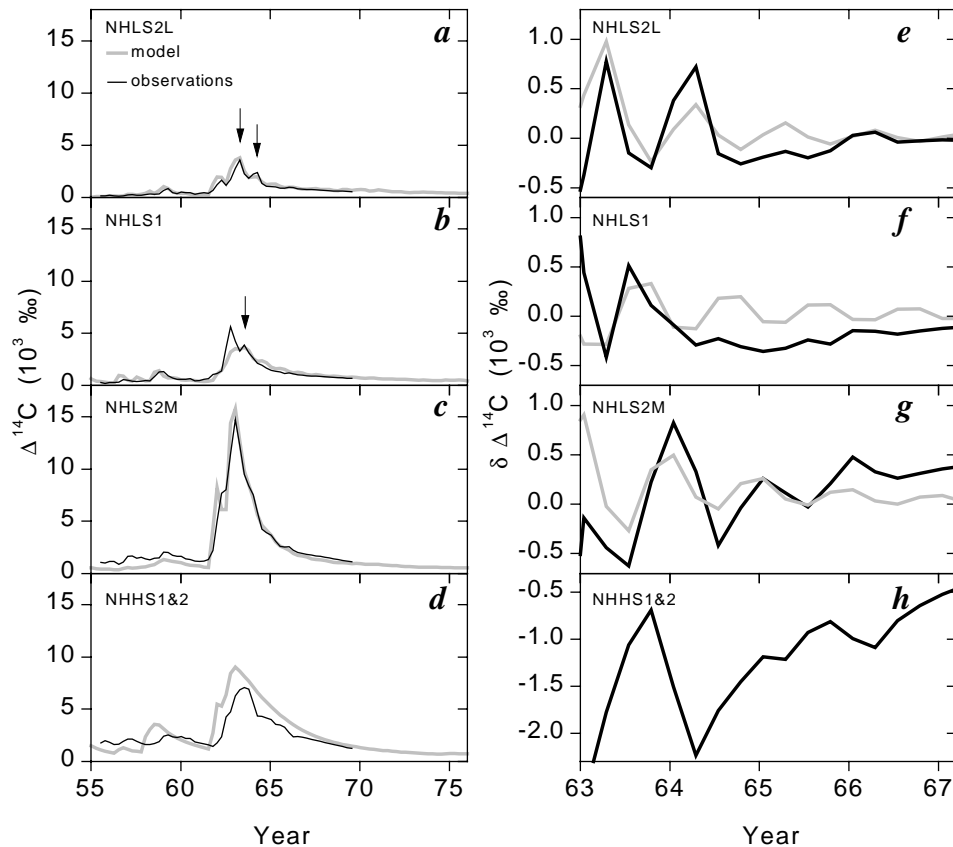


Figure 15 Comparison of stratospheric ^{14}C observations and model results. With the parameterization of Figure 13 the model matches the observations in all subdomains of the northern hemispheric stratosphere for which *Telegadas* [1971] has determined bomb ^{14}C inventories (*a-d*). Rising activities reflect time, location and strength of bomb inputs as long as direct ^{14}C injections from nuclear blasts prevail over delayed injections from adjacent stratospheric subdomains. Decreasing activities reflect the strength of air mass exchange (see also Figure 14*c-f*). Three arrows in *a* and *b* mark the most pronounced stratospheric ^{14}C peaks which do not result from direct bomb input and thus track the seasonality of air mass exchange. Seasonal components extracted from observations and from the model for the first 4 years after the maximum bomb ^{14}C activity in 1962 are shown in *e-h*. These seasonal components are obtained by subtracting a smoothed trend from both the model results and the observations. The smoothed trend results from a model run with all seasonal amplitudes of stratospheric air mass cycling and STE set to zero.

in Figure 15*g* where the exchange between the middle poleward stratosphere NHLS2M and the underlying box NHLS2L reveals to be maximal in early spring. A significant seasonality of the exchange between NHLS2M and both NHHS2 and NHLS1 is not evident in the observations for the two latter boxes. The worst agreement between our model and observations is found in the high stratosphere. Here the model matches the prominent structures (Figure 15*d*) but fails to reproduce the observed substructures (Figure 15*h*) possibly showing us some limits of our present approach.

3.5 Applications with beryllium and SF₆ in the southern hemisphere

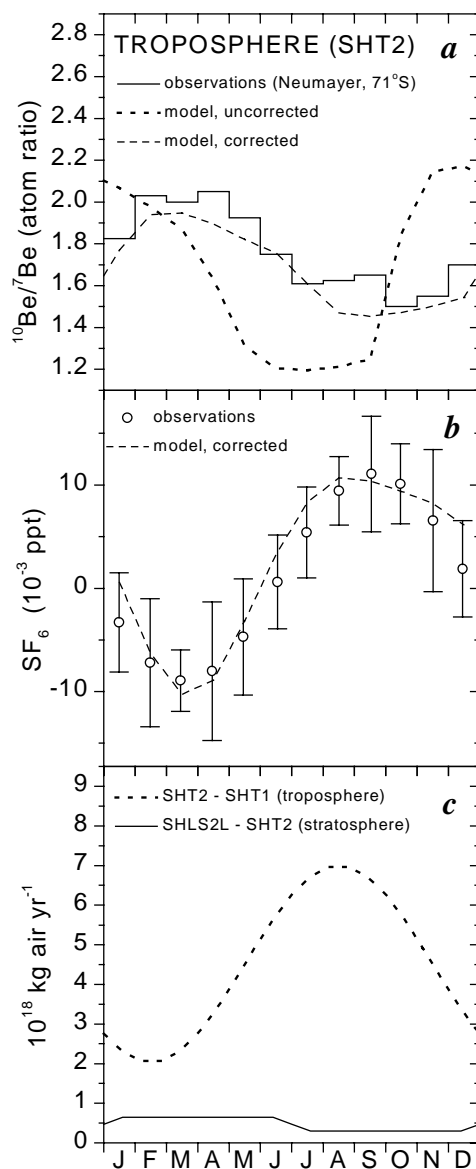
The bomb ^{14}C signals observed in the southern stratosphere are not pronounced enough to significantly constrain air mass cycling there. Hence we project the northern stratospheric parameterization to the southern hemisphere and shift the phase of southern seasonality by six

Figure 16 Results obtained after mirroring the northern stratospheric parameterization in Figure 13 to the southern hemisphere. *a*, The mirror model results for $^{10}\text{Be}/^7\text{Be}$ before and after correction are compared with observations from 1983-1985 at Neumayer [Wagenbach, 1996]. We use a mean ^7Be production of 5.56×10^{-2} atoms $\text{cm}_e^{-2} \text{s}^{-1}$ (cm_e^2 : square cm of Earth surface) [O'Brien, 1979] and a ratio of ^{10}Be production to ^7Be production of 0.6 [Dibb *et al.*, 1994]. The spatial repartition of the ^{10}Be and ^7Be production is the same as for ^{14}C [Lingenfelter, 1963]. The production rates of ^{10}Be , ^7Be and also of ^{14}C are modulated by $\pm 10\%$ with a period of 11 years to account for the cycle of solar activity [Stuiver and Quay, 1980]. The non radioactive removal of both, ^{10}Be and ^7Be occurs in the troposphere with a rate corresponding to the residence time for tropospheric aerosols. It was set to 0.5 months in the equatorial belts and to 1 month in the polar belts. *b*, The mean seasonal amplitude of SF_6 observations from 1988 to 1993 at Neumayer (Chapter 2, [Levin and Hesshaimer, 1996]) is compared to the corresponding seasonality in the mirror model after the $^{10}\text{Be}/^7\text{Be}$ -based correction and the fine-tuning of southern tropospheric meridional air mass exchange. *c*, Comparison of the strength of air mass exchange from the southern poleward box (SHT2) to the equatorward box (SHT1) with the corresponding strength of exchange to the stratosphere (SHLS2L) which together determine the residence time of air in SHT2 in the corrected mirror model.

months to compare model results (Figure 16a) with $^{10}\text{Be}/^7\text{Be}$ observed at the Coastal Antarctic station Neumayer (71°S , 42 m a.s.l.) ([Wagenbach, 1996]). The ratio of both cosmogenically produced isotopes ^{10}Be and ^7Be reflects the strength of stratospheric air mass intrusions into the troposphere. To match the observed $^{10}\text{Be}/^7\text{Be}$ seasonality with our model the time of maximal STE in the southern poleward stratosphere (SHLS2L) has to be retarded from December-January to March-April. In addition, the seasonal amplitude of STE has to be reduced by 50% in SHLS2L (Figure 16a). Accounting for these corrections the meridional air mass exchange between SHT2 and SHT1 can be fine tuned to reproduce SF_6 observations at Neumayer. This exchange peaks in August (Figure 16c) and controls 70% of the seasonal amplitude predicted for SF_6 in SHT2.

3.6 Comparison of our findings with present knowledge

How do our findings fit into the present knowledge of global STE? The low meridional mixing rate of 1.5 yr between the middle poleward stratosphere (NHLS2M) and the lowest equatorward stratosphere (NHLS1) confirms recent observational evidence for slow entrainment of mid-latitude air into the tropics [Volk *et al.*, 1996]. The phase shift between the maxima of exchange at the upper and at the lower boundary of the lowermost stratospheric box corroborates the updated picture of global stratospheric exchange processes [Holton *et al.*, 1995] and results of model based studies [Appenzeller *et al.*, 1996]. Also the weaker seasonal amplitude of poleward



STE in the southern than in the northern hemisphere as we inferred from $^{10}\text{Be}/^7\text{Be}$ observations is supported in these studies [Holton *et al.*, 1995; Appenzeller *et al.*, 1996]. Our stratospheric parameterization can not be independently confirmed by the low SF_6 concentrations observed above 20 km a.s.l. [Harnisch *et al.*, 1996] because these observations were used to supplementary constrain the mixing in the model high stratosphere. Nevertheless we can quantify a shortcoming which falsifies the residence time of air in the stratosphere determined from SF_6 . Comparing two model runs which respectively account or not for the destruction of SF_6 (atmospheric lifetime > 800 yr) presumed to take place above 50 km a.s.l. [Morris *et al.*, 1995] we find that 25% of the SF_6 concentration difference of 1.25 ppt between NHHS2 and NHT2 predicted for 1993 results from SF_6 destruction. This means that only 75% of this concentration difference can be attributed to the mean isolation time of stratospheric air from the tropospheric source. Hence the corresponding air isolation 'age' of 6 yr determined from the time lag of SF_6 concentration in the high stratosphere behind tropospheric observations [Harnisch *et al.*, 1996] overestimates the real isolation time by 30%.

3.7 Summary and conclusions

We investigated the cross-tropopause exchange of bomb radiocarbon (^{14}C) using a simple 14-box model of the atmosphere. Applying the adequate $^{14}\text{CO}_2$ fluxes across the northern hemispheric tropopause we reproduce observations of particularly high $^{14}\text{CO}_2$ seasonality in the free northern hemispheric troposphere [Levin *et al.*, 1992] and of bomb $^{14}\text{CO}_2$ inventories in the stratosphere [Telegadas, 1971]. The surprisingly good agreement even between substructures of these observations and model results provides quantitative insight into the strength and seasonality of stratospheric air mass cycling within the northern hemisphere. Most interesting results concern the middle poleward stratosphere. Here we find a residence time of 1.5 years for air with respect to mixing towards the Equator and correspondingly 1.7 years for air mixing with the underlying lowermost poleward stratosphere. The latter vertical exchange peaks during March to April. In contrast, the exchange of the lowermost poleward stratosphere with the troposphere takes only 0.5 years and peaks in June to July. A further particularity appears when we mirror the stratospheric parameterization of the northern hemisphere to the southern hemisphere and shift the phase of southern seasonality by six months. Then the ratio of ^{10}Be to ^7Be proves to be the crucial tracer for validation which demands that both a further phase shift of 3 months and a 50% reduction of the seasonal amplitude are applied to the southern poleward cross-tropopause exchange to reproduce tropospheric observations at high southern latitudes [Wagenbach, 1996].

The implications of our findings are manifold. First they confirm that the complexity of real air mass transport processes can be globally reduced to simple exchange patterns for tracers with atmospheric residence times longer than a couple of years. Second they confidently quantify global air mass exchange times and phases which can be used in further tracer studies. Finally they demonstrate consistency between the independently determined bomb strengths and stratospheric observations thus revalorizing both data sets to constrain global carbon cycle models. This will stimulate an exciting debate on the bomb ^{14}C inventory imbalance [Broecker and Peng, 1994; Heshaimer *et al.*, 1994]. The convenient way to solve this problem repeatedly focussed on depreciating the observed stratospheric inventories [Broecker *et al.*, 1995; Lassey *et al.*, 1996]. Our present study demonstrates that these inventories cannot be simply banished into oblivion and that we still have to seek for an acceptable solution to close the bomb ^{14}C budget.

CONCLUSIONS

Important new results of global relevance to our understanding of the carbon cycle can still be obtained using models which appear simplistic when compared to standard high-resolution models. This is essentially the merit of globally relevant long-term bomb $\Delta^{14}\text{C}$ observations, combined with an adequately simple modeling concept. Relying on this conviction we decided to still stay away from high-resolution when designing our seasonally modulated carbon cycle model with a 14-box atmosphere of which some results have been presented in the present Chapter 3. Our purpose with that model was threefold:

1. We intended to use an atmospheric model validated by tracer observations in its global air mass transport. This task was fulfilled in the meridional direction using SF_6 (see Appendix A.3 for some details) thus taking profit from our study in Chapter 1. A reliable vertical exchange through the tropopause was obtained from tracing bomb ^{14}C observations in the stratosphere while matching tropospheric $^{14}\text{CO}_2$ observations.
2. We wanted to underpin our fundamental working hypothesis relying on the global relevance of atmospheric $\Delta^{14}\text{C}$ monitoring. This task was achieved by proving the consistency of these observations tracking the global excursions of nuclear bomb ^{14}C . No evidence was found in the observed atmospheric $\Delta^{14}\text{C}$ signals since the early 1950s for significant inhomogeneities not explained by the 14-box model. Hence we do not agree with the conclusion of *Broecker et al.* [1995] depreciating atmospheric observations until 1965 (see section 3.1). Instead, we claim that the high-precision atmospheric $\Delta^{14}\text{C}$ monitoring started in the early 1950s *must* be continued to help closing the bomb ^{14}C budget.
3. Using the 14-box model with validated air mass exchange we wanted to understand the observed seasonal cycle of $^{14}\text{CO}_2$ in the troposphere since the 1980s showing a much stronger peak-to-peak amplitude of 6-8‰ in the northern than in the southern hemisphere (<2‰). Although this goal is not yet fully reached the preliminary results are promising. As an outlook I briefly present below three figures indicating why exciting findings concerning the ocean and the biosphere might be buried in the seasonal cycle of atmospheric $\Delta^{14}\text{C}$.

Figure 17 compares the mean seasonal modulation in ^{14}C of atmospheric CO_2 observed at the coastal Antarctic station Neumayer (71°S) [*Levin*, personal communication] with the model predictions for the corresponding box. In the first model run, the air-sea gas exchange coefficient was set according to seasonally variable fields adopted from the three-dimensional model TM2 ([*Heimann and Keeling*, 1989], see Appendix A.1.1). In the second run the air-sea gas exchange coefficient was set according to observational values from *Etcheto et al.* [1993] (see Appendix A.1.4). These preliminary results from our 14-box model the ^{14}C observations agree with the observed gas exchange coefficients. This is important because the observational gas exchange coefficients, traditionally considered to be too weak, corroborate our results from Chapter 2 indicating that the oceanic bomb ^{14}C inventory should be decreased.

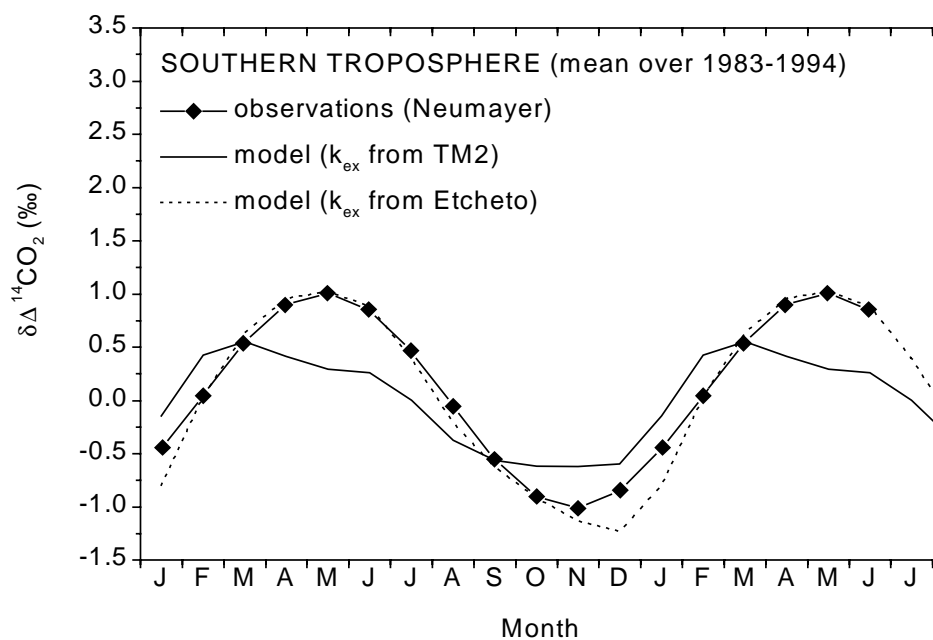


Figure 17 Mean over 1983-1994 of the seasonal $\Delta^{14}\text{C}$ component observed in CO_2 at Neumayer (71°S , 42m a.s.l.) This seasonal signal is compared with corresponding predictions from two runs of the atmospheric 14-box model with different gas exchange coefficient (k_{ex}) distributions (see text). The k_{ex} values from the TM2 were determined by Heimann and Monfray [1989]. The k_{ex} values from Etcheto *et al.* [1993] were read from the graphs of Figure 1 in *loc. cit.* $\delta\Delta^{14}\text{C}$ is the deviation of the observed $\Delta^{14}\text{C}$ concentrations from their long-term deseasoned trend.

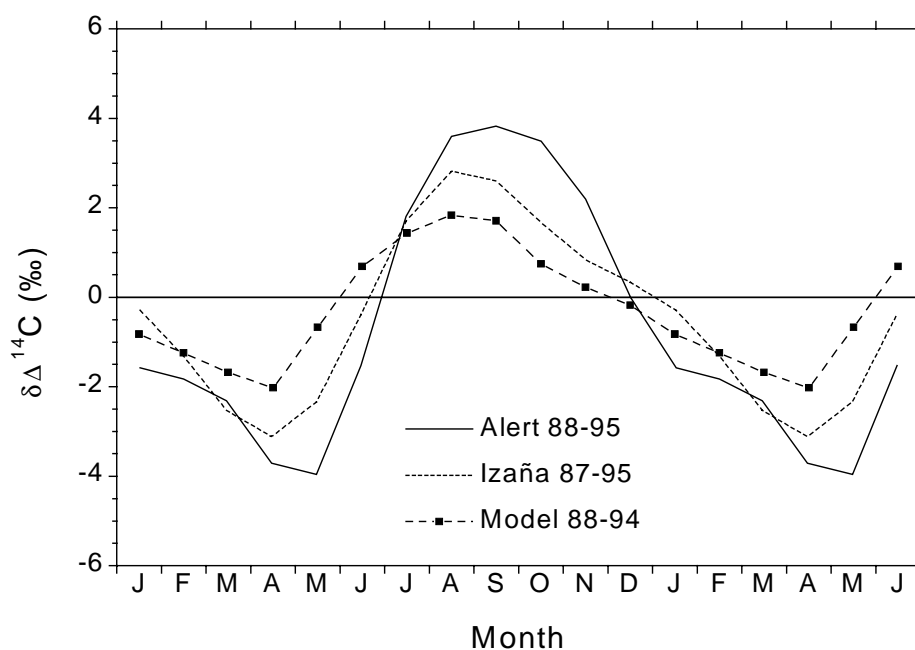


Figure 18 Mean seasonal cycles of $\Delta^{14}\text{CO}_2$ observed at Alert (82°N , 187m a.s.l.) and Izaña (28°N , 2367m a.s.l.) [Levin, personal communication] compared with the predictions of the atmospheric 14-box model for the tropospheric belt north of $+30^\circ$.

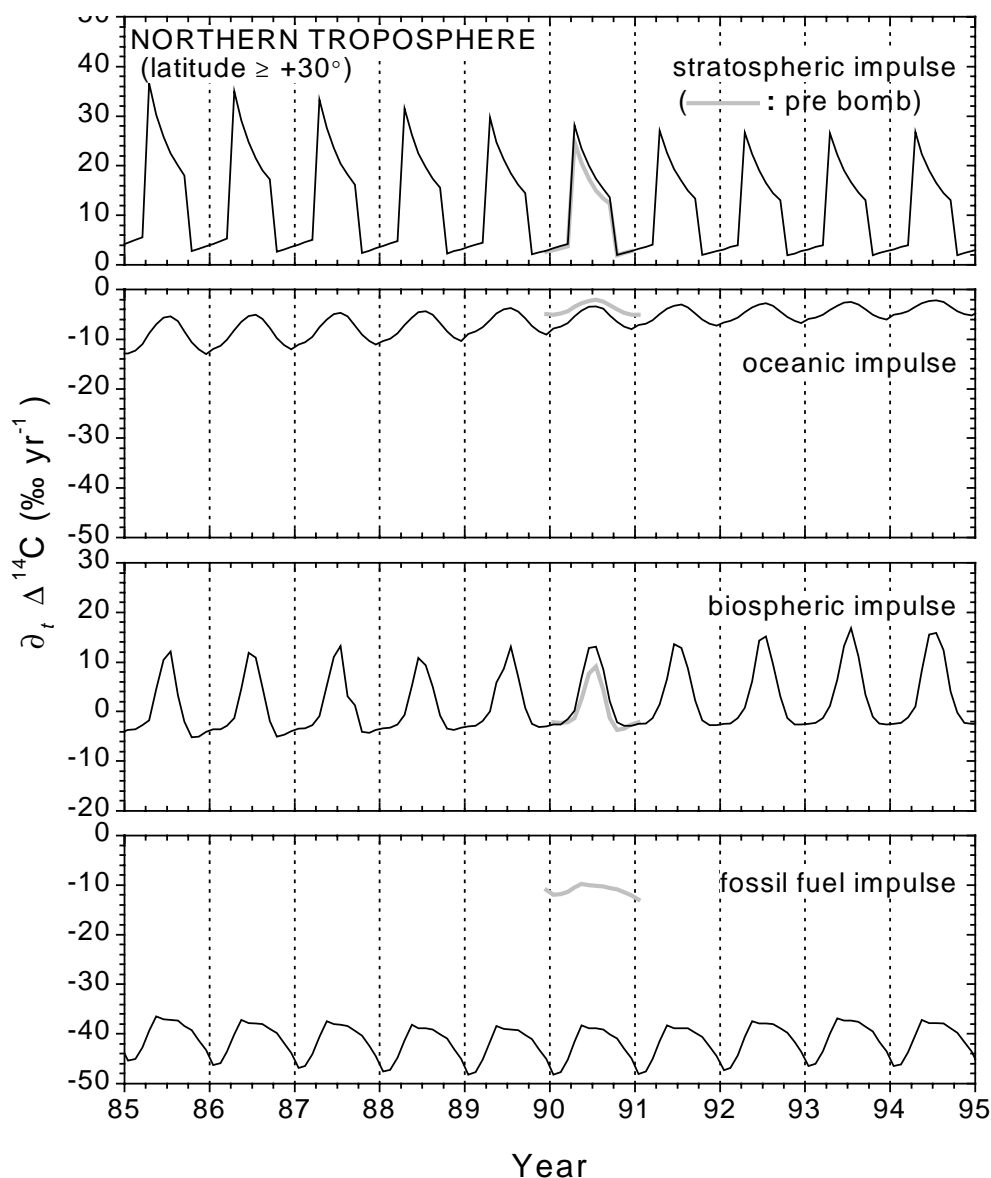


Figure 19 Comparison during 1985-1994 of the impulse contributions (see text) from the stratosphere, the ocean, the biosphere and from fossil fuels to the $\Delta^{14}\text{CO}_2$ seasonality in the northernmost troposphere of the 14-box model. The recent strengths of the impulses can be compared to corresponding pre-bomb values reported arbitrarily between 90 and 91.

Figure 18 compares the mean seasonal cycles in ^{14}C of atmospheric CO_2 at northern hemispheric clean air stations [Levin, personal communication] with corresponding results of the 14-box atmosphere model. The model results satisfactorily reproduce the phase in the observations but the peak-to-peak amplitude of the observed signals is by 50-100% higher than the model prediction. The strength of the time variation of $\Delta^{14}\text{C}$ is $\partial_t(\Delta^{14}\text{C})$ and can be easily determined in the 14 box model as a sum of "impulses" from individual carbon fluxes. In Figure 19 such impulses on $\Delta^{14}\text{C}$ of the model troposphere north of $+30^\circ$ are reported from 1985 to 1994. This allows to compare the individual impulses from the stratosphere, the ocean, the biosphere and from fossil fuel consumption to the model seasonality reported in Figure 18.

The seasonal modulations of all impulse components are shown in Figure 19 to have the same phase north of 30°N. The impulse values being higher during summer than during winter lead to a corresponding increase of the model $\delta\Delta^{14}\text{C}$ in Figure 18 from low values in April to high values in May. To produce a 50% higher model amplitude in Figure 18 a supplementary impulse component with a seasonal amplitude corresponding to the peak-to-peak amplitude of the stratospheric impulse is needed. Following evidence makes the biosphere a likely candidate to account for this missing seasonal impulse:

- Relying on our investigations in Chapter 3 the seasonality of the stratospheric impulse is accurately known within $\pm 30\%$.
- The seasonality of oceanic impulse is too weak and confined by observations (see Appendix A.1.4).
- The seasonality of fossil fuel impulse is constrained from statistical data [Rotty, 1987].
- The ^{14}C impulse of carbon released from the biosphere exerted on the atmospheric ^{14}C can be wrong by more than 100% depending on the sequestration time of carbon assimilated in the biosphere during the period of high atmospheric bomb ^{14}C activities.

Our parameterization of the biospheric pool sizes and turnover times (see Table 4 in Appendix A.2.2.8) corresponds to settings found in the recent literature. To provide a seasonality of the biospheric impulse more than twice as strong as the actual value this parameterization has to be sensibly modified with correspondent implications on our present day knowledge of the biosphere. Evidently, there is still much suspense left in modeling and monitoring the excursions of bomb radiocarbon.

APPENDIX

In the next sections A.1 and A.2 I present some details of the seasonally variable carbon isotope fluxes between the 14-box atmosphere and both the ocean and the biosphere. Section A.3 gives a few complements concerning the atmospheric 14-box model. Useful definitions and equations concerning radiocarbon are presented in section A.4.

A.1 Carbon and ^{14}C exchange ocean - troposphere

The results presented in Chapter 2 were based on an oceanic bomb ^{14}C inventory determined from a standard one dimensional box-diffusion ocean model [Oeschger *et al.*, 1975]. The bomb ^{14}C uptake determined from that model compares well with results from more refined models (see below, Figure 20) but provides neither the latitudinal distribution nor the seasonal variability of the radiocarbon exchange needed in the 14-box model. Therefore we implemented a more refined exchange with our 14-box atmosphere derived from two-dimensional distributions of the monthly carbon flux controlled by air-sea gas exchange. These carbon flux fields were previously used in the three-dimensional atmospheric transport model TM2 [Heimann and Keeling, 1989] and in the two-dimensional 2D-HD model [Hesshaimer, 1990] to simulate the atmospheric CO_2 in 1979. These fluxes do not explicitly account for carbon exchange with the marine biosphere. We calculated the radiocarbon exchange between the atmosphere and the ocean by combining these carbon fluxes with $\Delta^{14}\text{C}$ observations in the troposphere and in the ocean surface as described in the next subsections.

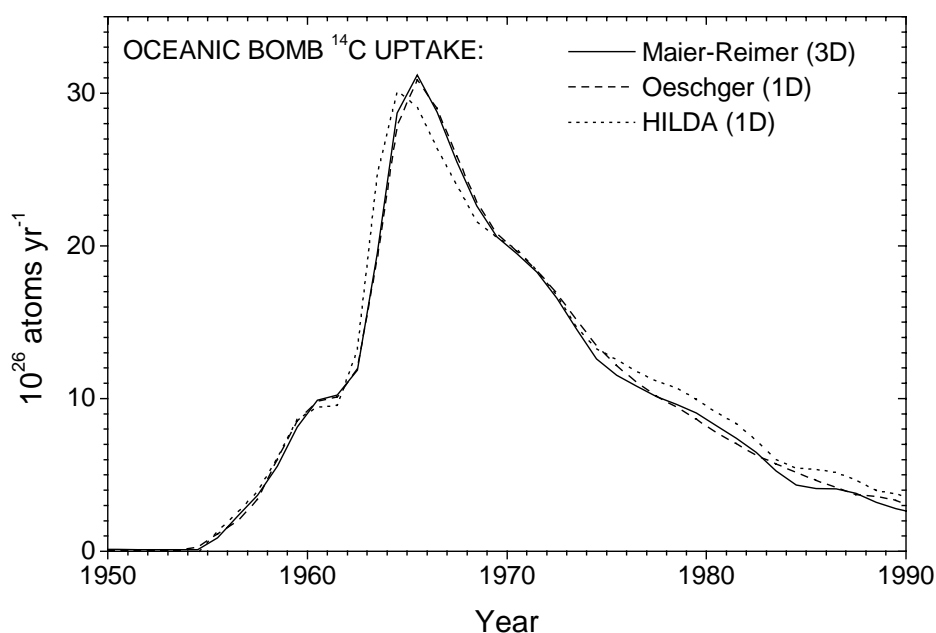


Figure 20 Comparison of oceanic bomb ^{14}C uptake fluxes predicted by three different ocean models. All three fluxes are normalized to match the Broecker inventory of $300 \cdot 10^{26}$ atoms on 1.1.1974. The flux obtained from the three-dimensional Hamburg Model of the Oceanic Carbon Cycle (HAMOCC) [Maier-Reimer, 1994, personal communication] agrees well with the one-dimensional predictions. The High-Latitude exchange/Interior Diffusion-Advection model (HILDA) [Siegenthaler and Joos, 1992] estimates are by F. Joos [1993, personal communication]. We constructed an Oeschger-type one-dimensional box-diffusion model [Oeschger *et al.*, 1975] to compute oceanic radiocarbon uptake needed for the global radiocarbon inventory study presented in Chapter 2.

A.1.1 Air-sea gas exchange and the TM2 carbon fluxes

The net carbon exchange flux F_{C_ex} per unit of time and of area results as sum of the positive carbon transfer flux F_{C_ao} from the atmosphere into the ocean and the correspondent negative reverse flux F_{C_oa} :

$$F_{C_ex} = F_{C_ao} + F_{C_oa} \quad (10)$$

The integral of F_{C_ex} over the surface of all world oceans is positive and corresponds to the uptake rate of excess anthropogenic CO₂ from the atmosphere into the ocean. F_{C_ex} was modeled in the TM2 [Heimann and Keeling, 1989] using the equation:

$$F_{C_ex} = k_{ex} \cdot (C_{CO2_atm} - C_{CO2_oce}) := k_{ex} \cdot \Delta C_{CO2_ao} \quad (11)$$

Here C_{CO2_oce} denotes the CO₂ concentration in dry air equilibrated under STP conditions with the DIC (Dissolved Inorganic Carbon) in the surface layer of the ocean. C_{CO2_atm} denotes the concentration of CO₂ with respect to dry air in the overlying atmosphere.

The gas exchange coefficient $k_{ex} = 6.6 \cdot 10^{-2}$ moles m⁻² yr⁻¹ ppm⁻¹ corresponding to a turnover time of the total atmospheric carbon inventory with respect to air-sea gas exchange of 7.87 years was used in the TM2 model [Heimann and Keeling, 1989] to determine the two-dimensional monthly net carbon exchange fluxes used in our work. The turnover time of 7.87 yr corresponds to a gross exchange flux F_{C_gross} of 90 GtC yr⁻¹ (see also Figure 1).

The value of ΔC_{CO2_ao} mainly depends on the CO₂ partial pressure of ocean surface waters which is modulated by changes in temperature, in the upwelling rate of subsurface waters, in horizontal water mass convection and in the photosynthesis activity of the marine biosphere. The seasonal and spatial variations of ΔC_{CO2_ao} entirely determine the variability of F_{C_ex} in the TM2 model fields because k_{ex} is kept constant.

We used the individual three field components of the TM2 model net oceanic carbon uptake:

$$F_{C_ex} = F_{C_seas} + F_{C_st} + F_{C_up} \quad (12)$$

The seasonal component F_{C_seas} accounts for all seasonal variations of CO₂ partial pressure at a given ocean surface location. The yearly mean carbon uptake from this component at a given ocean location is zero. In our work we used the same yearly TM2 model field of F_{C_seas} for all model years.

The stationary component F_{C_st} accounts for large scale stationary shifts in the ocean surface CO₂ partial pressure presumably reflecting the large scale transport of carbon within the ocean. This component leads to a carbon sink of 2 GtC yr⁻¹ in mid to high latitudes much more pronounced in the northern than in the southern hemisphere. This sink is balanced by carbon sources in the equatorial region so that the yearly mean carbon uptake from F_{C_st} integrated over all oceans is zero. In our work we used the same yearly TM2 model fields of F_{C_seas} for all model years.

The net carbon uptake component F_{C_up} which accounts for the net uptake of anthropogenic carbon by the ocean. The net flux F_{C_up} integrated over the surface of all oceans during 1979 corresponds to an oceanic uptake of 2.2 GtC yr⁻¹ in the TM2 model whereas the yearly mean gross fluxes F_{C_oa} and F_{C_ao} make up about 90 GtC yr⁻¹ (see also Figure 1). In our work we obtained the net yearly oceanic uptake by first determining the amount of yearly anthropogenic

CO_2 emission which has to be taken up by the biosphere and the ocean to preserve the global CO_2 increase observed in the troposphere [Neftel et al., 1985; Friedli et al., 1986; Siegenthaler et al., 1988; Keeling and Whorf, 1994]. Then we attributed 55% of this uptake to the oceanic carbon sink. This corresponds to a mean oceanic carbon sink during the 1980s of 2 GtC yr^{-1} in agreement with the value from IPCC 95 [1996] of $2 \pm 0.8 \text{ GtC yr}^{-1}$. Like in the TM2 this model uptake was uniformly distributed over the surface of the ice-free ocean.

The relation between $F_{C_{ao}}$ and the net uptake components $F_{C_{seas}}$, $F_{C_{st}}$ and $F_{C_{up}}$ is:

$$F_{C_{ao}} = F_{C_{gross}} + \begin{cases} F_{C_{seas}} & \text{if } F_{C_{seas}} > 0 \\ 0 & \text{else} \end{cases} + \begin{cases} F_{C_{st}} & \text{if } F_{C_{st}} > 0 \\ 0 & \text{else} \end{cases} + \begin{cases} F_{C_{up}} & \text{if } F_{C_{up}} > 0 \\ 0 & \text{else} \end{cases} \quad (13)$$

and a corresponding inverse relation is valid for $F_{C_{oa}}$. Although $F_{C_{seas}}$ and $F_{C_{st}}$ depend on the CO_2 gas exchange k_{ex} we did not modify these fluxes when reducing k_{ex} by 25% to balance the global bomb radiocarbon inventory. Despite their vanishing yearly average these two flux components nevertheless cycle carbon back and forth between the ocean and the atmosphere and thus contribute to the radiocarbon uptake by the ocean. However, this contribution to the oceanic radiocarbon uptake is by one to two orders of magnitude smaller than the total contribution from the gross carbon flux $F_{C_{gross}}$. On the other hand $F_{C_{seas}}$ and $F_{C_{st}}$ make up the entire contribution from the ocean to the seasonality of the atmospheric CO_2 signal and have been assessed in a comprehensive carbon cycle study using the TM2 [Heimann and Keeling, 1989; Heimann et al., 1989; Keeling et al., 1989b]. Therefore we preferred to neglect small inconsistencies in the radiocarbon uptake when maintaining $F_{C_{seas}}$ and $F_{C_{st}}$ unchanged and to keep the results of the comprehensive carbon cycle study.

Further, we use a meridionally and seasonally *variable* distribution of k_{ex} controlled by wind speed as implemented by Heimann and Monfray [1989] instead of the constant k_{ex} used to calculate the TM2 fields. This brings the oceanic radiocarbon uptake significantly closer to reality since wind is the driving force for the gas exchange peaking in high latitude (see Figure 23). The high gas exchange rate adds to increase the very low ocean surface $\Delta^{14}\text{CO}_2$ in southern hemispheric high latitudes (see Figure 21) and increase the southern ocean radiocarbon sink. The feedback on atmospheric CO_2 due to varying k_{ex} instead of being constant do not significantly affect the global oceanic radiocarbon uptake [Keeling et al., 1989b] and are neglected in the present study.

A.1.2 Ocean surface $\Delta^{14}\text{CO}_2$ determined from observation

Following method was used to determine ocean surface $\Delta^{14}\text{CO}_2$ values for the period between 1750 and 1995 from observations of Broecker et al. [1995]. First three mean meridional $\Delta^{14}\text{CO}_2$ profiles for 1957, 1973 and 1988 were obtained from the ocean surface observations (Figure 21). Then we assumed that the meridional shape of the pre-bomb profile for 1957 is also valid in 1750 and that the meridional *shape* of the profile for 1988 is valid in 1995. Then meridional profile shapes for each year between 1750 and 1995 were linearly interpolated from these five profiles. Finally all values from each profile were slightly shifted so that their mean value north of 60°N matches a function obtained from Appendix A.4.4. This function describes the time variation of

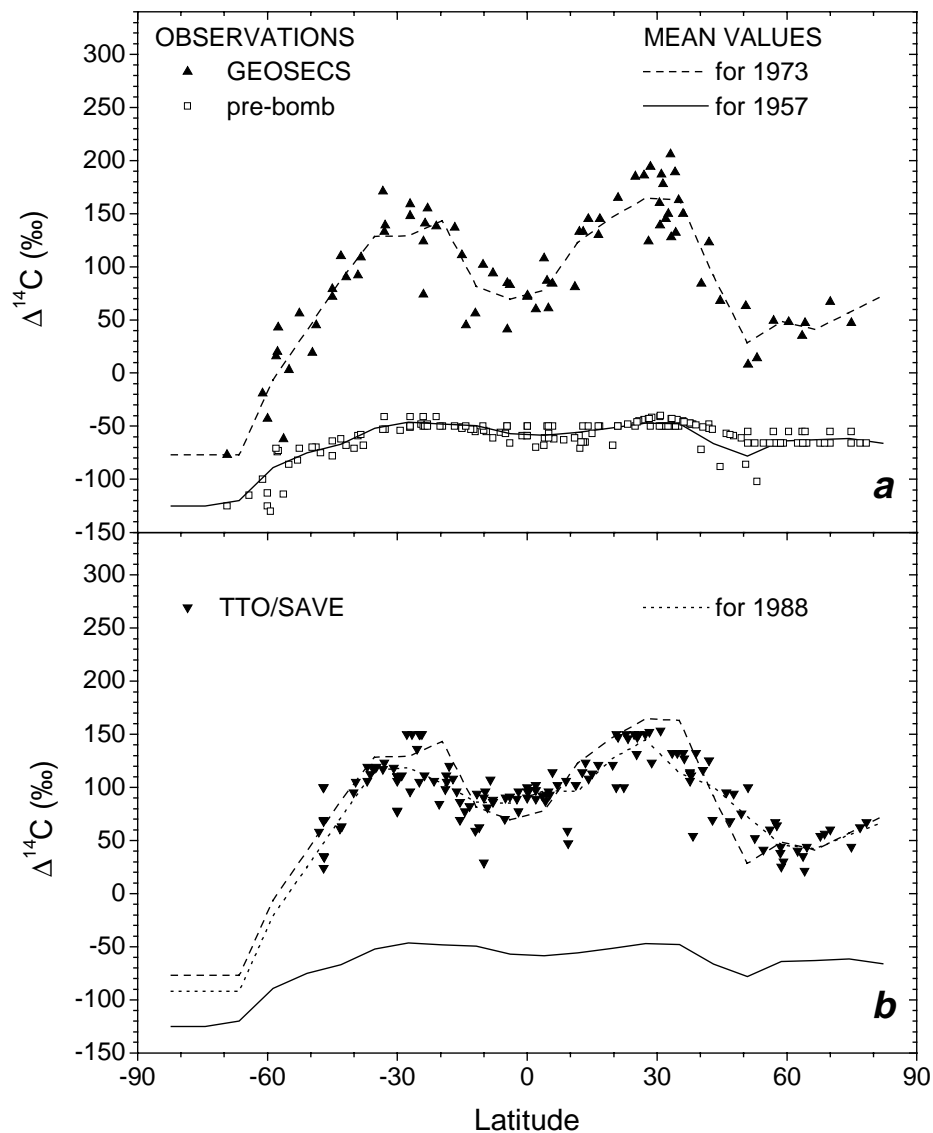


Figure 21 Worldwide observations of $\Delta^{14}\text{C}$ in dissolved inorganic carbon of ocean surface water as function of the geographical latitude [Broecker *et al.*, 1995]. The resulting mean meridional profiles were used to determine the oceanic radiocarbon uptake fluxes for our 14 box atmospheric model. *a*, The mean profile for 1957 is calculated from "pre-bomb" observations made before 1958. As the atmospheric $\Delta^{14}\text{CO}_2$ began to show nuclear bomb activity already in 1955 (Figure 14*b*) the "pre-bomb" profile is not free of bomb ^{14}C although the contamination is small (see A.1.2). The mean profile for 1973 is calculated from the observations of the GEOchemical Ocean SECTIONS Study (GEOSECS, 1972-1973) survey. *b*, The mean profile for 1988 is calculated from the Transient Tracers in the Ocean (TTO, 1980-1982) and from the South Atlantic Ventilation Experiment (SAVE, 1987-1989) surveys. The values for the 1988 profile south of 45°S were obtained by shifting the GEOSECS profile.

mean ocean surface $\Delta^{14}\text{CO}_2$ north of 60°S better than does the linear interpolation between the five initial profiles. After these corrections the profiles for 1957, 1973 and 1988 still agree with their initial values and compare well with ^{14}C activities measured in corals (see Figure 22).

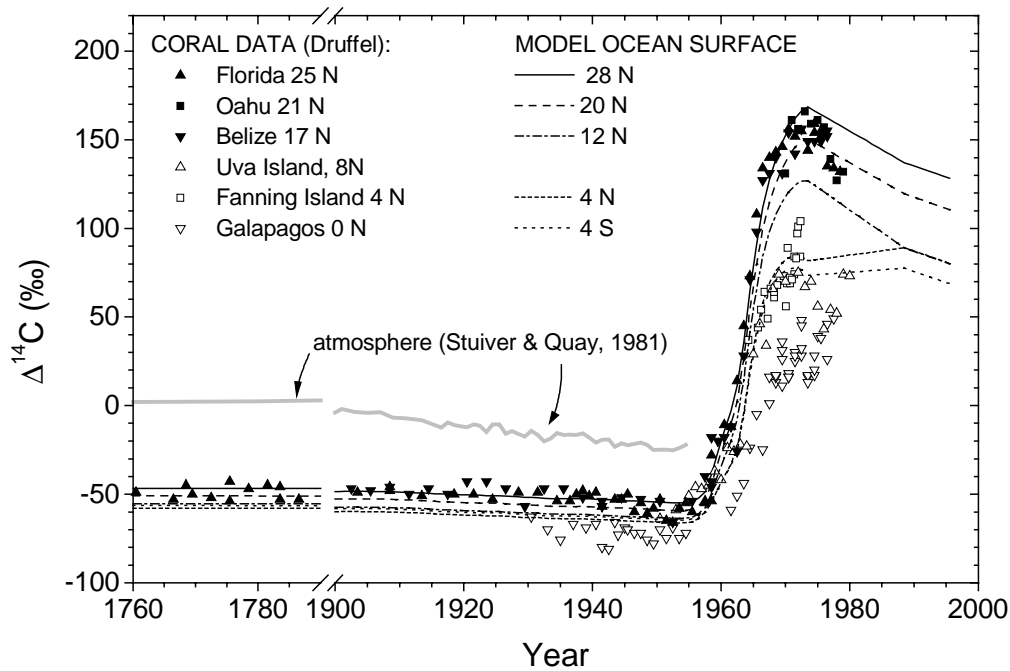


Figure 22 Comparison of the time variation of $\Delta^{14}\text{C}$ measured in banded corals with the $\Delta^{14}\text{C}$ activity determined for the model ocean surface. The coral samples were collected in Florida and Belize [Druffel, 1980], on the Galápagos Islands [Druffel, 1981], on Oahu Island (Hawaii), Uva Island (Panama) and Fanning Island (4°N, 159°W) [Druffel, 1995]. The model ocean surface values decrease by 8‰ between 1760 and 1955 due to the Sues Effect which can be seen in the included atmospheric ^{14}C activities based on tree ring measurements from northern hemispheric mid-latitudes [Stuiver and Quay, 1981]. The record from Stuiver and Quay begins in 1820 and we used a constant value of 2‰ for $\Delta^{14}\text{CO}_2$ in the northern hemisphere between 1750 and 1820.

A.1.3 The radiocarbon exchange between atmosphere and ocean

Radiocarbon uptake to the ocean is controlled by gas exchange and to a minor degree by net carbon uptake. CO_2 absorbed from the atmosphere by the ocean surface has essentially the radiocarbon activity signature of atmospheric CO_2 . Isotope fractionation at the air-sea interface slightly reduces this activity by the factor $\alpha_{14\text{C}_{ao}} = (0.998)^2 = 0.996$ [Siegenthaler and Münnich, 1981]. To obtain the radiocarbon flux corresponding to a carbon transfer flux per unit of time and of area $F_{C_{ao}}$ from the atmosphere into the ocean we first determined the radiocarbon activity A_{atm} of atmospheric CO_2 from the corresponding atmospheric $\Delta^{14}\text{C}$ observations using the equation (63) in Appendix A.4.2. Then the radiocarbon flux $F_{14\text{C}_{ao}}$ was computed according to equation:

$$F_{14\text{C}_{ao}} = F_{C_{ao}} \cdot A_{atm} \cdot \alpha_{14\text{C}_{ao}} \quad (14)$$

CO_2 released from the ocean surface to the atmosphere correspondingly has the radiocarbon activity signature of ocean surface carbon reduced by a fractionation factor of $\alpha_{14\text{C}_{oa}} = (0.9897)^2 = 0.9795$ [Mook et al., 1974].

The radiocarbon flux $F_{14\text{C}_{oa}}$ from the ocean to the atmosphere was obtained from the corresponding carbon flux $F_{C_{oa}}$ and the radiocarbon activity A_{oce} observed in DIC (Dissolved

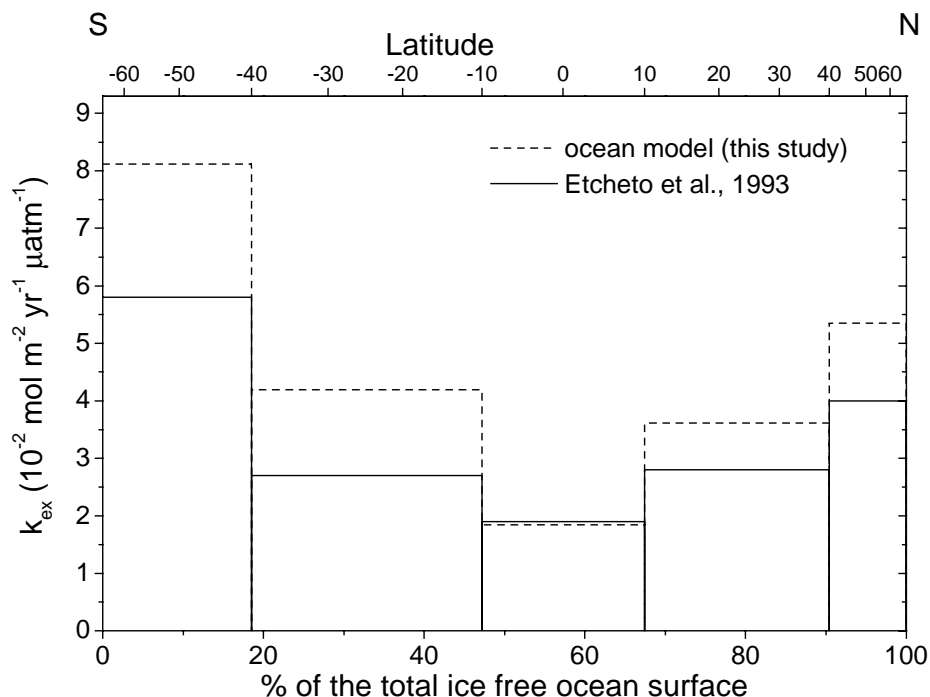


Figure 23 The yearly means of the CO_2 gas exchange coefficient k_{ex} used in our model averaged over each of five latitudinal belts are compared with corresponding values obtained from observations [Etcheto et al., 1993]. The observational values base on data obtained from the GEOSAT and from the SSM/I satellites are validated through comparison with in situ measurements at sea level [Boutin and Etcheto, 1996]. The observational means were read with an accuracy estimated better than $\pm 10\%$ from the SSM/I data in the Figure 1 of *loc. cit.* reporting the time variation of k_{ex} between 1985 and 1992 as average over $80^\circ\text{S}-40^\circ\text{S}$, $40^\circ\text{S}-10^\circ\text{S}$, $10^\circ\text{S}-10^\circ\text{N}$, $10^\circ\text{N}-40^\circ\text{N}$ and $40^\circ\text{N}-80^\circ\text{N}$.

Inorganic Carbon) of the ocean surface according to equation:

$$F_{14C_{oa}} = F_{14C_{oa}} \cdot A_{oce} \cdot \alpha_{14C_{oa}} \quad (15)$$

A.1.4 Mean gas exchange rate balancing the bomb ^{14}C inventory

To obtain an oceanic bomb radiocarbon inventory amounting only 75% of the Broecker inventory [Broecker et al., 1995] we used a mean gas exchange rate of $k_{ex}=4.55 \cdot 10^{-2} \text{ mol m}^{-2} \text{ yr}^{-1} \text{ ppm}^{-1}$. This rate is 30% lower than the $6.6 \cdot 10^{-2} \text{ mol m}^{-2} \text{ yr}^{-1} \text{ ppm}^{-1}$ adopted to calculate the TM2 fields. However the latter rate is higher than the published values of $(5.4-6.3) \cdot 10^{-2} \text{ mol m}^{-2} \text{ yr}^{-1} \text{ ppm}^{-1}$ determined from one-dimensional ocean models [Siegenthaler and Oeschger, 1987; Siegenthaler and Joos, 1992]. Furthermore CO_2 air-sea transfer coefficients obtained from wind tunnel experiments [Liss and Merlivat, 1986] confirmed by direct measurements at sea [Watson et al., 1991] lead to a global average gas exchange rate of $k_{ex}=3.2-4 \cdot 10^{-2} \text{ mol m}^{-2} \text{ yr}^{-1} \text{ ppm}^{-1}$ [Etcheto and Merlivat, 1988; Etcheto et al., 1991; Boutin and Etcheto, 1996] when combined with remotely sensed wind fields.

The meridional shape of our model ocean gas exchange rate (Figure 24) compares well with such observational values [Etcheto et al., 1993]. The model estimates give even more weight to the

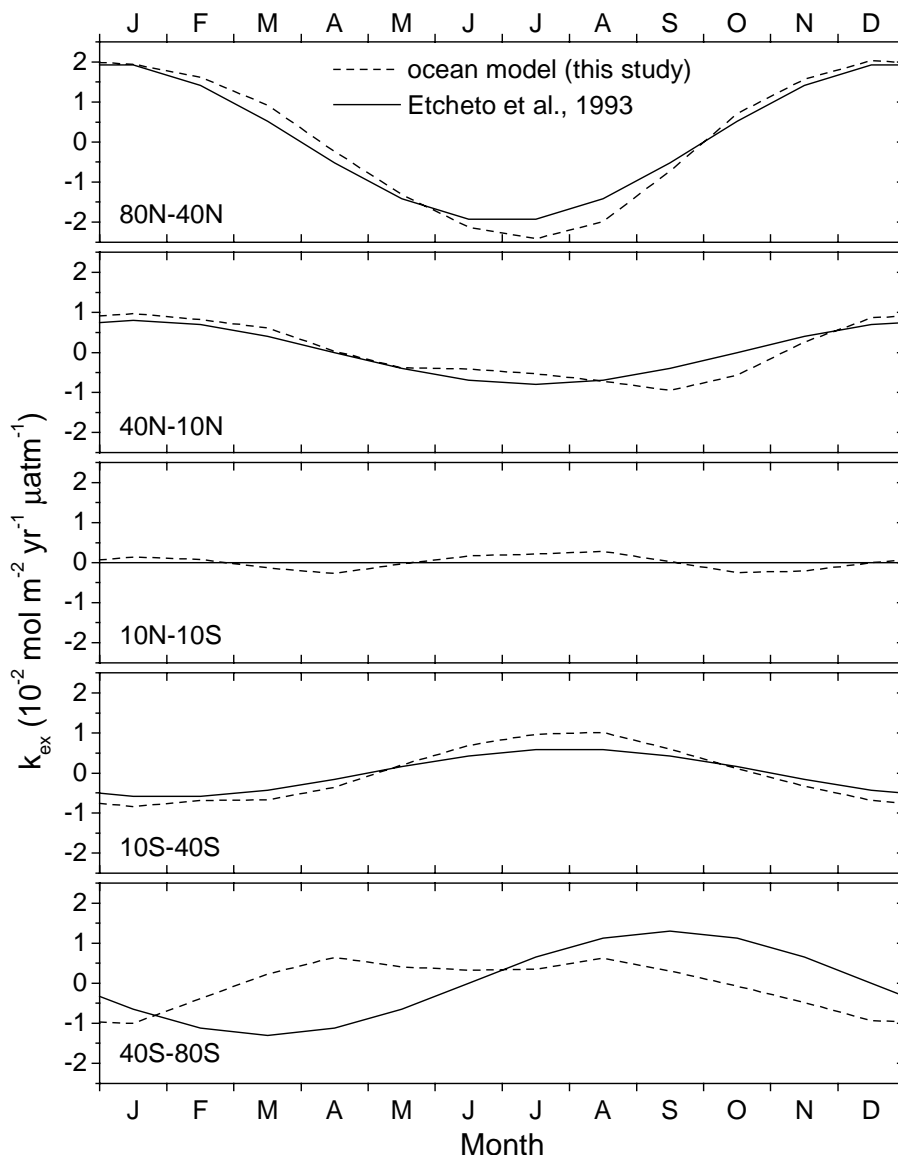


Figure 24 The mean seasonal variations of the CO_2 gas exchange coefficient used in our model ocean averaged over five latitudinal belts are compared with corresponding values obtained from observations [Etcheto et al., 1993]. The observations are described in Figure 23. The mean peak to peak amplitude and the phase of a sine curve approximating the observations were read from the SSM/I data in Figure 1 of *loc. cit.* with an accuracy estimated to be better than $\pm 20\%$ and ± 1 month respectively.

maximum gas exchange coefficients in high latitudes than the remotely sensed values. The seasonal variation of model gas exchange strength in different latitudinal bands agrees in both amplitude and phase with the observations except for the mid to high southern latitudes (Figure 24). There the model predictions are minimum in December to January which is two to three months later than observational values.

A.1.5 Remark concerning the definition of the oceanic bomb ^{14}C inventory

The bomb radiocarbon inventory determined by Broecker from the GEOSECS observations [Broecker et al., 1985; Broecker et al., 1995] considers only the difference in $\Delta^{14}\text{C}$ between ocean profiles for 1974 and ocean profiles for pre-bomb time assumed to be around 1955. It does

not account for most of the supplementary radiocarbon amount which is carried into the ocean by anthropogenic CO_2 . Therefore if the total bomb ^{14}C inventory $\Delta N_{^{14}\text{C}_{\text{oce}}}$ of an ocean model in 1974 is determined from the difference between the ^{14}C inventories in 1974 and in 1955 then a correction is necessary before comparing with the Broecker bomb ^{14}C inventory according to the expression:

$$\Delta N_{^{14}\text{C}_{\text{oce}}}^* = \Delta N_{^{14}\text{C}_{\text{oce}}} - \Delta N_{\text{C}_{\text{oce}}} \cdot \langle A(\Delta N_{\text{C}_{\text{oce}}}) \rangle \quad (16)$$

Here $\Delta N_{^{14}\text{C}_{\text{oce}}}^*$ is the oceanic bomb ^{14}C inventory to be compared to the Broecker inventory, $\Delta N_{\text{C}_{\text{oce}}}$ is the net amount of anthropogenic carbon taken up by the ocean between 1955 and 1974 and $\langle A(\Delta N_{\text{C}_{\text{oce}}}) \rangle$ is the mean activity in 1974 per carbon amount of $\Delta N_{\text{C}_{\text{oce}}}$. The value of $\langle A(\Delta N_{\text{C}_{\text{oce}}}) \rangle$ depends on the depth to which the carbon amount $\Delta N_{\text{C}_{\text{oce}}}$ has penetrated into the ocean. We determined that the correction term $\Delta N_{\text{C}_{\text{oce}}} \cdot \langle A(\Delta N_{\text{C}_{\text{oce}}}) \rangle$ makes up about $15 \cdot 10^{26}$ atoms which is 5% of the Broecker bomb ^{14}C inventory for 1.1.1974.

A.1.6 Preindustrial oceanic ^{14}C uptake and cosmic ray ^{14}C production

From our CO_2 gas exchange rate k_{ex} and from preindustrial values for the $\Delta^{14}\text{C}$ in the atmosphere [Stuiver and Quay, 1981] and the ocean surface [Druffel and Suess, 1983] we determine the equilibrium uptake of oceanic radiocarbon assumed for 1750. If we add to this uptake the rate of radiocarbon decay in the equilibrium biosphere and atmosphere we obtain a total ^{14}C sink from the preindustrial atmosphere of $2.2 \cdot 10^{26}$ atoms yr^{-1} . The latter value amounts only to 80% of the $2.8 \cdot 10^{26} \pm 10\%$ atoms yr^{-1} estimated for cosmic ray ^{14}C production during industrialization [O'Brien, 1979; Stuiver and Quay, 1980; O'Brien et al., 1991]. This is due to the fact that we did not account for all carbon reservoirs *in contact with the atmosphere* in our model. We neglected the cycling of carbon through buried and reactive sediment reservoirs like coastal wetlands, continental shelves and freshwater lakes because this cycling is too slow to significantly affect the time scale of a few decades on which the bomb ^{14}C perturbation occurs. However these pathways of carbon cycle become relevant on the millennial time scale of radiocarbon lifetime and may well accumulate 20% of the Earth ^{14}C inventory [Damon and Sternberg, 1989].

As we focussed on the nuclear bomb perturbation to the radiocarbon cycle we considered only a modulation by $\pm 10\%$ of the mean cosmic ray ^{14}C production reflecting the 11 year cycle of solar activity [Stuiver and Quay, 1980]. We did not account for secular variations of ^{14}C attributed to solar modulation of the cosmic ray flux or to changes in the earth geomagnetic field intensity [O'Brien et al., 1991] because the corresponding changes in atmospheric $\Delta^{14}\text{CO}_2$ were less than $\pm 20\%$ during the present millenium [Stuiver and Quay, 1980].

A.1.7 Discussion on k_{ex} and the oceanic ^{14}C inventory

With our model ocean gas exchange reduced to match 75% of the Broecker inventory in 1974 we come closer to the observational values of k_{ex} than without correction. This is one of the evidences supporting an oceanic solution to the bomb radiocarbon inventory mismatch presented in Chapter 2.

From our low k_{ex} we obtain an oceanic equilibrium uptake of radiocarbon through gas exchange of $2.0 \cdot 10^{26}$ atoms yr^{-1} . If summed up over the lifetime of radiocarbon this uptake leads to an inventory of $8270 \cdot 2.0 \cdot 10^{26}$ atoms = $16540 \cdot 10^{26}$ atoms ^{14}C which is lower by about 20% than values for radiocarbon in DIC of the preindustrial ocean from other authors [Lassey et al., 1990]. However we think that our low preindustrial oceanic radiocarbon inventory is acceptable because

it is not in contradiction with the cosmic ray ^{14}C production as discussed in Appendix A.1.6.

The seasonal variation of our model k_{ex} adopted from the TM2 should be corrected in southern high latitudes (Figure 24) to better match the observational values. These observations indicate that winds peak during July to September in the southern hemisphere and thus peak at about the same time as the meridional air mass transport obtained in Chapter 3 (Figure 16c).

A.2 Carbon and ^{14}C exchange biosphere - troposphere

Radiocarbon uptake by the ocean is constrained by worldwide $\Delta^{14}\text{C}$ observations from the sea surface down to the deepest water layers. These constraints allowed us to determine the ^{14}C uptake through the air-sea boundary in Appendix A.1 without running a complete ocean model. Unfortunately no such observations are available for the biosphere and biospheric carbon models must be used to quantify this exchange. To cycle bomb ^{14}C through the biosphere these models must account for the time delay between assimilation through net primary productivity (NPP) of a bomb ^{14}C spiked carbon amount and its release back to the atmosphere through decomposition. In the next two sections I present the simple fundamentals on which the mixed biosphere model used in chapter two and the more realistic statistical biosphere used in chapter three are based.

A.2.1 The mixed biosphere box model

A.2.1.1 Cycling of carbon

A very simplified picture of the biosphere subdivides it into three major reservoirs. The first reservoir cycles carbon within a few years and contains all leaves, grasses, fine roots as well as fast decomposed fractions of litter. The second reservoir includes bulky wooden structures like stems and big roots removing carbon from the atmosphere for several decades. This reservoir includes a soil and litter carbon fraction with correspondingly slow decomposition rate. The third reservoir contains soil carbon which is more resistant to decomposition and where carbon has a mean residence time of several centuries.

We consider the carbon amount $dI(t_0)=F_{C_inp}(t_0)dt$ taken up (e.g. through NPP) according to a carbon flux $F_{C_inp}(t_0)$ at time t_0 in one of these mixed reservoirs. F_{C_inp} is defined positive if carbon is assimilated in the biosphere. The part $dI(t, t_0)$ of this input which has not left the reservoir due to decomposition until time $t \geq t_0$ is:

$$dI(t, t_0) = F_{C_inp}(t_0) \cdot \exp\left(-\frac{t-t_0}{\tau_{dec}}\right) dt_0 \quad (17)$$

Here τ_{dec} is the e-folding time for decomposition. This formulation is most adequate for the soil carbon reservoir because carbon is decomposed here as soon as it enters. The situation is different in the two other reservoirs where carbon is fixed (e.g. in the leaves or in the stem) for a while before being decomposed. Here it is argued that $F_{C_inp}(t_0)$ is assimilated at the same time in elements of these reservoirs (e.g. a leaf or a stem) which have different degrees of maturity between birth and death. Although part of $F_{C_inp}(t_0)$ is fixed for longer in young elements of the reservoir other parts of $F_{C_inp}(t_0)$ are decomposed soon, after death of old elements. This residence behavior is approximated at the reservoir scale by a decreasing exponential. The mixed reservoir approach is widely used in literature [Siegenthaler and Oeschger, 1987; Keeling et al., 1989a; Broecker and Peng, 1994] and we adopted it in chapter two for its simplicity.

The total carbon mass $M_{res}(t)$ in such a biospheric carbon reservoir is the integral over all inputs of the part remaining in the reservoir:

$$M_{res}(t) = \int_{-\infty}^t F_{C_inp}(\xi) \cdot \exp\left(\frac{\xi-t}{\tau_{dec}}\right) d\xi \quad (18)$$

In the case of constant input $F_{C_inp}(t)=F_{C_inp_cst}$, the last equation can be solved and results in a constant reservoir mass M_{res_cst} :

$$M_{res_cst} = F_{C_inp_cst} \cdot \tau_{dec} \quad (19)$$

The carbon decomposition flux F_{C_dec} from the reservoir to the atmosphere is:

$$F_{C_dec}(t) = - \int_{-\infty}^t \partial_t \left(F_{C_inp}(\xi) \cdot \exp\left(\frac{\xi-t}{\tau_{dec}}\right) \right) d\xi = \frac{M_{res}(t)}{\tau_{dec}} \quad (20)$$

This flux does not depend on the time history of $F_{C_inp}(t)dt$ inputs which have lost their identity as if the reservoir would be well-mixed. This is the reason why we speak of a *mixed biosphere model* in this section.

The mean residence time (also called the mean transit time) T_{res} for carbon in a reservoir is the mean over all outputs of the time they have spent in the reservoir (if analogously replacing carbon atoms in a reservoir by humans beings in a population, the mean residence time of carbon would become the mean lifetime of the population) [Bolin and Rodhe, 1973]. Here it is determined after weighting the time each output has spent in the reservoir with its corresponding output strength. In the case of constant input $F_{C_inp_cst}$ we obtain:

$$\begin{aligned} T_{res} &:= \frac{- \int_{-\infty}^t (t-\xi) \partial_t \left(F_{C_inp_cst} \exp\left(\frac{\xi-t}{\tau_{dec}}\right) \right) d\xi}{- \int_{-\infty}^t \partial_t \left(F_{C_inp_cst} \exp\left(\frac{\xi-t}{\tau_{dec}}\right) \right) d\xi} \\ &= \frac{F_{C_inp_cst} \cdot \tau_{dec}}{F_{C_inp_cst}} = \tau_{dec} \end{aligned} \quad (21)$$

The mean carbon age T_{age} in a reservoir is the mean over all carbon amounts in a reservoir of the time passed since they entered the reservoir [Bolin and Rodhe, 1973] (in analogy to the mean age of a human population). Here it is obtained after weighting the time each element has spent in the reservoir with the carbon mass of this element. In the case of constant input $F_{C_inp_cst}$ we obtain:

$$\begin{aligned} T_{age} &:= \frac{\int_{-\infty}^t (t-\xi) F_{C_inp_cst} \exp\left(\frac{\xi-t}{\tau_{dec}}\right) d\xi}{\int_{-\infty}^t F_{C_inp_cst} \exp\left(\frac{\xi-t}{\tau_{dec}}\right) d\xi} \\ &= \frac{F_{C_inp_cst} (\tau_{dec})^2}{F_{C_inp_cst} \cdot \tau_{dec}} = \tau_{dec} \end{aligned} \quad (22)$$

The turnover time T_{turn} of a reservoir is usually expressed as the ratio of the total mass in the

reservoir to the gross output flux [*Bolin and Rodhe, 1973*]:

$$T_{turn} := \frac{M_{res}(t)}{F_{C_dec}(t)} = \tau_{dec} \quad (23)$$

The equivalence $\tau_{dec}=T_{res}=T_{age}=T_{turn}$ valid in the case of constant input flux $F_{C_inp_cst}$ is the reason why the terms *age*, *residence time* and *turnover time* are often used without distinction. It is worth noticing that this equivalence is a pleasant property of the mixed biosphere model which is not generally valid (see the statistical biosphere).

A.2.1.2 Cycling of radiocarbon

Significant $\delta^{13}\text{C}$ fractionation with $\alpha_{13\text{C}} = 0.9819$ (this value is obtained considering that atmospheric carbon with $\delta^{13}\text{C} = -7\text{‰}$ has $\delta^{13}\text{C} = -25\text{‰}$ after assimilation, [*Siegenthaler and Oeschger, 1987*]) and corresponding $\Delta^{14}\text{C}$ fractionation with $\alpha_{14\text{C}} = (\alpha_{13\text{C}})^2$ occurs when CO_2 is assimilated in plant tissues through photosynthesis. No fractionation is considered during decomposition of organic carbon. Thus the mean $^{14}\text{C}/\text{C}$ activity A_{res} in a reservoir is (e.g. in Bq per kgC):

$$A_{res}(t) = \frac{1}{M_{res}(t)} \int_{-\infty}^t F_{C_inp}(\xi) \cdot \alpha A_{inp}(\xi) \cdot \exp\left((\xi - t) \cdot \left(\frac{1}{\tau_{dec}} + \lambda\right)\right) d\xi \quad (24)$$

where M_{res} is the carbon mass in the reservoir, α is the fractionation factor for ^{14}C input (see Appendix A.4.3 for the approximation concerning α), $A_{inp}(t)$ is the activity (e.g. in Bq per kgC) of the carbon input before fractionation, λ^{-1} is the mean radioactive lifetime of ^{14}C and $\alpha \cdot A_{inp}(\xi) \cdot \exp(-\lambda(t-\xi))$ is the activity at time t of a carbon amount entered at time ξ . If both the carbon input flux $F_{C_inp}(t) = F_{C_inp_cst}$ and the activity $A_{inp}(t) = A_{inp_cst}$ are constant, the reservoir activity is also constant:

$$A_{res}(t) = \frac{\alpha A_{inp_cst}}{1 + \tau_{dec} \lambda} := A_{res_cst} \quad (25)$$

The mean activity $A_{out}(t)$ of the carbon leaving the reservoir through decomposition is equal to the mean activity in that reservoir:

$$\begin{aligned} A_{out}(t) &= \frac{-1}{F_{C_dec}(t)} \int_{-\infty}^t F_{C_inp}(\xi) \cdot \alpha A_{inp}(\xi) \cdot \exp(\lambda(\xi - t)) \cdot \partial_t \exp\left(\frac{\xi - t}{\tau_{dec}}\right) d\xi \\ &= A_{res}(t) \end{aligned} \quad (26)$$

where we used equation (20) to replace $F_{C_dec}(t)$.

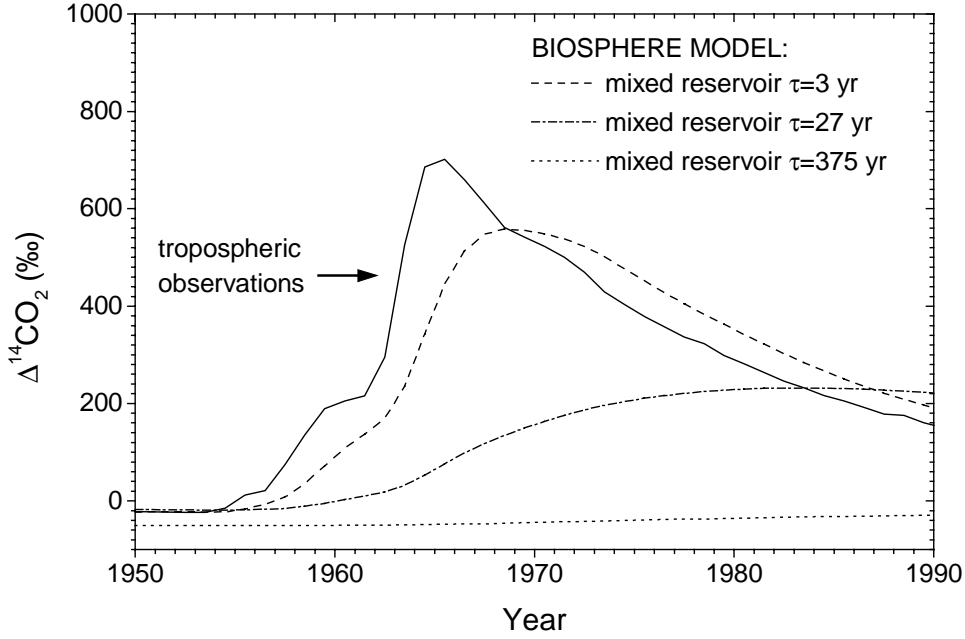


Figure 25 Comparison between the atmospheric $\Delta^{14}\text{CO}_2$ and mean $\Delta^{14}\text{C}$ activities predicted for mixed biosphere reservoirs cycling atmospheric carbon at different turnover rates. The turnover times of the individual reservoirs are those we already used in Chapter 2.

A.2.1.3 Numerical realization of the mixed biosphere model

Equation (20) shows that the output fluxes of carbon from the mixed reservoir depend only on the instantaneous total carbon amount in the reservoir and on the e-folding time for decomposition τ_{dec} . Equation (26) shows that also the activity of this carbon output depends only on the mean activity in the mixed reservoir. This independence from the details of input history simplifies the computational effort needed to program the mixed model numerically but will not remain valid in the statistical biosphere model. Our numerical approach consists in first reformulating equation (24) with constant reservoir mass M_{res_cst} and constant carbon input flux $F_{C_inp_cst}$ to obtain a recursive equation:

$$\begin{aligned}
 A_{res}(t_n) &= \frac{1}{M_{res_cst}} \int_{-\infty}^{t_{n-1}} F_{C_inp_cst} \cdot \alpha A_{inp}(\xi) \cdot \exp\left((\xi - t_n)\left(\frac{1}{\tau_{dec}} + \lambda\right)\right) d\xi \\
 &+ \frac{1}{M_{res_cst}} \int_{t_{n-1}}^{t_n} F_{C_inp_cst} \cdot \alpha A_{inp}(\xi) \cdot \exp\left((\xi - t_n)\left(\frac{1}{\tau_{dec}} + \lambda\right)\right) d\xi \\
 &= A_{res}(t_{n-1}) \cdot \exp\left((t_{n-1} - t_n)\left(\frac{1}{\tau_{dec}} + \lambda\right)\right) \\
 &+ \frac{1}{\tau_{dec}} \int_{t_{n-1}}^{t_n} \alpha A_{inp}(\xi) \cdot \exp\left((\xi - t_n)\left(\frac{1}{\tau_{dec}} + \lambda\right)\right) d\xi
 \end{aligned} \tag{27}$$

Then the last equation is solved in yearly steps $\{t_i, i=1 \dots n\}$ for each of the three reservoirs of the

mixed biosphere model in Chapter 2. In the two reservoirs containing leaves and bulky wood $A_{inp}(t)$ is determined from atmospheric observations with $\alpha = \alpha_{14C_{ab}}$. Yearly mean atmospheric $\Delta^{14}CO_2$ observations and equation (63) from Appendix A.4.2 are used to determine $A_{inp}(t)$ ongoing from preindustrial equilibrium at $t_0=1750$. The initial value for $A_{res}(t_0)$ is obtained from equation (25). The input activity to the soil carbon reservoir is the mean of the activity of the two other reservoirs and $\alpha=1$ is used. Figure 25 shows the time variation predicted for $\Delta^{14}C$ since 1950 in each reservoir of the biospheric model from Chapter 2. This Figure shows that the $\Delta^{14}C$ of the mixed wood reservoir steps over the atmospheric values during the mid 1980s. Ongoing from that date carbon decomposed from the mixed wood reservoir acts as a "source" of $\Delta^{14}C$ to the atmosphere.

A.2.2 The statistical biosphere box model

There were two reasons to develop a more refined model than the mixed biosphere model presented in the last section and used in Chapter 2. The first reason is that the representation of the carbon fixed in bulky wood like stems is not very realistic in the mixed reservoir where every carbon input begins instantaneously to be decomposed. The second is that we needed a biosphere model allowing for seasonally variable NPP and decomposition fluxes. For simplicity of the explanations we do not consider seasonality until Appendix A.2.2.4.

A.2.2.1 Basic idea of the statistical model

Let us consider the cycling of carbon through the bulky wooden parts of a large amount of trees in a reservoir. The mass of one element of this reservoir representing carbon in the stem, big branches and roots of a single tree in a *statistically idealized* way varies in time according to Figure 26. After birth at time t_0 the carbon mass $m(t-t_0)$ of the element grows until time t_0+T_g to the maximal mass m_{max} , then the element stands without growth during an intermediate time until

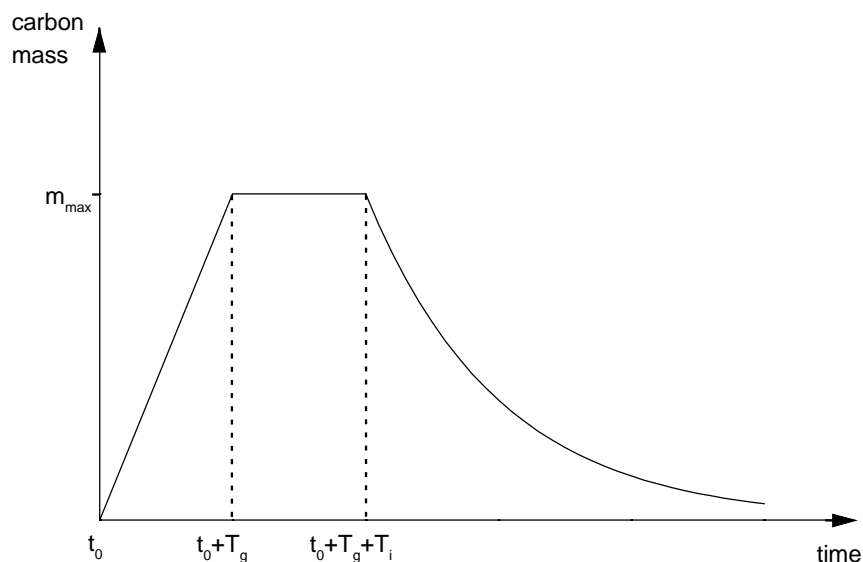


Figure 26 Time development of the carbon mass in a single idealized element of a statistical biosphere reservoir. The seasonality of growth and decomposition is not accounted for in this graph.

$t_0+T_g+T_i$ and is finally decomposed with an e-folding time τ_{dec} . The corresponding definition of $m(t-t_0)$ is:

$$m(t-t_0) = \begin{cases} \frac{m_{max}}{T_g} \cdot (t-t_0) & \text{if } 0 \leq t-t_0 \leq T_g \\ m_{max} & \text{if } T_g \leq t-t_0 \leq T_g+T_i \\ m_{max} \cdot \exp\left(\frac{t_0+T_g+T_i-t}{\tau_{dec}}\right) & \text{if } t-t_0 \geq T_g+T_i \end{cases} \quad (28)$$

A similar description can also account for a reservoir representing twigs and leaves, ground vegetation or any other subdivisions of the biosphere. We call *statistical biosphere* our model containing such kind of reservoirs.

A.2.2.2 Cycling of carbon (no seasonality)

The function $m(t-t_0)$ is subdivided to distinguish between carbon input and carbon output:

$$m(t-t_0) = m_{inp}(t-t_0) + m_{out}(t-t_0) \quad (29)$$

$$\text{with} \quad m_{inp}(t-t_0) = \begin{cases} m(t-t_0) & \text{if } \partial_t m(t-t_0) \geq 0 \\ m_{max} & \text{else} \end{cases}$$

$$m_{out}(t-t_0) = \begin{cases} m(t-t_0) - m_{max} & \text{if } \partial_t m(t-t_0) < 0 \\ 0 & \text{else} \end{cases}$$

In a statistical reservoir such idealized elements are born at time η with a birth rate $N(\eta)$ and the gross carbon input flux $F_{C_inp}(t)$ then is:

$$F_{C_inp}(t) = \int_{-\infty}^t N(\eta) \cdot \partial_t m_{inp}(t-\eta) d\eta$$

$$= \int_{t-T_g}^t N(\eta) \cdot \partial_t m_{inp}(t-\eta) d\eta$$

and if $N(t)=N_{cst}$ is constant:

$$= N_{cst} \cdot m_{max} := F_{C_inp_cst} \quad (30)$$

The gross carbon decomposition flux $F_{C_dec}(t)$ out of the reservoir is:

$$F_{C_dec}(t) = \int_{-\infty}^t N(\eta) \partial_t m_{out}(t-\eta) d\eta$$

and if $N(t)=N_{cst}$ is constant:

$$= -N_{cst} m_{max} := F_{C_dec_cst} \quad (31)$$

which just balances the gross carbon input flux when $N(t)=N_{cst}$ is constant.

The total mass of carbon in the reservoir is:

$$M(t) = \int_{-\infty}^t N(\eta) \cdot m(t-\eta) d\eta$$

and if $N(t)=N_{cst}$ is constant:

$$= N_{cst} \int_0^{\infty} m(\mu) d\mu = N_{cst} \cdot m_{max} \cdot \left(\frac{T_g}{2} + T_i + \tau_{dec} \right) := M_{cst} \quad (32)$$

where the variable transformation $\mu = (t-\eta)$ was used. To determine the residence time of carbon in the reservoir we consider that when decomposition begins, *all* parts of an element (e.g. stem, big branches and roots of a tree) are decomposed at the same rate defined by τ_{dec} . Therefore the output $\partial_t m_{out}(t-\eta)$ at time t from a single element born at time η has the residence time $(t-\eta-T_g/2)$ because the growth was constant between η and $\eta+T_g$. Thus the residence time for carbon in the entire reservoir assuming constant birth rate $N(t)=N_{cst}$ is:

$$\begin{aligned} T_{res} &= \frac{1}{-N_{cst} m_{max}} \int_{-\infty}^t (t-\eta - \frac{T_g}{2}) \cdot N_{cst} \cdot \partial_t m_{out}(t-\eta) d\eta \\ &= \frac{-\frac{T_g}{2} N_{cst}}{-N_{cst} \cdot m_{max}} \int_0^{\infty} \partial_{\mu} m_{out}(\mu) d\mu + \frac{1}{m_{max}} \int_0^{\infty} \mu \cdot \partial_{\mu} m_{out}(\mu) d\mu \\ &= \frac{-\frac{T_g}{2} + \frac{1}{m_{max}} \int_{T_g+T_i}^{\infty} \mu \cdot \left(\frac{-1}{\tau_{dec}} \cdot m_{max} \cdot \exp\left(\frac{T_g+T_i-\mu}{\tau_{dec}}\right) \right) d\mu}{1} \\ &= \frac{-\frac{T_g}{2} + \int_0^{\infty} (v+T_g+T_i) \cdot \frac{-1}{\tau_{dec}} \cdot \exp\left(-\frac{v}{\tau_{dec}}\right) dv}{1} \\ &= \frac{-\frac{T_g}{2} + T_g + T_i + \int_0^{\infty} v \cdot \partial_v \exp\left(-\frac{v}{\tau_{dec}}\right) dv}{1} \\ &= \frac{T_g}{2} + T_i + \tau_{dec} \end{aligned} \quad (33)$$

where the variable transformations $\mu=(t-\eta)$ and $v=\mu-(T_g+T_i)$ are used. Combining equations (32), (30) and (33) results in the equation:

$$M_{cst} = F_{C_inp_cst} \cdot T_{res} \quad (34)$$

which bears strong similarity with the equation (19) for a mixed biosphere reservoir.

The mean carbon age $T_{age_elt}(t-t_0)$ at time t in a single element of a statistical reservoir born at time t_0 is given through the function:

$$\begin{aligned}
\text{if } t-t_0 \leq T_g, \quad T_{age_elt}(t-t_0) &= \frac{1}{m_{inp}(t)} \int_{t_0}^t (t-\eta) \cdot \partial_{\eta} m_{inp}(\eta-t_0) d\eta \\
&= \frac{1}{\frac{m_{max}}{T_g}(t-t_0)} \int_0^{t-t_0} \mu \cdot \frac{m_{max}}{T_g} d\mu \\
&= \frac{t-t_0}{2} \\
\text{if } t-t_0 \geq T_g, \quad T_{age_elt}(t-t_0) &= (t-t_0) - \frac{T_g}{2}
\end{aligned} \tag{35}$$

where the variable transformation $\mu=(t-\eta)$ was used. The mean carbon age T_{age} in the entire reservoir is the mean of all reservoir element carbon ages according to the expression:

$$T_{age} = \frac{1}{M_{cst}} \int_{-\infty}^t T_{age_elt}(t-\eta) \cdot N_{cst} \cdot m(t-\eta) d\eta = \frac{N_{cst}}{M_{cst}} \int_0^{\infty} T_{age_elt}(\mu) \cdot m(\mu) d\mu \tag{36}$$

where the substitution $\mu=(t-\eta)$ was used. With the equation (28) for $m(t-t_0)$ and the equation (35) for $T_{res_elt}(t-t_0)$ the last equation becomes:

$$\begin{aligned}
T_{age} &= \frac{N_{cst}}{M_{cst}} \left(\int_0^{T_g} T_{age_elt}(\mu) \cdot m(\mu) d\mu + \int_{T_g}^{T_g+T_i} T_{age_elt}(\mu) \cdot m(\mu) d\mu + \int_{T_g+T_i}^{\infty} T_{age_elt}(\mu) \cdot m(\mu) d\mu \right) \\
&= \frac{N_{cst}}{M_{cst}} \left(\int_0^{T_g} \frac{\mu}{2} \cdot \frac{m_{max}}{T_g} \mu d\mu + \int_{T_g}^{T_g+T_i} \left(\mu - \frac{T_g}{2}\right) \cdot m_{max} d\mu + \int_{T_g+T_i}^{\infty} \left(\mu - \frac{T_g}{2}\right) \cdot \exp\left(-\frac{T_g+T_i-\mu}{\tau_{dec}}\right) d\mu \right) \\
&= \frac{N_{cst} m_{max}}{M_{cst}} \left(\left[\frac{T_g^2}{6} \right] + \left[-\frac{T_g}{2} T_i + \frac{(T_g+T_i)^2 - T_g^2}{2} \right] + \left[\tau_{dec} \left(\frac{T_g}{2} + T_i + \tau_{dec} \right) \right] \right)
\end{aligned} \tag{37}$$

Substituting M_{cst} according to equation (32) we finally obtain:

$$\begin{aligned}
T_{age} &= \frac{N_{cst} \cdot m_{max}}{N_{cst} \cdot m_{max} \cdot \left(\frac{T_g}{2} + T_i + \tau_{dec}\right)} \left(\frac{T_g^2}{6} + \frac{T_g T_i}{2} + \frac{T_i^2}{2} + \tau_{dec} \cdot \left(\frac{T_g}{2} + T_i + \tau_{dec}\right) \right) \\
&= \tau_{dec} + \frac{\frac{T_g^2}{6} + \frac{T_g T_i}{2} + \frac{T_i^2}{2}}{\frac{T_g}{2} + T_i + \tau_{dec}}
\end{aligned} \tag{38}$$

Note that in a statistical model reservoir the carbon age is generally different from the carbon residence time except if $T_g=T_i=0$.

A.2.2.3 Cycling of radiocarbon (no seasonality)

The total ^{14}C activity (e.g. in Bq) of a reservoir element born at time t_0 until the time $t_0+T_g+T_i$ when decomposition starts is the integral sum over all the inputs remaining in the reservoir of their initial activity corrected for decay. During decomposition only radioactive decay changes the *mean* activity (e.g. in Bq per kgC) so that we obtain following expression for the element's mean ^{14}C activity $a(t, t_0)$ (e.g. in Bq per kgC):

$$a(t_0, t) = \frac{1}{m_{inp}(t-t_0)} \left(\int_{t_0}^t \alpha A_{inp}(\xi) \cdot \exp(\lambda \cdot (\xi - t)) \partial_{\xi} m_{inp}(\xi - t_0) d\xi \right) \quad (39)$$

For a single element the mean activity $a(t_0+T_g+T_i, t_0)$ just when decomposition starts does not depend on the birth date t_0 if $A_{inp}(t)=A_{inp_cst}$ is constant:

$$\begin{aligned} a(t_0+T_g+T_i, t_0) &= \\ &= \frac{\alpha A_{inp_cst}}{m_{max}} \int_{t_0}^{t_0+T_g+T_i} \partial_{\xi} m_{inp}(\xi - t_0) \cdot \exp(\lambda \cdot (\xi - (t_0+T_g+T_i))) d\xi \\ &= \frac{\alpha A_{inp_cst}}{m_{max}} \exp(-\lambda T_i) \int_{t_0}^{t_0+T_g} \frac{m_{max}}{T_g} \exp(\lambda \cdot (\xi - (t_0+T_g))) d\xi \\ &= \frac{\alpha A_{inp_cst}}{T_g} \exp(-\lambda T_i) \frac{1 - \exp(-\lambda T_g)}{\lambda} \\ &:= a_{cst_Tg+Ti} \end{aligned} \quad (40)$$

The mean activity of an entire reservoir then becomes:

$$\begin{aligned} A_{res}(t) &= \frac{1}{M_{res}(t)} \int_{-\infty}^t N(\eta) \cdot m(t-\eta) \cdot a(t, \eta) d\eta \\ &= \frac{1}{M_{res}(t)} \int_{-\infty}^t \frac{N(\eta) \cdot m(t-\eta)}{m_{inp}(t-\eta)} \int_{\eta}^t \alpha A_{inp}(\xi) \cdot \exp(\lambda \cdot (\xi - t)) \partial_{\xi} m_{inp}(\xi - \eta) d\xi d\eta \end{aligned}$$

and if $N(t)=N_{cst}$ is constant:

$$\begin{aligned} &= \frac{1}{m_{max} T_{res}} \int_{-\infty}^t \frac{m(t-\eta)}{m_{inp}(t-\eta)} \int_{\eta}^t \alpha A_{inp}(\xi) \cdot \exp(\lambda \cdot (\xi - t)) \partial_{\xi} m_{inp}(\xi - \eta) d\xi d\eta \\ &= \frac{1}{m_{max} T_{res}} \int_{-\infty}^t \frac{m(t-\eta)}{m_{inp}(t-\eta)} \int_{\eta}^{\min(t, \eta+T_g)} \alpha A_{inp}(\xi) \cdot \exp(\lambda \cdot (\xi - t)) \cdot \frac{m_{max}}{T_g} d\xi d\eta \end{aligned}$$

$$= \frac{1}{T_{res} T_g} \int_{-\infty}^t \frac{m(t-\eta)}{m_{inp}(t-\eta)} \int_{\eta}^{\min(t, \eta+T_g)} \alpha A_{inp}(\xi) \cdot \exp(\lambda \cdot (\xi - t)) d\xi d\eta \quad (41)$$

Assuming that $A_{inp}(t) = A_{inp_cst}$ is constant at preindustrial equilibrium the reservoir activity is constant with the value A_{res_cst} :

$$\begin{aligned} A_{res} &= \frac{\alpha A_{inp_cst}}{T_{res} T_g} \int_{-\infty}^t \frac{m(t-\eta)}{m_i(t-\eta)} \int_{\eta}^{\min(t, \eta+T_g)} \exp(\lambda \cdot (\xi - t)) d\xi d\eta \\ &= \dots \\ &= \frac{\alpha \cdot A_{inp_cst}}{T_{res} T_g} \cdot \frac{1}{\lambda} \left(T_g - \frac{\exp(-\lambda T_i) \cdot (1 - \exp(-\lambda T_g))}{\lambda \cdot (1 + \lambda \cdot \tau_{dec})} \right) \\ &= \frac{1}{\lambda \cdot T_{res}} \left(\alpha A_{inp_cst} - \frac{a_{cst_Tg+Ti}}{1 + \lambda \tau_{dec}} \right) := A_{res_cst} \end{aligned} \quad (42)$$

Solving the last equation is not difficult but too long to be detailed here. If $T_i=0$ and T_g tends to zero the last equation becomes:

$$\lim_{\substack{T_g \rightarrow 0 \\ T_i=0}} A_{res_cst} = \frac{\alpha A_{inp_cst}}{1 + \lambda \tau_{dec}} \quad (43)$$

where we used equation (33) giving the equivalence $T_{res} = \tau_{dec}$ when $T_g=0$ and $T_i=0$. The last expression is similar to that obtained in the mixed biosphere case (equation (25)). The sense of equation (42) becomes clear when reformulating it:

$$\begin{aligned} A_{res_cst} &= \frac{1}{\lambda T_{res}} \left(\alpha A_{inp_cst} - \frac{a_{cst_Tg+Ti}}{1 + \lambda \tau_{dec}} \right) \\ &\quad \Downarrow \\ &= \frac{\left(\alpha A_{inp_cst} - \frac{a_{cst_Tg+Ti}}{1 + \lambda \tau_{dec}} \right)}{A_{res_cst}} = \lambda T_{res} \end{aligned} \quad (44)$$

The left hand term of the last equation is the difference between input activity and mean activity in the decomposable carbon fraction of a reservoir divided by the mean activity in the reservoir. The obtained ratio is equal to the ratio between carbon residence time and radioactive lifetime of ^{14}C .

The ^{14}C uptake flux $F_{14C_inp}(t)$ to the statistical reservoir is obtained from the carbon input:

$$F_{14C_inp}(t) = \alpha A_{inp}(t) \cdot F_{C_inp}(t)$$

$$= \alpha A_{inp}(t) \int_{-\infty}^t N(\eta) \cdot \partial_t m_{inp}(t-\eta) d\eta$$

and if $N(t)=N_{cst}$ is constant:

$$= \alpha A_{inp}(t) \cdot N_{cst} \cdot m_{max} \quad (45)$$

The ^{14}C output flux $F_{14C_dec}(t)$ due to carbon decomposition from the reservoir is:

$$\begin{aligned} F_{14C_dec}(t) &= \int_{-\infty}^t N(\eta) a(t,\eta) \partial_t m_{out}(t-\eta) d\eta \\ &= \int_{-\infty}^t N(\eta) \left[\frac{\int_{\eta}^t \alpha A_{inp}(\xi) \cdot \exp(\lambda \cdot (\xi-t)) \partial_{\xi} m_{inp}(\xi-\eta) d\xi}{m_{inp}(t-\eta)} \right] \cdot \partial_t m_{out}(t-\eta) d\eta \\ &= \int_{-\infty}^{t-(T_g+T_i)} N(\eta) \partial_t m_{out}(t-\eta) \left[\frac{\int_{\eta}^{\eta+T_g+T_i} \alpha A_{inp}(\xi) \cdot \exp(\lambda \cdot (\xi-t)) \partial_{\xi} m_{inp}(\xi-\eta) d\xi}{m_{max}} \right] d\eta \\ &= \int_{-\infty}^{t-(T_g+T_i)} N(\eta) \cdot \partial_t m_{out}(t-\eta) \cdot a(\eta+T_g+T_i, \eta) \cdot \exp(\lambda \cdot (\eta+T_g+T_i-t)) d\eta \end{aligned} \quad (46)$$

The integration in the last equation can be reduced to a finite interval by introducing an intermediate time step $t_0 \leq t$ where $F_{14C_dec}(t_0)$ is assumed to be known:

$$\begin{aligned} F_{14C_dec}(t) &= \\ &= \int_{-\infty}^{t_0-(T_g+T_i)} N(\eta) \partial_t m_{out}(t-t_0+t_0-\eta) \cdot a(\eta+T_g+T_i, \eta) \cdot \exp(\lambda \cdot (\eta+T_g+T_i-t_0+t_0-t)) d\eta \\ &+ \int_{t_0-(T_g+T_i)}^{t-(T_g+T_i)} N(\eta) \partial_t m_{out}(t-\eta) \cdot a(\eta+T_g+T_i, \eta) \cdot \exp(\lambda \cdot (\eta+T_g+T_i-t)) d\eta \\ &= F_{14C_dec}(t_0) \cdot \exp((t_0-t)(\lambda + \frac{1}{\tau_{dec}})) \\ &+ \int_{t_0-(T_g+T_i)}^{t-(T_g+T_i)} N(\eta) \partial_t m_{out}(t-\eta) \cdot a(\eta+T_g+T_i, \eta) \cdot \exp(\lambda \cdot (\eta+T_g+T_i-t)) d\eta \end{aligned} \quad (47)$$

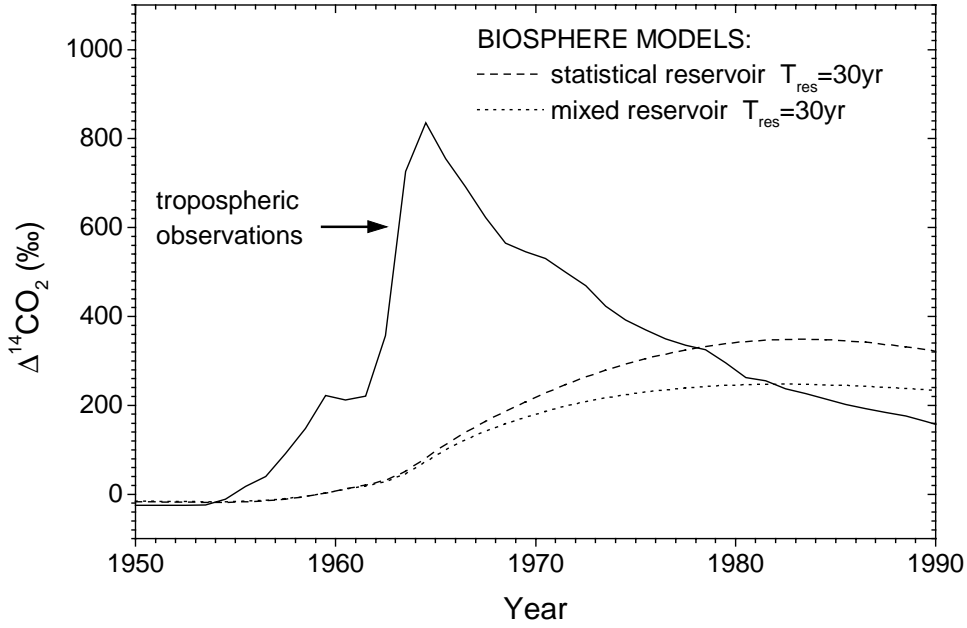


Figure 27 Comparison of the mean $\Delta^{14}\text{C}$ in a mixed biospheric reservoir with the mean ^{14}C in a statistical biospheric reservoir which has the same residence time for carbon. The settings for the statistical reservoir are $T_g=20$ yr, $T_i=10$ yr and $\tau_{dec}=10$ yr, which corresponds to a residence time of 30 yr. The statistical reservoir really sequesters the bomb radiocarbon before releasing it back to the atmosphere and, hence, has a higher mean ^{14}C activity than the mixed reservoir.

At preindustrial equilibrium where $N(t)=N_{cst}$ and $A_{inp}(t)=A_{inp_cst}$ are assumed to be constant, the radiocarbon decomposition flux $F_{^{14}\text{C}_{dec}}(t)$ becomes constant:

$$\begin{aligned}
 F_{^{14}\text{C}_{dec}}(t) &= N_{cst} \int_{-\infty}^{t-T_g-T_i} \partial_t m_{out}(t-\eta) \cdot a_{cst_Tg+Ti} \cdot \exp(\lambda \cdot (\eta + T_g + T_i - t)) d\eta \\
 &= -N_{cst} \cdot a_{cst_Tg+Ti} \int_{-\infty}^{t-T_g-T_i} \frac{-m_{max}}{\tau_{dec}} \exp\left(\frac{\eta + T_g + T_i - t}{\left(\lambda + \frac{1}{\tau_{dec}}\right)^{-1}}\right) d\eta \\
 &= -N_{cst} \cdot m_{max} \cdot a_{cst_Tg+Ti} \frac{1}{\lambda \tau_{dec} + 1} \\
 &= -N_{cst} m_{max} \frac{\alpha A_{inp_cst}}{T_g} \cdot \exp(-\lambda T_i) \cdot \frac{1 - \exp(-\lambda T_g)}{\lambda} \cdot \frac{1}{\lambda \tau_{dec} + 1} \\
 &:= F_{^{14}\text{C}_{dec_cst}} \tag{48}
 \end{aligned}$$

With the help of the preceding formalism the mean activity in a statistical biosphere reservoir can be computed. Figure 27 clearly demonstrates that the more realistic carbon sequestering of the statistical biosphere can lead to mean reservoir activities which sensibly differ from those of the mixed biosphere approach.

A.2.2.4 Seasonally variable cycling of carbon

Growth of plants and decomposition of organic matter occurs with a seasonally varying intensity mainly controlled by light intensity, temperature and precipitation. To account for seasonal variation of biospheric NPP and decomposition fluxes in the statistical reservoirs we must introduce a new definition of the now seasonally modulated carbon mass $m_S(t, t_0)$ at time t of an element born at time t_0 in a statistical reservoir:

$$m_S(t, t_0) = m_{inpS}(t, t_0) + m_{outS}(t, t_0) \quad (49)$$

These functions explicitly depend on both parameters (t, t_0) , not only on the difference $(t - t_0)$ as in the previous sections. The functions $m_{inpS}(t, t_0)$ and $m_{outS}(t)$ are defined as follows:

$$\partial_t m_{inpS}(t, t_0) = \begin{cases} \frac{m_{max}}{T_g} \cdot \varphi_{inpS}(t) & \text{if } 0 \leq t \leq T_{gS}(t_0) \\ 0 & \text{else} \end{cases}$$

$$\partial_t m_{outS}(t, t_0) = \begin{cases} \frac{-m_{max}}{\tau_{dec}} \varphi_{outS}(t) \cdot \exp\left(\frac{t_0 + T_{gS}(t_0) + T_{iS}(t_0) - t}{\tau_{dec}}\right) & \text{if } t \geq t_0 + T_{gS}(t_0) + T_{iS}(t_0) \\ 0 & \text{else} \end{cases} \quad (50)$$

$\varphi_{inpS}(t)$ and $\varphi_{outS}(t)$ are seasonally variable functions with a periodicity of 1 yr and yearly mean value of 1, m_{max} is the maximal carbon mass of an element, $T_{gS}(t_0)$ is the seasonally variable time needed by an element born at t_0 to grow up to m_{max} , T_g is the yearly mean of $T_{gS}(t)$. To simplify our seasonal approach we will always consider that:

$$T_{g+iS} := T_{gS}(t) + T_{iS}(t) \quad \text{is a positive constant} \quad (51)$$

T_{g+iS} is the time interval between birth and the start of decomposition of an element. Thus $T_{iS}(t)$ is the time during which the element is neither growing nor decomposed. $\varphi_{inpS}(t)$ reflects the seasonally variable impulse of light, temperature and precipitations on the growth of plants. $\varphi_{outS}(t)$ reflects the corresponding effect on decomposition. The seasonally variable carbon input flux $F_{C_inpS}(t)$ to a reservoir is:

$$F_{C_inpS}(t) = \int_{-\infty}^t N(\eta) \cdot \partial_t m_{inpS}(t, \eta) d\eta$$

$$= \int_{t_{min}(t)}^t N(\eta) \cdot \frac{m_{max}}{T_g} \cdot \varphi_{inpS}(t) d\eta \quad (52)$$

where $t_{min}(t)$ is the smallest value of η for which t lies in the interval $[\eta, \eta + T_{gS}(\eta)]$. Equation (52) allows to explain how we determined the seasonally variable birth rate $N(t)$ and the function $\varphi_{inpS}(t)$ for our statistical reservoirs in contact to the atmosphere. We assumed that both the element growth rate $\partial_t m_{inpS}(t, \eta)$ and the element birth rate $N(\eta)$ have the same seasonality as the NPP. The function $\varphi_{inpS}(t)$ is set proportional to the prescribed NPP flux entering the reservoir. We use data fields of the TM2 model [Heimann and Keeling, 1989] to prescribe the NPP flux (see Appendix A.2.2.6). The proportionality factor is set to obtain a yearly mean $\varphi_{inpS}(t)$ equal to 1. The values for $N(t)$ are obtained from:

$$N(t) = \beta \varphi_{inpS}(t) \quad (53)$$

where β is set to obtain the same yearly mean value for $F_{C_inpS}(t)$ using equation (52) as for the NPP flux prescribed from the TM2 fields. When these values for $N(t)$ and $\partial_t m_{inpS}(t, \eta)$ are used in equation (52) the values obtained for $F_{C_inpS}(t)$ in our standard model agree very well with the NPP fluxes prescribed from the TM2. However our simple assumption that both the element growth rate and the element birth rate have the same seasonality as the NPP may not be realistic for all types of biospheric reservoirs.

The seasonally variable decomposition flux $F_{C_outS}(t)$ out of a reservoir is:

$$\begin{aligned} F_{C_outS}(t) &= \int_{-\infty}^{t-T_{g+iS}} N(\eta) \cdot \partial_t m_{outS}(t, \eta) d\eta \\ &= \int_{-\infty}^{t-T_{g+iS}} N(\eta) \cdot \frac{-m_{max}}{\tau_{dec}} \varphi_{outS}(t) \cdot \exp\left(\frac{\eta + T_{g+iS} - t}{\tau_{dec}}\right) d\eta \\ &\Downarrow \\ \varphi_{outS}(t) &= \frac{F_{C_outS}(t)}{\int_{-\infty}^{t-T_{g+iS}} N(\eta) \cdot \frac{-m_{max}}{\tau_{dec}} \cdot \exp\left(\frac{\eta + T_{g+iS} - t}{\tau_{dec}}\right) d\eta} \end{aligned} \quad (54)$$

This allows us to determine the values for $\varphi_{outS}(t)$ replacing $F_{C_outS}(t)$ by the prescribed decomposition flux fields of the TM2 model.

A.2.2.5 Seasonally variable cycling of radiocarbon

Once the birth rate $N(t)$ and the carbon input flux $\partial_t m_{inpS}(t, \eta)$ are known, the radiocarbon input flux $F_{14C_inpS}(t)$ to the statistical reservoir is simply determined from:

$$F_{14C_inpS}(t) = \int_{t_{min}(t)}^t N(\eta) \cdot \alpha A_{inp}(\eta) \cdot \exp(\lambda \cdot (\eta - t)) \cdot \partial_t m_{inpS}(t, \eta) d\eta \quad (55)$$

which can be easily solved numerically. The definition for $t_{min}(t)$ is the same as in equation (52).

The radiocarbon output flux from the reservoir is less simple to determine because it involves integration over an infinite time interval. First we define the element's mean ^{14}C activity $a_S(t, t_0)$ of one element (e.g. in Bq per kgC) similarly to equation (39):

$$a_S(t, t_0) = \frac{1}{m_{inpS}(t, t_0)} \int_{t_0}^t \alpha A_{inp}(\xi) \cdot \exp(\lambda \cdot (\xi - t)) \cdot \partial_\xi m_{inpS}(\xi, t_0) d\xi \quad (56)$$

Then the radiocarbon flux $F_{14C_decS}(t)$ from decomposition in the reservoir can be reformulated as:

$$\begin{aligned}
F_{14C_decS}(t) &= \int_{-\infty}^{t-T_{g+iS}} N(\eta) \cdot \partial_t m_{outS}(t, \eta) \cdot a_S(\eta + T_{g+iS}, \eta) \cdot \exp(\lambda \cdot (\eta + T_{g+iS} - t)) d\eta \\
&= \int_{-\infty}^{t-T_{g+iS}-n \cdot T_{Iyear}} N(\eta) \cdot \partial_t m_{outS}(t, \eta) \cdot a_S(\eta + T_{g+iS}, \eta) \cdot \exp(\lambda \cdot (\eta + T_{g+iS} - t)) d\eta \\
&\quad + \int_{T-T_{g+iS}-n \cdot T_{Iyear}}^{t-T_{g+iS}} N(\eta) \cdot \partial_t m_{outS}(t, \eta) \cdot a_S(\eta + T_{g+iS}, \eta) \cdot \exp(\lambda \cdot (\eta + T_{g+iS} - t)) d\eta \\
&= F_{14C_decS}(t - n \cdot T_{Iyear}) \cdot \exp\left(-n T_{Iyear} \left(\lambda + \frac{1}{\tau_{dec}}\right)\right) \\
&\quad + \int_{T-T_{g+iS}-n \cdot T_{Iyear}}^{t-T_{g+iS}} N(\eta) \cdot \partial_t m_{outS}(t, \eta) \cdot a_S(\eta + T_{g+iS}, \eta) \cdot \exp(\lambda \cdot (\eta + T_{g+iS} - t)) d\eta \quad (57)
\end{aligned}$$

where $n \cdot T_{Iyear} = n$ is an integer number of years. This redundant notation is used to emphasize that this formula is only valid for a time step of n years because the periodicity of $\partial_t m_{outS}(t, \eta)$ is one year.

A.2.2.6 NPP, decomposition, fertilization, destruction and the TM2 data fields

Four components of gross carbon exchange between the statistical biosphere and the model atmosphere are considered so that the net carbon exchange is:

$$F_{C_bio_net} = F_{C_npp} + F_{C_dec} + F_{C_des} + F_{C_fer} \quad (58)$$

Two components are adopted from the TM2 fields [Heimann and Keeling, 1989] (here we consider that *a positive flux describes a positive uptake by the biosphere*):

- The natural seasonal uptake component F_{C_npp} is always positive and describes the net primary productivity of the land biosphere due to photosynthesis. It was determined from satellite data using a model for remote sensing of plant growth by Kumar and Monteith [1981]. In the TM2 data fields this component amounts to a yearly mean uptake of 56 GtC yr⁻¹ but in our model we multiply this distribution by a constant value in order to amount 60 GtC yr⁻¹.
- The natural seasonal component F_{C_dec} is always negative and describes the release of carbon back to the atmosphere through decomposition of organic matter in litter and soils. It was determined using ground level temperature data to account for the seasonal variation of soil temperature and a fitting procedure to best match atmospheric CO₂ observations. We scale the distribution of the TM2 data fields to exactly balance the yearly mean NPP of 60 GtC yr⁻¹ mean in each box of our model.

The two other components are not seasonal and account for net global fluxes:

- The yearly mean anthropogenic destruction component F_{C_des} is always negative and describes the net release of biospheric carbon to the atmosphere due to land use change [Houghton and Hackler, 1995]. This destruction flux is assumed to make up between 1.5 and 2 GtC yr⁻¹ during the 1980s.

- The yearly mean fertilization uptake flux $F_{C_{fer}}$ is always positive. It accounts for a still hypothetical worldwide excess of plant growth stimulated by the increased atmospheric CO₂ level. In our study this net yearly biospheric uptake is obtained similarly to the net yearly oceanic uptake (see Appendix A.1.1). First we determine the amount of the total yearly anthropogenic CO₂ emissions which has to be removed from the atmosphere to preserve the globally observed tropospheric CO₂ increase. Then 45% of this uptake are attributed to the biospheric fertilization sink. The mean strength of this sink lies between 1.5 and 2 GtC yr⁻¹ during the 1980s.

A.2.2.7 Numerical realization of the statistical biosphere model

Equations (55), (56) and (57) are used together with atmospheric activity values determined from $\Delta^{14}\text{CO}_2$ observations [Stuiver and Quay, 1981; Tans, 1981; Manning et al., 1990; Levin et al., 1992] using equation (63) from the Appendix A.4.2. Then $F_{14C_{impS}}(t)$ and $F_{14C_{decS}}(t)$ can be computed step by step ongoing from preindustrial equilibrium assumed for 1750. To determine $F_{14C_{decS}}(t)$ using equation (57), initial values for 1750 must be obtained. As the model works with a monthly time resolution, a set of 12 initial values $\{F_{14C_{decS}}(1750+i/12), i=1,12\}$ must be known. This set is obtained by first computing:

$$\omega(t_i) = \int_{t_i - T_{g+iS} - T_{1year}}^{t_i - T_{g+iS}} N(\eta) \cdot a_S(\eta + T_{g+iS}, \eta) \cdot \frac{-m_{max}}{\tau_{dec}} \cdot \varphi(t_i) \cdot \exp\left(\left(\lambda + \frac{1}{\tau_{dec}}\right)(\eta + T_{g+iS} - t_i)\right) d\eta \quad (59)$$

All functions of the integrand in the last equation except the exponential have a periodicity of one year. Thus we obtain:

$$\begin{aligned} F_{14C_{decS}}(t_i) &= \int_{-\infty}^{t_i - T_{g+iS}} N(\eta) \cdot a_S(\eta + T_{g+iS}, \eta) \cdot \frac{-m_{max}}{\tau_{dec}} \cdot \varphi(t_i) \cdot \exp\left(\left(\lambda + \frac{1}{\tau_{dec}}\right)(\eta + T_{g+iS} - t_i)\right) d\eta \\ &= \omega(t_i) \cdot \sum_{i=0}^{\infty} \exp\left(-\left(\lambda + \frac{1}{\tau_{dec}}\right)^i\right) \\ &= \frac{\omega(t_i)}{1 - \exp\left(-\left(\lambda + \frac{1}{\tau_{dec}}\right)\right)} \end{aligned} \quad (60)$$

A.2.2.8 Statistical biosphere settings

The biosphere model used in Chapter 3 computes carbon isotope exchange fluxes to each tropospheric box of the atmospheric 14-box model which subdivides the troposphere into four latitudinal belts at 0° and ±30°. For each of these latitudinal belts the biosphere is subdivided into four reservoirs. The first with a carbon residence time T_{res} of a few years accounts for fast cycling organic matter like leaves, grasses, twigs and fine roots. The second with T_{res} of about a decade accounts for perennial ground vegetation. The third reservoir with T_{res} of several decades accounts for bulky wooden stems, branches and roots. These three reservoir are computed as statistical reservoirs. Finally a fourth mixed reservoir with a residence time of several centuries accounts for the soil organic matter resistant to decomposition. The soil reservoir takes its input equally from the first three reservoirs. Hence our statistical biosphere model amounts 16 reservoirs cycling carbon isotopes at preindustrial equilibrium according to Table 4. Note that

we did not yet account for meridional variations of the residence time of carbon in the reservoirs of the statistical biosphere. Within a latitudinal belt a constant fraction of the seasonally variable NPP prescribed by the TM2 fields is attributed to each of the three biospheric reservoirs assimilating carbon through photosynthesis. The same constant fraction of the corresponding carbon decomposition TM2 fields is used to prescribe the carbon release from each of these reservoirs at preindustrial equilibrium.

reservoir name	latitude (θ)	T_g yr	T_i yr	τ_{dec} yr	NPP frac	NPP GtC/yr	Mass GtC
leaves	$+30^\circ \leq \theta$	1	1	1	0.35	7.11	17.79
	$0^\circ \leq \theta \leq +30^\circ$	1	1	1	0.35	6.24	15.61
	$-30^\circ \leq \theta \leq 0^\circ$	1	1	1	0.35	7.11	17.77
	$-90^\circ \leq \theta \leq -30^\circ$	1	1	1	0.35	0.53	1.33
leaves total:						21.00	52.5
perennial vegetation	$+30^\circ \leq \theta$	9	1	1	0.35	7.11	46.24
	$0^\circ \leq \theta \leq +30^\circ$	9	1	1	0.35	6.24	40.58
	$-30^\circ \leq \theta \leq 0^\circ$	9	1	1	0.35	7.11	46.21
	$-90^\circ \leq \theta \leq -30^\circ$	9	1	1	0.35	0.53	3.46
perennial total:						21.00	136.5
wood	$+30^\circ \leq \theta$	44	1	20	0.30	6.10	262.22
	$0^\circ \leq \theta \leq +30^\circ$	44	1	20	0.30	5.35	230.12
	$-30^\circ \leq \theta \leq 0^\circ$	44	1	20	0.30	6.09	262.02
	$-90^\circ \leq \theta \leq -30^\circ$	44	1	20	0.30	0.46	19.65
wood total:						18.00	774.01
soil	$+30^\circ \leq \theta$	-	-	600	-	*1.47	883.75
	$0^\circ \leq \theta \leq +30^\circ$	-	-	600	-	*0.26	153.68
	$-30^\circ \leq \theta \leq 0^\circ$	-	-	600	-	*0.19	114.00
	$-90^\circ \leq \theta \leq -30^\circ$	-	-	600	-	*0.14	85.56
soil total:						*2.06	1236.99
TOTAL	(without *)					60.00	2200.00

Table 4 Main parameters for the statistical biosphere model used in chapter three. T_g is the mean time during which a reservoir element grows, T_i is the mean time during which a reservoir element stands without growing, τ_{dec} is the e-folding time for the element decomposition after death. More explanations on these quantities are found in the sections describing the seasonal statistical biosphere. $NPP\ frac$ is the fraction of the NPP uptake in the latitudinal belt which enters the corresponding reservoir. NPP is the flux of net primary productivity into the reservoir at preindustrial equilibrium. For the soil reservoir the values marked with a star (*) indicate that not the NPP is reported but the yearly gross uptake of carbon from the other reservoirs into the soil reservoir. $Mass$ is the total carbon mass in the reservoir at preindustrial equilibrium. The tabled values correspond to present day literature [Goudriaan, 1992; Post III, 1993] which, however, shows large uncertainties. The terms *leaves*, *perennial vegetation*, *wood* and *soil* are used as names and do not exhaustively describe the contents of the reservoirs.

A.3 Complements on the 14-box atmosphere model

The atmospheric model with 14 boxes is subdivided into 4 tropospheric and 10 stratospheric boxes as described in Figure 13. This structure is not arbitrary:

- The subdivision into latitudinal ring belts reflects the fast longitudinal mixing of air masses around the Earth completed within one month.
- The subdivision at the Equator accounts for the Inter Tropical Convergence Zone (ITCZ) acting as resistance for interhemispheric air mass exchange (see section 1.6).
- The subdivisions at $\pm 30^\circ$ account for the extension of the Hadley Cell circulation.
- The vertical extension of the tropospheric boxes accounts for the strong convective mixing of air up to the tropopause. The extension also reflects the mean location of the tropopause which is lower in mid to high latitudes than between the Tropics.
- The stratospheric subdivision adopted from Telegadas [Telegadas, 1971] revealed to satisfactorily reproduce the residence time of air with respect to bomb ^{14}C injections.

We mentioned in Chapter 3 that the meridional air mass exchange in the 14-box model was determined to match *ground level SF₆ observations*. As SF₆ is emitted at ground level the observations tend to be higher than corresponding tropospheric means. Therefore we determined the meridional transport in our 14-box model to match tropospheric means of the 2D-HD model running SF₆ as presented in Chapter 1. However Figure 28 demonstrates that we could also have determined the 14-box model transport by direct comparison with background station observations.

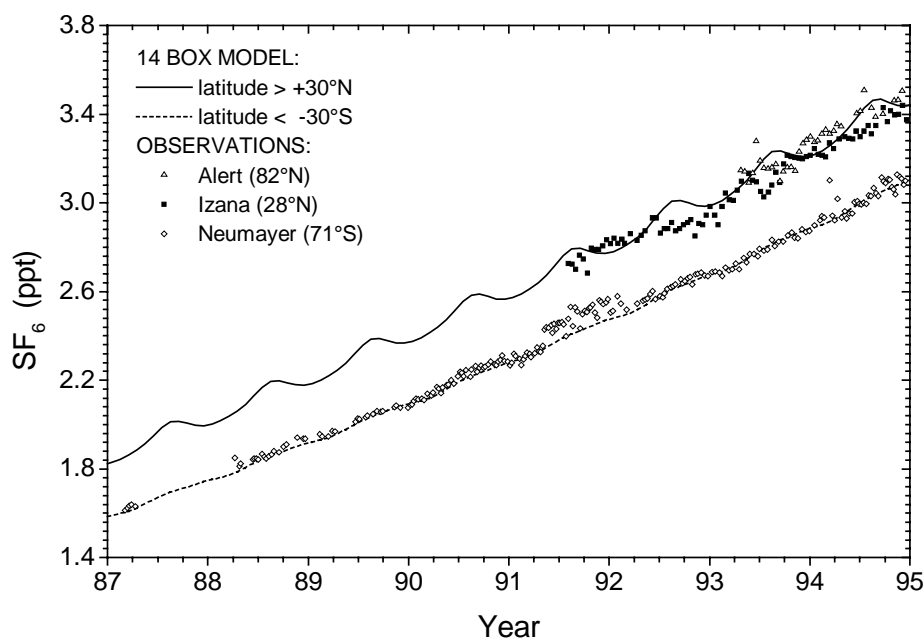


Figure 28 SF₆ concentrations estimated for the northern (latitude $> +30^\circ$) and the southern (latitude $< -30^\circ$) troposphere using the 14-box atmosphere model are compared with observations (individual data points) at corresponding sites. When compared with Figure 6 the 14-box model reveals to predict a much stronger SF₆ seasonality north of 30° than the 2D-HD model.

A.4 Definitions and equations concerning radiocarbon

A.4.1 Definition of $\delta^{13}\text{C}$

$\delta^{13}\text{C}$ of a carbon sample in permil is defined as:

$$\delta^{13}\text{C}_{\text{sample}} = \left(\frac{R_{\text{sample}}}{R_{\text{std}}} - 1 \right) \cdot 1000 \quad (61)$$

where R_{sample} denotes the $^{13}\text{C}/^{12}\text{C}$ atom ratio of the sample and $R_{\text{std}}=0.0112372$ is the atom ratio of the PDB standard [Craig, 1957]. $\delta^{13}\text{C}=-25\text{‰}$ is a typical mean value for carbon in plants. The mean $\delta^{13}\text{C}$ in atmospheric CO_2 was about -6.5‰ in 1800 [Neftel et al., 1985; Friedli et al., 1986] and decreased to about -8‰ in 1990. This decline reflects the emissions of anthropogenic fossil fuel with $\delta^{13}\text{C} \approx -26\text{‰}$ [Andres et al., 1996].

A.4.2 Definition of $\Delta^{14}\text{C}$

$\Delta^{14}\text{C}$ of a carbon sample in permil is defined as:

$$\Delta^{14}\text{C}_{\text{sample}} = \frac{A_{\text{sample}}}{A_{\text{std}}} \cdot \left(1 - 2 \cdot \frac{(\delta^{13}\text{C}_{\text{sample}} + 25)}{1000} \right) \cdot 1000 - 1000 \quad (62)$$

where A_{sample} is the activity of the sample. $A_{\text{std}}=226\text{ Bq per kgC}=13.56\text{ dpm per gC}=5.902 \cdot 10^{25}$ atoms ^{14}C per GtC = $1.177 \cdot 10^{12}$ atoms ^{14}C per atom C is 95% of the NBS oxalic acid activity corrected for decay [Karlén et al., 1968; Stuiver and Polach, 1977] and $\delta^{13}\text{C}_{\text{sample}}$ is expressed in permil. The very small ratio of $^{14}\text{C}/\text{C}$ allows in most cases to neglect the radiocarbon fraction in expressions involving total carbon, i.e to replace $\text{C}=(^{12}\text{C}+^{13}\text{C}+^{14}\text{C})$ by $\text{C}=(^{12}\text{C}+^{13}\text{C})$.

The activity of a carbon sample in units of the standard activity A_{std} can be determined from its $\Delta^{14}\text{C}$ and $\delta^{13}\text{C}$ expressed in permil using the inverse equation:

$$A_{\text{sample}} = \frac{(\Delta^{14}\text{C}_{\text{sample}} + 1000)}{1000} \cdot A_{\text{std}} \cdot \left(1 - 2 \cdot \left(\delta^{13}\text{C}_{\text{sample}} + \frac{25}{1000} \right) \right)^{-1} \quad (63)$$

A.4.3 Isotopic fractionation terminology

The isotopic fractionation for ^{13}C is described by $R'=\alpha_{13\text{C}} \cdot R$ where R' is the $^{13}\text{C}/^{12}\text{C}$ ratio after fractionation of a carbon sample with initial ratio R . As long as $R/R_{\text{std}} \approx 1$ the fractionation $\alpha_{13\text{C}}$ can be translated to a shift $\epsilon_{13\text{C}} = (\alpha_{13\text{C}} - 1) \cdot 1000$ in $\delta^{13}\text{C}$:

$$\begin{aligned} \delta^{13}\text{C}' &= \left(\frac{R'}{R_{\text{std}}} - 1 \right) \cdot 1000 = \left(\frac{\alpha_{13\text{C}} R}{R_{\text{std}}} - 1 \right) \cdot 1000 = \delta^{13}\text{C} + 1000 \cdot (\alpha_{13\text{C}} - 1) \cdot \frac{R}{R_{\text{std}}} \\ &= \delta^{13}\text{C} + \epsilon_{13\text{C}} \cdot \frac{R}{R_{\text{std}}} \\ &\approx \delta^{13}\text{C} + \epsilon_{13\text{C}} \end{aligned} \quad (64)$$

The fractionation for ^{14}C is similarly described by $A'=\alpha_{14\text{C}} \cdot A$ where A' is the activity after

fractionation of the carbon sample with initial activity A . The discrimination factor α_{14C} can be approximated as [Mook, 1994]:

$$\alpha_{14C} \approx (\alpha_{13C})^2 \quad (65)$$

and this results in:

$$\begin{aligned} \varepsilon_{14C} &= (\alpha_{14C} - 1) \\ &\approx ((\alpha_{13C})^2 - 1) \\ &= ((1 + \varepsilon_{13C})^2 - 1) \\ &\approx 2 \cdot \varepsilon_{13C} \end{aligned} \quad (66)$$

Note that the fractionation factor α_{13C} describes a variation in the $^{13}\text{C}/^{12}\text{C}$ ratio so that $\alpha_{14C} = (\alpha_{13C})^2$ describes a variation in the $^{14}\text{C}/^{12}\text{C}$ ratio and not in the $^{14}\text{C}/(^{12}\text{C} + ^{13}\text{C})$ ratio in which the ^{14}C activities are usually expressed. To be more exact the $^{14}\text{C}/(^{12}\text{C} + ^{13}\text{C})$ ratio after fractionation should be expressed as:

$$\begin{aligned} \left. \frac{^{14}\text{C}}{^{12}\text{C} + ^{13}\text{C}} \right)_{frac} &= \frac{\left(\alpha_{14C} \frac{^{14}\text{C}}{^{12}\text{C}} \right)^{12}\text{C}}{^{12}\text{C} \cdot \left(1 + \alpha_{13C} \frac{^{13}\text{C}}{^{12}\text{C}} \right)} \\ &= \alpha_{14C} \frac{^{12}\text{C} + ^{13}\text{C}}{^{12}\text{C} + \alpha_{13C} \cdot ^{13}\text{C}} \cdot \frac{^{14}\text{C}}{^{12}\text{C} + ^{13}\text{C}} \\ &= \alpha_{14C}^* \cdot \frac{^{14}\text{C}}{^{12}\text{C} + ^{13}\text{C}} \end{aligned} \quad (67)$$

However in all oceanic and biospheric fractionation processes α_{14C} is very near to one. The ratio $\alpha_{14C}^*/\alpha_{14C}$ is largest and equals 1.000181 during biospheric assimilation where $\alpha_{14C_ab} = 0.9819$. This leads to a difference in ^{14}C activity of about 0.2‰ which can be neglected and we do not distinguish between α_{14C}^* and α_{14C} in the present study.

A.4.4 Interannual variation of ocean surface $\Delta^{14}\text{C}$

The interannual variation of $\Delta^{14}\text{C}$ in the mixed layer of the ocean north of 60°S is determined basing on a crude model. We represent the mixed layer north of 60°S as a box exchanging radiocarbon with a well mixed atmosphere and with a well mixed deeper ocean according to the simple equilibration equation:

$$\frac{d}{dt} D_{oce_surf}(t) = \frac{(D_{atm}(t) - D_{oce_surf}(t))}{\tau_{sa}} + \frac{(D_{oce_deep}(t) - D_{oce_surf}(t))}{\tau_{sd}} \quad (68)$$

Here D_{oce_surf} is the $\Delta^{14}\text{C}$ of the mixed layer, D_{atm} is the $\Delta^{14}\text{C}$ of the atmosphere, D_{oce_deep} is the $\Delta^{14}\text{C}$ of the deeper ocean, τ_{sa} is the turnover time of ^{14}C in the mixed surface layer with respect to the atmosphere, τ_{sd} is the turnover time of ^{14}C in the mixed surface layer with respect to the deeper ocean. This equation partly accounts for fractionation effects. It is a differential equation

of the Bernoulli type for D_{oce_surf} :

$$\frac{d}{dt} D_{oce_surf}(t) + \frac{D_{oce_surf}(t)}{\tau^*} = \frac{D_{atm}(t)}{\tau_{sa}} + \frac{D_{oce_deep}(t)}{\tau_{sd}} \quad (69)$$

where $\tau^* = (1/\tau_{sa} + 1/\tau_{sd})^{-1}$. A solution is found by multiplying all terms with $\exp((t-t_0)/\tau^*)$ so that the equation can be written as:

$$\frac{d}{dt} \left(D_{oce_surf}(t) \cdot \exp\left(\frac{t-t_0}{\tau^*}\right) \right) = \left(\frac{D_{atm}(t)}{\tau_{sa}} + \frac{D_{oce_deep_equil}}{\tau_{sd}} \right) \cdot \exp\left(\frac{t-t_0}{\tau^*}\right) \quad (70)$$

Here t_0 is the time of preindustrial equilibrium, and we considered that the $\Delta^{14}\text{C}$ in the deeper ocean has the constant value $D_{oce_deep_equil}$. After integration, the equation can be written as:

$$D_{oce_surf}(t) = D_{oce_surf}(t_0) \cdot \exp\left(\frac{-(t-t_0)}{\tau^*}\right) + \int_{t_0}^t \left(\frac{D_{atm}(\xi)}{\tau_{sa}} + \frac{D_{oce_deep_equil}}{\tau_{sd}} \right) \cdot \exp\left(\frac{\xi-t}{\tau^*}\right) d\xi \quad (71)$$

If we define:

$$\Delta D(t) := D_{oce_surf}(t) - D_{oce_surf}(t_0) \quad (72)$$

and use the equilibrium form of equation (68):

$$\frac{D_{atm}(t_0) - D_{oce_surf}(t_0)}{\tau_{sa}} = - \frac{D_{oce_deep_equil} - D_{oce_surf}(t_0)}{\tau_{sd}} \quad (73)$$

we obtain:

$$\begin{aligned} \Delta D(t) &= D_{oce_surf}(t_0) \left[\exp\left(\frac{-(t-t_0)}{\tau^*}\right) - 1 \right] + \int_{t_0}^t \left(\frac{D_{atm}(\xi)}{\tau_{sa}} + \frac{D_{oce_deep_equil}}{\tau_{sd}} \right) \cdot \exp\left(\frac{\xi-t}{\tau^*}\right) d\xi \\ &= \int_{t_0}^t \left(\frac{D_{atm}(\xi)}{\tau_{sa}} + \frac{D_{oce_deep_equil}}{\tau_{sd}} - \frac{D_{oce_surf}(t_0)}{\tau^*} \right) \cdot \exp\left(\frac{\xi-t}{\tau^*}\right) d\xi \\ &= \int_{t_0}^t \left(\frac{D_{atm}(\xi) - D_{atm}(t_0)}{\tau_{sa}} \right) \cdot \exp\left(\frac{\xi-t}{\tau^*}\right) d\xi \end{aligned} \quad (74)$$

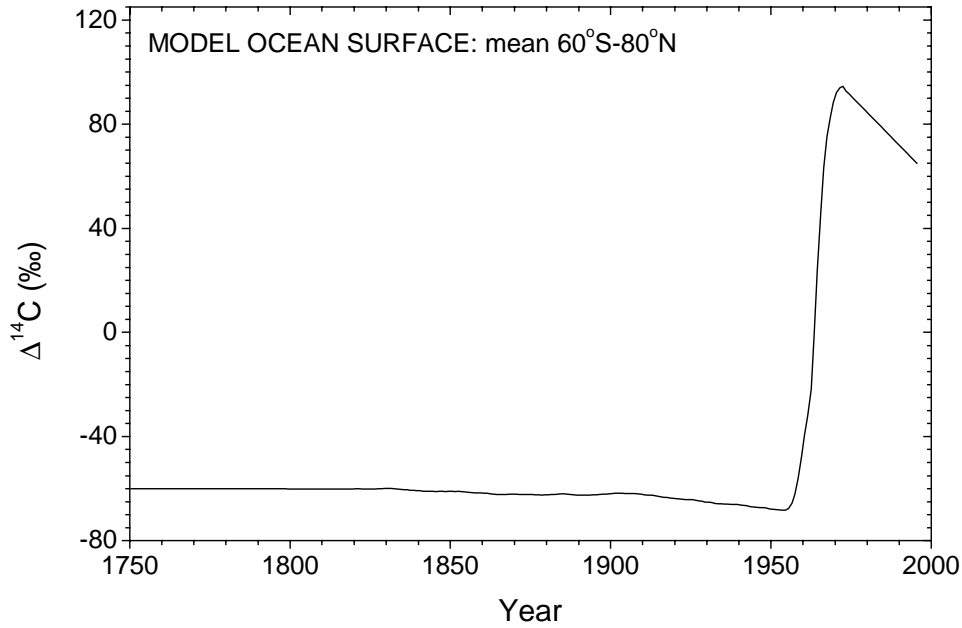


Figure 29 Function describing the mean $\Delta^{14}\text{C}$ north of 60°S in the model ocean surface. The function is obtained using atmospheric $^{14}\text{CO}_2$ observations together with a simple equation for the ocean surface (see Appendix A.4.4). We use this function to determine the long-term time variation of ocean surface $\Delta^{14}\text{C}$ between 1750 and 1995 in agreement with $\Delta^{14}\text{C}$ activities from ocean surface waters (Figure 21) and from corals (Figure 22).

We used mean tropospheric observations [*Stuiver and Quay*, 1981; *Tans*, 1981; *Manning et al.*, 1990; *Levin et al.*, 1992] for $D_{\text{atm}}(t)$, $\tau_{\text{sa}}=20$ yr, $\tau_{\text{sd}}=9$ yr and $D_{\text{oce_surf}}(t_0)=-60\text{‰}$ to compute from equation (74) the function shown in Figure 29 until 1973. After that date, a linearly decreasing function amounting $\Delta^{14}\text{C}=65\text{‰}$ in 1995 was used in order to match the observed meridional profile for 1988 (see Figure 21).

REFERENCES

- Andres, B., G. Marland, and S. Bischof, Global and Latitudinal Estimates of $\delta^{13}\text{C}$ from Fossil-Fuel Consumption and Cement Manufacture (DB-1013), *CDIAC Communications* (22), 9-10, 1996.
- Appenzeller, C., J.R. Holton, and K.H. Rosenlof, Seasonal variation of mass transport across the tropopause, *Journal of Geophysical Research*, 101 (D10), 15071-15078, 1996.
- Bolin, B., and H. Rodhe, A note on the concepts of age distribution and transit time in natural reservoirs, *Tellus*, 25, 58-62, 1973.
- Bonka, H., Produktion und Freisetzung von Tritium und Kohlenstoff-14 durch Kernwaffenversuche, Testexplosionen und kerntechnische Anlagen, einschliesslich Wiederaufarbeitungsanlagen, in *Strahlenschutzprobleme im Zusammenhang mit der Verwendung von Tritium und Kohlenstoff-14 und ihren Verbindungen*, edited by F.E. Stieve, and G. Kirstner, pp. 17-26, Dietrich Reimer Verlag, Berlin, 1980.
- Boutin, J., and J. Etcheto, Long term variability of the air-sea CO_2 exchange coefficient; consequences for the CO_2 fluxes in the equatorial Pacific ocean, *submitted to Global Biogeochemical Cycles*, 1996.
- Broecker, W.S., and T.-H. Peng, Stratospheric contribution to the global bomb radiocarbon inventory: Model versus observation, *Global Biogeochemical Cycles*, 8 (3), 377-384, 1994.
- Broecker, W.S., T.-H. Peng, and R. Engh, Modeling the carbon system, *Radiocarbon*, 22, 565-598, 1980.
- Broecker, W.S., T.-H. Peng, G. Östlund, and M. Stuiver, The distribution of bomb radiocarbon in the ocean, *Journal of Geophysical Research*, 90, 6953-6970, 1985.
- Broecker, W.S., S. Sutherland, W. Smethie, T.-H. Peng, and G. Östlund, Oceanic radiocarbon: Separation of the natural and bomb components, *Global Biogeochemical Cycles*, 9 (2), 263-288, 1995.
- Conway, T.J., P.P. Tans, L.S. Waterman, K.W. Thoning, D.R. Kitzis, K.A. Masarie, and N. Zhang, Evidence for interannual variability of the carbon cycle from the National Oceanic and Atmospheric Administration/Climate Monitoring and Diagnostics Laboratory global air sampling network, *Journal of Geophysical Research*, 99, 22831-22855, 1994.
- Craig, H., Isotopic standards for carbon and oxygen and correction factors for mass-spectrometric analysis of carbon dioxide, *Geochimica et Cosmochimica Acta*, 12 (1-2), 133-149, 1957.
- Cunnold, D.M., P.J. Fraser, R.F. Weiss, R.G. Prinn, P.G. Simmonds, B.R. Miller, F.N. Alyea, and A.J. Crawford, Global trends and annual releases of CCl_3F and CCl_2F_2 estimated from ALE/GAGE and other measurements from July 1978 to June 1991, *Journal of Geophysical Research*, 99, 1107-1126, 1994.
- Damon, P.E., and R.E. Sternberg, Global production and decay of radiocarbon, *Radiocarbon*, 31, 697-703, 1989.
- Dibb, J.E., L.D. Meeker, R.C. Finkel, J.R. Southon, M.W. Caffee, and L.A. Barrie, Estimation of stratospheric input to the Arctic troposphere: ^7Be and ^{10}Be in aerosols at Alert, Canada, *Journal of Geophysical Research*, 99 (D6), 12855-12864, 1994.
- Druffel, E., Pacific Bomb Radiocarbon Coral Data, in *IGBP PAGES/World Data Center-A for Paleoclimatology*, NOAA/NGDC Paleoclimatology Program, Boulder, CO, 1995.
- Druffel, E.M., Radiocarbon in Annual Coral Rings of the Pacific and Atlantic Oceans, Ph. D. thesis, Univ. of Calif., San Diego, 1980.

- Druffel, E.M., Radiocarbon in annual coral rings from the eastern tropical Pacific Ocean, *Geophysical Research Letters*, 8 (1), 59-62, 1981.
- Druffel, E.M., and H.E. Suess, On the Radiocarbon Record in Banded Corals: Exchange Parameters and Net Transport of $^{14}\text{CO}_2$ Between Atmosphere and Surface Ocean, *Journal of Geophysical Research*, 88 (C2), 1271-1280, 1983.
- Enting, I.G., Nuclear Weapons Data for use in Carbon Cycle Modelling, *CSIRO Division of Atmospheric Physics Technical Paper*, 44, 1-18, 1982.
- Etcheto, J., J. Boutin, and L. Merlivat, Seasonal variation of the CO_2 exchange coefficient over the global ocean using satellite wind speed measurements, *Tellus*, 43B, 247-255, 1991.
- Etcheto, J., and L. Merlivat, Satellite determination of the carbon dioxide exchange coefficient at the ocean-atmosphere interface: a first step, *Journal of Geophysical Research*, 93 (C12), 15669-15678, 1988.
- Etcheto, J., A. Morel, and A. Poisson, Large scale determination of ocean-atmosphere CO_2 flux, in *The Global Carbon Cycle and its Perturbation by Man and Climate*, edited by M. Heimann, pp. 105-117, EC-EPOC Final report, Hamburg, 1993.
- Feichter, J., and P.J. Crutzen, Parameterization of vertical tracer transport due to deep cumulus convection in a global transport model and its evaluation with ^{222}Rn , *Tellus*, 42B, 100-117, 1990.
- Friedli, H., H. Löttscher, H. Oeschger, U. Siegenthaler, and B. Stauffer, Ice core record of the $^{13}\text{C}/^{12}\text{C}$ ratio of atmospheric CO_2 in the past two centuries, *Nature*, 324, 237-238, 1986.
- Goudriaan, J., Biosphere structure, carbon sequestering potential and the atmospheric ^{14}C carbon record, *J. Experimental Botany*, 43, 1111-1119, 1992.
- Harnisch, J., R. Borchers, P. Fabian, and M. Maiss, Tropospheric trends for CF_4 and C_2F_6 since 1982 derived from SF_6 dated stratospheric air, *Geophysical Research Letters*, 23 (10), 1103-1106, 1996.
- Harrison, K., W.S. Broecker, and G. Bonani, A strategy for estimating the impact of CO_2 fertilization on soil carbon storage, *Global Biogeochemical Cycles*, 7, 69-80, 1993.
- Heimann, M., personal communication, *MPI für Meteorologie, Hamburg, Germany*.
- Heimann, M., and C.D. Keeling, A three-dimensional model of atmospheric CO_2 transport based on observed winds - Part 2: Model description and simulated tracer experiments, *Geophysical Monograph*, 55, 237-275, 1989.
- Heimann, M., C.D. Keeling, and C.J. Tucker, A three-dimensional model of atmospheric CO_2 transport based on observed winds - Part 3: Seasonal cycle and synoptic time scale variations, *Geophysical Monograph*, 55, 277-303, 1989.
- Heimann, M., and P. Monfray, Spatial and temporal variation of the gas exchange coefficient for CO_2 : 1. Data analysis and global validation, in *subm. to Journal of Geophysical Research*, MPI für Meteorologie, Hamburg, 1989.
- Hesshaimer, A model to investigate the concentration of trace constituents in the Earth atmosphere (in German), Univ. of Heidelberg, Heidelberg, 1990.
- Hesshaimer, V., M. Heimann, and I. Levin, Radiocarbon evidence for a smaller oceanic carbon dioxide sink than previously believed, *Nature*, 370, 201-203, 1994.

- Hesshaimer, V., I. Levin, and M. Heimann, Modeling the global distribution of CO₂ and ¹⁴C in the atmosphere, in *Proceedings of the Third International Conference on Analysis and Evaluation of Atmospheric CO₂ Data Present and Past*, WMO Rep. 59, World Meteorol. Organ., Geneva, 1989.
- Holton, J.R., P.H. Haynes, M.E. McIntyre, A.R. Douglass, R.B. Rood, and L. Pfister, Stratosphere - Troposphere Exchange, *Reviews of Geophysics*, 33 (4), 403-439, 1995.
- Houghton, *Physics of the Atmosphere*, Cambridge Univ. Press, New York, 1977.
- Houghton, R.A., and J.L. Hackler, Continental scale estimates of the biotic carbon flux from land cover change: 1850 to 1980, in *CDIAC Databases*, pp. NDP-050, CDIAC/ORNL, 1995.
- Hyson, P., P.J. Fraser, and G.I. Pearman, A two-dimensional transport simulation model for trace atmospheric constituents, *Journal of Geophysical Research*, 85, 4443-4456, 1980.
- IPCC1995, Technical Summary, in *Climate Change 1995: The science of Climate Change. Contribution of Working Group I to the Second Assessment Report of the Intergovernmental Panel on Climate Change*, edited by J.T. Houghton, L.G.M. Filho, B.A. Callander, N. Harris, A. Kattenberg, and K. Mashell, pp. 9-49, Cambridge Univ. Press, Cambridge, 1996.
- Jacob, D.A., M.J. Prather, S.C. Wofsy, and M.B. McElroy, Atmospheric distribution of ⁸⁵Kr simulated with a general circulation model, *Journal of Geophysical Research*, 92, 6614-6626, 1987.
- Jain, A.K., H.S. Kheshgi, and D.J. Wuebbles, Is there an imbalance in the global budget of bomb-produced radiocarbon?, *Journal of Geophysical Research*, 102 (D1), 1327-1333, 1997.
- Joos, F., personal communication, Physics Institute, Univ. of Bern, Switzerland, 1993.
- Karlén, I., I.U. Olsson, P. Kallenberg, and S. Kilici, Absolute determination of the activity of two ¹⁴C dating standards, *Arkiv för Geofysik*, 4 (22), 465-471, 1968.
- Keeling, C.D., Global historical CO₂ emissions, in *Trends '93: A Compendium of Data on Global Change*, edited by T.A. Boden, D.P. Kaiser, R.J. Sepanski, and F.W. Stoss, pp. 501-504, CDIAC, Oak Ridge, Tenn., 1994.
- Keeling, C.D., R.B. Bacastow, A.F. Carter, S.C. Piper, T.P. Whorf, M. Heimann, W.G. Mook, and H. Roeloffzen, A three-dimensional model of atmospheric CO₂ transport based on observed winds - Part 1: Analysis of observational data, *Geophysical Monograph*, 55, 305-363, 1989a.
- Keeling, C.D., S.C. Piper, and M. Heimann, A three-dimensional model of atmospheric CO₂ transport based on observed winds - Part 4: Mean annual gradients and interannual variations, *Geophysical Monograph*, 55, 305-363, 1989b.
- Keeling, C.D., and T.P. Whorf, CO₂ observations at Mauna Loa, Hawaii, in *Trends 90*, edited by T.A. Boden, P. Kanciruk, and M.P. Farrell, pp. 8-9, Oak Ridge Natn. Lab., Oak Ridge, 1990.
- Keeling, C.D., and T.P. Whorf, Atmospheric CO₂ records from sites in the SIO air sampling network, in *Trends '93: A Compendium of Data on Global Change*, edited by T.A. Boden, D.P. Kaiser, R.J. Sepanski, and F.W. Stoss, pp. 16-26, ORNL/CDIAC, Oak Ridge, Tennessee, 1994.
- Ko, M.K.W., N.D. Sze, W.-C. Wang, G. Shia, A. Goldman, F.J. Murcray, and C.P. Rinsland, Atmospheric sulfur hexafluoride: Sources, sinks, and greenhouse warming, *Journal of Geophysical Research*, 98, 10499-10507, 1993.
- Kumar, M., and J.L. Monteith, Remote sensing of crop growth, in *Plants and the Daylight Spectrum*, edited by H. Smith, pp. 133-144, Academic Press, New York, 1981.

- Lassey, K.R., I.G. Enting, and C.M. Trudinger, The earth's radiocarbon budget - A consistent model of the global carbon and radiocarbon cycles, *Tellus*, 48B, 487-501, 1996.
- Lassey, K.R., M.R. Manning, and B.J. O'Brien, An Overview of Oceanic Radiocarbon: Its Inventory and Dynamics, *Aquatic Sciences*, 3 (2&3), 117-146, 1990.
- Levin, I., personal communication, *Institut für Umweltphysik, Heidelberg, Germany*.
- Levin, I., The recent state of carbon cycling through the atmosphere, in *Carbon Cycling in the Glacial Ocean: Constraints on the Ocean's Role in Global Change*, edited by R. Zahn, T.F. Pedersen, M.A. Kaminski, and L. Labeyrie, pp. 3-13, Springer, Heidelberg, 1994.
- Levin, I., R. Böisinger, G. Bonani, R.J. Francey, B. Kromer, K.O. Münnich, M. Suter, N.B.A. Trivett, and W. Wölfli, Radiocarbon in atmospheric carbon dioxide and methane: global distribution and trends, in *Radiocarbon After Four Decades: An Interdisciplinary Perspective*, edited by R.E. Taylor, A. Long, and R.S. Kra, pp. 503-518, Springer-Verlag, New York, 1992.
- Levin, I., and V. Hesshaimer, Refining of atmospheric transport model entries by the globally observed passive tracer distributions of $^{85}\text{krypton}$ and sulfur hexafluoride (SF_6), *Journal of Geophysical Research*, 101 (D11), 16745-16755, 1996.
- Levin, I., B. Kromer, H. Schoch-Fischer, M. Bruns, M. Münnich, D. Berdau, J.C. Vogel, and K.O. Münnich, 25 years of tropospheric ^{14}C observations in Central Europe, *Radiocarbon*, 27 (1), 1-19, 1985.
- Levin, I., B. Kromer, D. Wagenbach, and K.O. Münnich, Carbon isotope measurements of atmospheric CO_2 at a coastal station in Antarctica, *Tellus*, 39B, 89-95, 1987.
- Lingenfelter, R.E., Production of Carbon 14 by Cosmic-Ray Neutrons, *Reviews of Geophysics*, 1 (1), 35-55, 1963.
- Liss, P.S., and L. Merlivat, Air-sea gas exchange rates: Introduction and synthesis, in *The Role of Air-Sea Exchange in Geochemical Cycling*, edited by P. Buat-Ménard, pp. 113-127, Reidel, D., Dordrecht, 1986.
- Machta, L., R.J. List, and K. Telegadas, Meteorology of fallout from 1961-62 nuclear tests, in *Congress of the U.S., Hearing before Subcommittee in Research, Development and Radiation of the Joint Committee of Atomic Energy, 88th Congress*, pp. 46-61, 1963.
- Maier-Reimer, E., Geochemical cycles in an ocean general circulation model. Preindustrial tracer distributions, *Global Biogeochemical Cycles*, 7, 645-677, 1993.
- Maier-Reimer, E., Personal communication, MPI für Meteorologie, Hamburg, Germany, 1994.
- Maiss, M., and I. Levin, Global increase of SF_6 observed in the atmosphere, *Geophysical Research Letters*, 21, 569-572, 1994.
- Maiss, M., L.P. Steele, R.J. Francey, P.J. Fraser, R.L. Langenfelds, N.B.A. Trivett, and I. Levin, Sulfur hexafluoride-A powerful new atmospheric tracer, *Atmospheric Environment*, 30 (10/11), 1621-1629, 1996.
- Manning, M.R., D.C. Lowe, W.H. Melhuish, R.J. Sparks, G. Wallace, C.A.M. Brenninkmeijer, and R.C. McGill, The use of radiocarbon measurements in atmospheric studies, *Radiocarbon*, 32 (1), 37-58, 1990.
- Marland, G., R.J. Andres, and T.A. Boden, Global, regional and national CO_2 emissions, in *Trends '93: a compendium of data on global change*, edited by T.A. Boden, D.P. Kaiser, R.J. Sepanski, and F.W. Stoss, pp. 505-584, Carbon Dioxide Information Analysis Center, Oak Ridge, Tenn., U.S.A., 1994.
- Mook, W.G., *Principles of Isotope Hydrology (Introductory course on Isotope Hydrology)*, 153 pp., Amsterdam, 1994.

- Mook, W.G., J.C. Bommerson, and W.H. Staverman, Carbon isotope fractionation between dissolved bicarbonate and gaseous carbon dioxide, *Earth and Planetary Science Letters*, 22, 169-176, 1974.
- Morris, R.A., T.M. Miller, A.A. Viggiano, J.F. Paulson, S. Solomon, and G. Reid, Effects of electron and ion reactions on atmospheric lifetimes of fully fluorinated compounds, *Journal of Geophysical Research*, 100 (D1), 1287-1294, 1995.
- Nakamura, T., T. Nakazawa, N. Nakai, H. Kitagawa, H. Honda, T. Itoh, T. Machida, and E. Matsumoto, Measurement of ^{14}C concentrations of stratospheric CO_2 by accelerator mass spectrometry, *Radiocarbon*, 34 (3), 745-752, 1992.
- Neftel, A., E. Moor, H. Oeschger, and B. Stauffer, Evidence from polar ice cores for the increase in atmospheric CO_2 in the past two centuries, *Nature*, 315 (315), 45-47, 1985.
- O'Brien, K., Secular Variations in the Production of Cosmogenic Isotopes in the Earth's Atmosphere, *Journal of Geophysical Research*, 84 (A2), 423-431, 1979.
- O'Brien, K., A. De La Zerda, Z. Lerner, M.A. Shea, and D.F. Smart, The production of cosmogenic isotopes in the Earth's atmosphere and their inventories, in *The Sun in Time*, edited by C.P. Sonnet, M.S. Giampapa, and M.S. Matthews, pp. 317-342, University of Arizona Press, Tucson, 1991.
- Oeschger, H., U. Siegenthaler, U. Schotterer, and A. Gugelmann, A box diffusion model to study the carbon dioxide exchange in nature, *Tellus*, 27, 168-192, 1975.
- Peng, T.H., and W.S. Broecker, Inventories of bomb ^{14}C in the ocean, in *Abstracts of the 4th International CO_2 Conference, Carqueiranne, France, 13-17 September 1993*, edited by G. Lambert, and L. Merlivat, pp. 214, (WMO-GAW-Report No. 89, WMO/TD-NO 561, Geneva), 1993.
- Post III, W.M., Organic carbon in soil and the global carbon cycle, in *The Global Carbon Cycle*, edited by M. Heimann, pp. 277-302, Springer, 1993.
- Prather, M.J., M.B. McElroy, S.C. Wofsy, G. Russell, and D. Rind, Chemistry of the global troposphere: Fluorocarbons as tracers of air motion, *Journal of Geophysical Research*, 91, 6671-6681, 1987.
- Rasch, P.J., X. Tie, B.A. Boville, and D.L. Williamson, A three-dimensional transport model for the middle atmosphere, *Journal of Geophysical Research*, 99 (D1), 999-1017, 1994.
- Rath, H.K., Simulation of the global ^{85}Kr and $^{14}\text{CO}_2$ distribution by means of a time dependent two-dimensional model of the atmosphere (in German), Ph.D. thesis, Univ. of Heidelberg, Germany, 1988.
- Ravishankara, A.R., S. Solomon, A.A. Turnipseed, and R.F. Warren, the atmospheric lifetimes of long-lived halogenated species, *Science*, 259, 194-199, 1993.
- Rehfeld, S., and M. Heimann, Three dimensional atmospheric transport simulation of the radioactive tracers ^{210}Pb , ^7Be , ^{10}Be , and ^{90}Sr , *Journal of Geophysical Research*, 100 (D12), 26141-26161, 1995.
- Rotty, R.M., Estimates of seasonal variation in fossil fuel CO_2 emissions, *Tellus*, 39B, 184-202, 1987.
- Siegenthaler, U., Uptake of excess CO_2 by an outcrop-diffusion model of the ocean, *Journal of Geophysical Research*, 88, 3599-3608, 1983.
- Siegenthaler, U., H. Friedli, H. Loetscher, E. Moor, A. Neftel, H. Oeschger, and B. Stauffer, Stable-isotope ratios and concentration of CO_2 in air from polar ice cores, *Ann. Glaciol.*, 10, 151-156, 1988.

- Siegenthaler, U., and F. Joos, Use of a simple model for studying oceanic tracer distributions and the global carbon cycle, *Tellus*, 44B, 186-207, 1992.
- Siegenthaler, U., and K.O. Münnich, $^{13}\text{C}/^{12}\text{C}$ Fractionation during CO_2 Transfer from Air to Sea, in *Carbon Cycle Modelling (SCOPE 16)*, edited by B. Bolin, pp. 249-257, John Wiley & Sons, New York, 1981.
- Siegenthaler, U., and H. Oeschger, Biospheric CO_2 emissions during the past 200 years reconstructed by deconvolution of ice core data, *Tellus*, 39B, 140-154, 1987.
- Siegenthaler, U., and G. Sarmiento, Atmospheric carbon dioxide and the ocean, *Nature*, 365, 119-125, 1993.
- Stordal, F., B. Innset, A.S. Grossmann, and G. Myhre, SF_6 as a greenhouse gas: An assessment of Norwegian and global sources and the global warming potential, in *NILU-Rep. 15/93*, Norw. Inst. of Air Res., Lillestrom, Norway, 1993.
- Stuiver, M., ^{14}C Distribution in the Atlantic Ocean, *Journal of Geophysical Research*, 85 (C5), 2711-2718, 1980.
- Stuiver, M., H.G. Östlund, and T.A. McConnaughey, GEOSECS Atlantic and Pacific ^{14}C distribution, in *SCOPE 16, Carbon Cycle Modelling*, edited by B. Bolin, pp. 201-221, Wiley, New York, 1981.
- Stuiver, M., and H.A. Polach, Discussion - Reporting of ^{14}C data, *Radiocarbon*, 19 (3), 355-363, 1977.
- Stuiver, M., and P.D. Quay, Changes in Atmospheric Carbon-14 Attributed to a Variable Sun, *Science*, 207 (4426), 13-19, 1980.
- Stuiver, M., and P.D. Quay, Atmospheric ^{14}C changes resulting from fossil fuel CO_2 release and cosmic ray flux variability, *Earth and Planetary Science Letters*, 53, 349-362, 1981.
- Suess, H.E., Radiocarbon concentration in modern wood, *Science*, 122, 415-417, 1955.
- Tans, P., A Compilation of Bomb ^{14}C Data for Use in Global Carbon Model Calculations, in *Carbon Cycle Modelling (SCOPE 16)*, edited by B. Bolin, pp. 131-157, John Wiley & Sons, New York, 1981.
- Tans, P.P., P.S. Bakwin, T.J. Conway, R.W. Dissly, E.J. Dlugokencky, L.S. Geller, D.W. Guenther, D.F. Hurst, D.R. Kitzis, P.M. Lang, K.A. Masarie, J.B. Miller, P.C. Novelli, C. Prostko-Bell, M. Ramonet, K.W. Thoning, M. Trolier, L.S. Waterman, N. Zhang, and C. Zhao, 2. Carbon Cycle, in *Summary Report 1994-95, No. 23*, edited by D.J. Hofmann, J.T. Peterson, and T.M. Rosson, pp. 29-49, NOAA/CMDL, Boulder, CO, 1996.
- Tans, P.P., I.Y. Fung, and T. Takahashi, Observational constraints on the global atmospheric CO_2 budget, *Science*, 247, 1431-1438, 1990.
- Telegadas, K., The Seasonal Atmospheric Distribution and Inventories of Excess Carbon-14 from March 1955 to July 1969, in *Health and Safety Laboratory Report 166*, edited by E.P. Hardy Jr., pp. 2-87, U.S. At. Energy Comm., Springfield, Virginia, 1971.
- Thoning, K.W., P.P. Tans, and W.D. Komhyr, Atmospheric carbon dioxide at Mauna Loa Observatory, 2, Analysis of the NOAA GMCC data, *Journal of Geophysical Research*, 94, 8549-8565, 1989.
- Toggweiler, J.R., K. Dixon, and K. Bryan, Simulations of radiocarbon in a coarse resolution world ocean model, I, steady state prebomb distributions, *Journal of Geophysical Research*, 94, 8217-8242, 1989.
- UNSCEAR, Ionizing radiation: sources and biological effects, in *Report to the General Assembly*, UNO (publication sales no. E82.IX.8), New York, 1982.

- UNSCEAR, Sources and Effects of Ionizing Radiation, in *Report to the General Assembly*, UNO (publication sales no. E94.IX.2), New York, 1993.
- Volk, C.M., J.W. Elkins, D.W. Fahey, T.J. Salawitch, G.S. Dutton, J.M. Gilligan, M.H. Proffitt, M. Loewenstein, J.R. Podolske, K. Minschwaner, J.J. Margitan, and K.R. Chan, Quantifying Transport Between the Tropical and Mid-Latitude Lower Stratosphere, *Science*, 272, 1763-1768, 1996.
- Von Hippel, F.D., H. Albright, and B.G. Levi, Quantities of fissile materials in U.S. and Soviet nuclear weapons arsenals, in *Rep. PU/CEES 168*, Cent. for Energy and Environ. Stud., Princeton Univ., Princeton, N. J., 1986.
- Wagenbach, D., Coastal Antarctica: atmospheric chemical composition and atmospheric transport, in *Chemical Exchange Between the Atmosphere and Polar Snow*, edited by E.W. Wolff, and R.C. Bales, pp. 173-199, Springer-Verlag, New York, 1996.
- Watson, A., Air-sea gas exchange and carbon dioxide, in *The Global Carbon Cycle*, edited by M. Heimann, pp. 397-411, Springer, Heidelberg, 1993.
- Watson, A.J., R.C. Upstill-Goddard, and P.S. Liss, Air-sea gas exchange in rough and stormy seas measured by a dual-tracer technique, *Nature*, 349, 145-147, 1991.
- Weiss, W., H. Sartorius, and H. Stockburger, Global distribution of atmospheric ^{85}Kr -A database for the verification of transport and mixing models, in *Isotopes of Noble Gases as Tracers in Environmental Studies*, Int. At. Energy Agency, Vienna, 1992.
- Weiss, W., A. Sittkus, H. Stockburger, H. Sartorius, and K.O. Münnich, Large-scale atmospheric mixing derived from meridional profiles of krypton 85, *Journal of Geophysical Research*, 88, 8574-8578, 1983.
- Zimmermann, P.H., J. Feichter, H.K. Rath, P.J. Crutzen, and W. Weiss, A global three-dimensional source-receptor model investigation using ^{85}Kr , *Atmospheric Environment*, 23, 25-35, 1989.

FIGURES

Figure 1	2
Figure 2	12
Figure 3	13
Figure 4	14
Figure 5	16
Figure 6	17
Figure 7	18
Figure 8	19
Figure 9	20
Figure 10	27
Figure 11	28
Figure 12	30
Figure 13	34
Figure 14	35
Figure 15	37
Figure 16	38
Figure 17	42
Figure 18	42
Figure 19	43
Figure 20	45
Figure 21	48
Figure 22	49
Figure 23	50
Figure 24	51
Figure 25	56
Figure 26	57
Figure 27	64
Figure 28	70
Figure 29	74

TABLES

Table 1	6
Table 2	8
Table 3	9
Table 4	69

DANKSAGUNG

Diese Dissertation kennzeichnet für mich den Abschluss von einigen Jahren Forschung am Institut für Umweltp Physik. Während dieser Zeit intensiver und erfreulicher Zusammenarbeit habe ich stets tiefere Einsicht, richtungweisende Ratschläge sowie entscheidende Unterstützung von meiner Betreuerin PD Dr. Ingeborg Levin erhalten. Ihre hohe Forderung sowohl an die Qualität der Messung von atmosphärischem Radiokohlenstoff als auch an deren Interpretation erlaubten mir einerseits mein wissenschaftliches Handwerkszeug zu festigen und andererseits spannende Ergebnisse zu erhalten. Dafür will ich ihr hiermit meinen besonderen Dank erweisen.

Buchstäblich seit meinem ersten Tag an diesem Institut habe ich wichtige Ansätze, Beobachtungen und Informationen aus dem reichen und grosszügigen Fundus von Prof. Dr. Karl Otto Münnich erhalten. Hierfür bin ich ihm ausgesprochen dankbar.

Ausdrücklichen Dank schulde ich auch Dr. Martin Heimann vom Max-Planck-Institut für Meteorologie in Hamburg für seine sehr hilfreiche auswärtige Betreuung sowie für seine stets anregende Kritik.

Mein weiterer Dank geht an Prof. Dr. Till Kirsten vom Max-Planck-Institut für Kernphysik in Heidelberg für die Übernahme des Zweitgutachtens meiner Dissertation.

Alle Anderen, hier ungenannten, haben ihren Platz in meinem Herzen.

